Report No. BD-544-11

Final Report

Evaluation and Validation of a High-Speed Multi-Function System for Automated Pavement Condition Survey

M. Gunaratne, Ph.D., P.E.
Principal Investigator

and

A. Mraz, Ph.D.
D. Randeniya
Graduate Assistants

Submitted to

Florida Department of Transportation

By the

Department of Civil and Environmental Engineering
College of Engineering
University of South Florida
Tampa, FL 33620
Ph. (813)974-2275

June 15, 2006

Evaluation and Validation of a High-Speed Multi-Function System for Automated Pavement Condition Survey

M. Gunaratne, Ph.D., P.E.
Principal Investigator

and

A. Mraz, Ph.D.
D. Randeniya
Graduate Assistants

Department of Civil and Environmental Engineering
College of Engineering
University of South Florida
Tampa, Florida 33620

June 15, 2006

1. Report No.	2. Government Accession No.	3. Recipient's Catalog No.
BD-544-11		2101-1014

4. Title and Subtitle	5. Report Date
EVALUATION AND VALIDATION OF A HIGH-SPEED MULTI-FUNCTION SYSTEM FOR AUTOMATED PAVEMENT CONDITION SURVEY	June 15, 2006
	6. Performing Organization Code CEE/FDOT/1014

7. Author(s)	8. Performing Organization Report No.
M.Gunaratne, A.Mraz and D. Randeniya	

9. Performing Organization Name and Address	10. Work Unit No. (TRAIS)
Department of Civil and Environmental Engineering College of Engineering University of South Florida, Tampa, FL 33620	11. Contract or Grant No. BD-544-11

12. Sponsoring Agency Name and Address	13. Type of Report and Period Covered
Florida Department of Transportation 605 Suwannee St. MS 30 Tallahassee, FL 32399	Final report Aug. 2003 – May 2006
	14. Sponsoring Agency Code

15. Supplementary Notes

Prepared in cooperation with the Federal Highway Administration

16. Abstract

FDOT has developed and validated a multi-functional survey vehicle (MPSV) for rapid and automated collection of pavement condition data using its imaging subsystem and identification of hazardous conditions using its inertial subsystem. During the first phase of the study, an efficient technique was developed to filter out noise present in the pavement crack images, by using intensity measurements obtained from a standard grayscale target. The results from the initial phases of the study can be used to (1) minimize the effect of noise on digital images of pavement cracks, (2) improve the accuracy of evaluation of pavement cracks based on digital images, and (3) determine the optimum conditions for most accurate crack evaluation. The inertial measurement unit (IMU) subsystem of the MPSV also plays a vital role because of its capability for rapid and automatic collection of roadway geometrical data such as cross-slopes, curvatures and grades. It was also seen that the cross-slope data acquired by the IMU subsystem of the MPSV were generally repeatable and accurate on asphalt pavements, with respect to ASTM standards. Hence the investigators believe that the MPSV is well-equipped for statewide implementation of automated cross-slope and super-elevation measurements. Furthermore, the investigators also recommend that the MPSV is adequate for automated project-level evaluation of roadway curvature.

17. Key Word	18. Distribution Statement
Multi-functional survey, cross-slope, grade, radius of curvature, digital images, precision, accuracy, inertial measurement	No restrictions. This document is available to the public through the National Technical Information Service, Springfield, VA 22161

19. Security Classif. (of this report)	20. Security Classif. (of this page)	21. No. of Pages	22. Price
Unclassified	Unclassified	138	

CONVERSION FACTORS

To convert	British	SI	multiply by
Acceleration	ft/s^2	m/s^2	3.048E-1
Area	ft^2	m^2	9.290E-2
Density	$slugs/ft^3$	kg/m^3	5.154E+2
Length	ft	m	3.048E-1
Pressure	lb/ft^2	N/m^2	4.788E+1
Velocity	ft/s	m/s	3.048E-1

Acknowledgments

The authors are indebted to Mr. Abdenour Nazef, Pavement Systems Evaluation Engineer, State of Florida Department of Transportation (FDOT), State Materials Office, Gainesville, Florida, for his diligent project management efforts. In addition, the constant collaboration of Dr. Alex Mraz of Applied Research Associates, Gainesville, FL and Mr. Stacy Scott and Mr. Glenn Salvo of FDOT State Materials Office, Gainesville, Florida is greatly appreciated. Finally, the financial support provided by Dr. Bouzed Choubane, State Pavement Materials Engineer, FDOT, is gratefully acknowledged.

TABLE OF CONTENTS

LIST OF FIGURES

LIST OF TABLES

EXECUTIVE SUMMARY

The Florida Department of Transportation (FDOT) has developed and validated a multi-functional survey vehicle (MPSV) for collection of highway pavement related data at normal operating speeds. With its ability to collect pavement, right-of-way, and side-view images together with position location, cross-slope, grade, curvature, rutting and roughness data, this state-of-the-art vehicle enables rapid and automated collection of roadway performance data and identification of hazardous conditions. On the other hand, the most widely used means for evaluation of pavement distress, the manual survey, involves a high degree of subjectivity, low production rates, and exposure to hazardous conditions. Hence the above FDOT MPSV would indeed be an efficient, cost-effective, and safe alternative for collection and evaluation of pavement distress data.

The first phase of the research documented in this report focused on the investigation of the sources of noise that affect the quality of digital line-scan pavement distress images. Specifically, the Signal-to-Noise Ratio (SNR) was identified as an objective parameter appropriate for the evaluation of quality of pavement images. A number of widely used noise filtering methods that can enhance the images captured by the pavement camera thereby improving the accuracy of crack evaluation were also identified. At the completion of this phase of the study, a novel and efficient technique was developed to filter out noise especially present in the pavement crack images, by using intensity measurements obtained from a standard grayscale target.

Second, a detailed experimental study was conducted to investigate the effect of vehicle speed, ambient lighting conditions and the pavement lighting system on the accuracy and precision of digital line-scan images in representing the actual crack condition of a pavement. It was revealed that the speed of the survey vehicle does not significantly affect the quality of pavement images or the precision and accuracy of crack evaluation. Furthermore, it was seen that the artificial lighting system is redundant and even counter-productive in the evaluation of cracks under adequate ambient lighting. The experimental

results also indicated that the accuracy and precision of crack evaluation based on digital images is satisfactory only in the case of high severity cracks. In addition, the effect of the vehicle's movement in the blurring of images and the geometrical distortion of the image due to optical distortion and distance measurement instrument (DMI) error were also investigated in this phase. Hence the conclusions drawn from the first and second phases of the study can be used to (1) minimize the effect of noise on digital images of pavement cracks, (2) improve the accuracy of evaluation of pavement cracks based on digital images, and (3) determine the optimum conditions for most accurate crack evaluation.

Another important aspect of the evaluation of pavement infrastructure consists of verifying the roadway geometrical design features such as cross-slopes, super elevations, radii of curvature, and grades to be within acceptable tolerances at all locations of a roadway. In this respect, the inertial measurement unit (IMU) subsystem of the FDOT MPSV plays a vital role because of its capability for rapid and automatic collection of roadway geometrical data. Rapid evaluations are particularly essential in contingency situations where pavement evaluators are required to perform impromptu safety inspections at roadway locations that have been identified as presenting safety hazards. Hence the assurance of the repeatability and accuracy of the IMU subsystem would be critical in their subsequent decisions. Thus, the third phase of the research investigation involved the performance of a variety of field experiments that were designed to better interpret the data produced by the IMU subsystem of the FDOT MPSV and determine its accuracy and precision under different operating conditions. During this effort, the MPSV manufacturer's algorithms that generate roadway cross-slopes, grades and curvature results based on its IMU subsystem were scrutinized in detail. In order to address the issues of undulations and uncertainties inherent in the radius of curvature data produced by the manufacturer's algorithms, a number of effective analytical techniques such as the moving averages and statistical filtering were incorporated in them. Consequently, the modified kinematic method was formulated by the investigators to

provide more accurate and stable radii of curvature results for circular and non-circular curves.

During the fourth and the final phase of the study, a comprehensive experimental program was developed for validating the geometrical data produced by the IMU subsystem of the MPSV by comparing them with corresponding data obtained from manual surveys. It was seen that the cross-slope and super-elevation data were generally repeatable and accurate with respect to ASTM standards on both newly laid and relatively aged asphalt pavements. Considering the results of both the preliminary testing program and the detailed testing program, the investigators believe that the FDOT MPSV is well-equipped for statewide implementation of automated cross-slope and super-elevation measurements.

However, the precision and accuracy of radii of curvature data and the accuracy of grade data were significantly less than that of the cross-slope measurements, on both new and aged pavements. Once the possible causes of such inaccuracies were identified, the relevant experimental conditions were enhanced to overcome the limitations of the initial experimentation. In this respect, renewed efforts and measures such as the installation of a laser on the rear bumper of the MPSV and more controlled, better guided and smoother maneuvering of MPSV during experimentation on curves in particular, yielded improved precision and accuracy results for grade and radii of curvature measurements as well. The investigators also recommend that the FDOT MPSV is adequate for automated project-level evaluation of roadway curvature.

CHAPTER 1
ENHANCEMENT OF PAVEMENT DISTRESS IMAGES USING NOISE FILTRATION

1.0 Introduction

As the nation's transportation infrastructure grows, so does the need for keeping it safe and operational. State and local agencies are responsible for carrying out program development to evaluate roadway performance, identify conditions that are detrimental to highway safety, and strategize mitigating solutions. Advances in sensor and inertial navigation technologies have enhanced the functionality of pavement evaluation equipment, allowing highway engineers to capitalize on the large amount of information afforded by this state-of-the-art equipment.

Manual survey of pavements still represents the most widely used means for inspection and evaluation of pavements. Manual rating of the pavement through windshield surveys to identify the types of surface cracking and other distresses leads to relatively slow evaluation. And when necessary, the survey crew has to physically be in the travel lane to evaluate the pavement, exposing themselves to hazardous conditions. Therefore, the high speed automatic pavement evaluation is an efficient and cost-effective alternative that assures the safety of the field survey personnel and other travelers. Numerous efforts have been made in the US in implementing automated pavement evaluation systems. The study undertaken for the Oregon and Washington DOT evaluated pavement data collection technology (Smith et al, 1996). Wang (2000) also presents the development of several automated pavement evaluation systems. In addition, NCHRP Synthesis 334 (2004) examines highway community practice, research, and development efforts in the automated collection and processing of pavement condition data techniques used in network-level pavement management.

Meanwhile the Florida Department of Transportation (FDOT) has developed a state-of-the-art Multi-Purpose Survey Vehicle (MPSV) for high-speed collection of pavement related data such as pavement images, cross-slopes, grades, curvatures, rutting and roughness information along with the location referencing of such data. At the inception of the current research study USF investigators and the FDOT project staff proposed to assess each individual subsystem of the MPSV through the design of controlled experiments which would validate the measurements of each subsystem and prepare it for eventual implementation. The project scope consisted of two

main tasks; (1) evaluation of the pavement camera subsystem and (2) evaluation of the inertial measurement unit/DGPS subsystem. The first two chapters of this report (Chapters 1 and 2) are dedicated to report the findings of the first task, while the research efforts toward fulfilling the second task are described in Chapters 3 and 4.

The pavement imaging system of the FDOT MPSV consists of a Basler L103 line-scan camera with a resolution of 1.9 by 1.9 mm (or saved image resolution of 2048 by 2942 pixels) mounted over the pavement surface at a preset height, interfaced with a dedicated computer. The camera captures 2942 consecutive image lines separately and combines them together to create one image. Images can be captured at preset exposure times such as 1/19,000 or 1/40,000 seconds depending on the lighting conditions. To enable night survey and minimize shadow overcast on pavement, the pavement imaging system is coupled with a lighting system consisting of ten (10) high intensity discharge 150 watts Philips MasterColor CDM lamps each with polished reflectors.

1.1 Quality of highway pavement distress images

The key attribute to the loss in quality of digital pavement distress images is the noise present in them. Hence the USF investigators determined that it is essential to understand the causes of noise and its impact on various components of the imaging subsystem of the FDOT evaluation vehicle. The results from this phase of the study is expected to shed light into techniques which can be used to improve the accuracy of crack evaluation by improving the quality of pavement distress images.

1.2 Types of Noise in CCD Sensors

Noise generally occurs in digital images captured by Charge-Coupled Devices (CCD) due to the visible effects of electronic errors or compression artifacts. Noise can be evaluated using the variation in the digital image pixel intensities of a uniformly bright area. Hence noise is usually described by statistical characteristics such as the standard deviation of the pixel intensity variation and closely approximated probability distribution such as the Gaussian or Poisson distribution (Sonka et al. 1999). The effect of noise on the quality of a digital image is described by the signal-to-noise ratio (SNR) defined as

$$SNR(x) = \frac{\mu(x)}{\sigma(x)} \tag{1.1a}$$

where μ is the mean of all intensity values x in the image and σ represents their standard deviation. The larger the SNR, the stronger the signal the lower the noise is, and the more desirable the image quality is. However, the standard is to use the logarithm (base 10) of Eqn. (1.1a) and express SNR in decibels (db), as follows:

$$SNR(db) = 20\left(\log\frac{signal}{noise}\right) \tag{1.1b}$$

There is a variety of sources of noise present in pavement images acquired with a CCD line-scan cameras used for capturing pavement images. This noise is basically classified into (1) object-dependent noise and (2) object-independent noise. The photo-conversion process by which object light is converted into photoelectrons introduces object-dependent noise such as photon, thermal, and bias noise. On the other hand, object-independent noise such as quantization noise and read-out noise further contribute to the degradation of acquired pavement images. The key sources of noise attributing to the loss of digital image quality are shown in Figure 1.1.

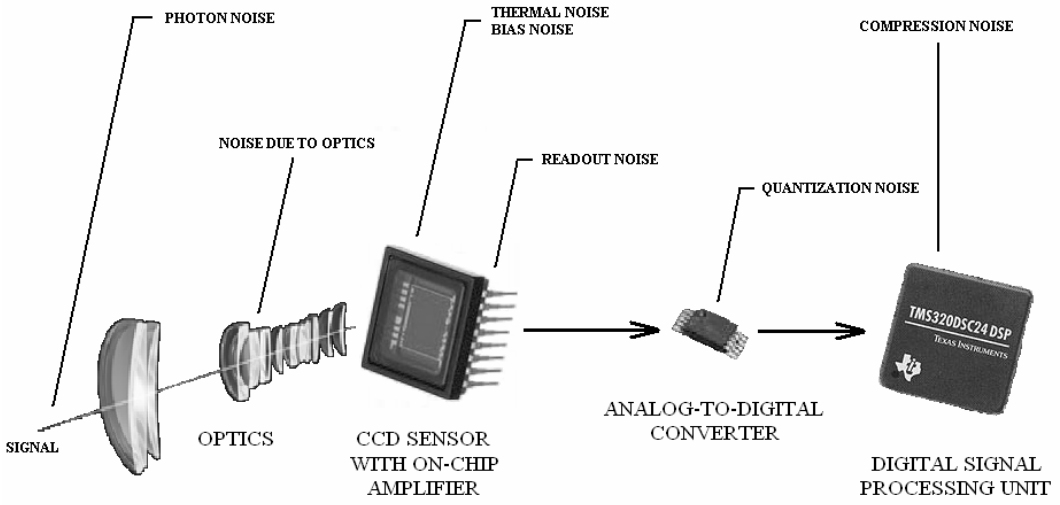

Figure 1.1 Sources of Noise in Digital Camera

1.2.1 Object-dependent Noise

1.2.1.1 Photon Noise

The photon noise arises from the statistical nature of photon production which is governed by the laws of quantum physics. The probability distribution of photons in an observation window of length T seconds can be closely approximated by a Poisson distribution, with a mean ρT where ρ is the photon flux or intensity measured in photons per second. The photons entering a given pixel of the CCD must be multiplied by the quantum efficiency (Q_e) of the CCD camera to determine the number of electrons detected (Deiries 2004). Hence the signal intensity can be expressed by

$$\mu = \rho Q_e T \tag{1.2a}$$

Since the Poisson distribution has the property that its variance is equal to its mean, i.e. $\sigma^2 = \mu$, the photon noise can be expressed by the standard deviation of the distribution of photons (σ) in the observation window T as:

$$\sigma_p = \sqrt{\rho Q_e T} \tag{1.2b}$$

1.2.1.2 Thermal Noise

The thermal noise is due to the random generation of thermal electrons at a given CCD temperature (Stein 2004). The probability distribution of thermal electrons is also a Poisson distribution where the rate parameter (ρ) is an increasing function of temperature. Therefore, thermal noise in a given pixel is equal to the square root of the number of thermal electrons generated within a given exposure time and it can be expressed as:

$$\sigma_T = \sqrt{DT} \tag{1.3}$$

where D and T represent the dark current (second^{-1}) and exposure time interval (seconds), respectively.

1.2.1.3 Bias Noise

There is a certain magnitude of electric potential difference that must be imposed on the chip so that each pixel can act as a photosensitive pixel able to gather electrons. The result of applying a potential difference on the chip causes an electron build-up in the pixels, even if no light is incident on the CCD sensor. The number of bias electrons which cause the bias noise remains

constant irrespective of the exposure time of the CCD chip, as long as the potential difference applied on the chip is constant.

1.2.2 Object-independent Noise

1.2.2.1 Read-out Noise

All electronic noise sources inherent to the digital camera and the CCD sensor are collectively referred to as read-out noise (N_r) and it represents the error introduced during the process of reading the signal from the sensor. The read-out noise of a typical CCD camera is about 15 electrons per pixel for every read-out process (Stein 2004). The standard model for this type of noise is additive and Gaussian. Mathematically, it can be expressed as;

$$\sigma = N_r \tag{1.4}$$

1.2.2.2 Quantization Noise

Noise that occurs in the analog-to-digital converter (ADC) (Figure 1.1) is called quantization noise. This type of noise is additive and independent of the signal when the number of image bits, $B \geq 4$. This is equivalent to a number of gray levels of $L \geq 2^B$ or $L \geq 16$. For a signal that has been converted to an electrical form and thus has minimum and maximum voltage values, the ADC is adjusted so that zero corresponds to the minimum voltage value and 2^B-1 corresponds to the maximum voltage value.

Quantization noise (σ_n) is directly expressed using the following SNR equation, which is derived from Eqn. (1.1b) (Young 1998):

$$SNR_{q_n} = 6B + 11 \ \ decibels \tag{1.5}$$

Quantization noise does not usually impact the overall *SNR* of a complete imaging system since the latter is typically dominated by the smallest *SNR* component of the digital camera. For example, the maximum SNR for the line-scan camera used in the FDOT MPSV with a preset JPEG (8-bit) image format depends on the quantization noise. Based on Eqn. (1.5), $SNR_{\max} = 6(8) + 11 = 59 \ dB$.

However, measurement of noise in the digital images from FDOT MPSV during its routine operations reveal SNR values much lower than 59 db which indicates many more sources of

noise than the quantization noise. The overall SNR evaluated for forward-view and pavement cameras of the FDOT MPSV under different lighting conditions and speeds on concrete and asphalt pavements are provided in Table 1.1. It is clear that the average SNR of each camera is dominated by sources of noise other than the quantization noise since the measured SNR is less than 59 db as computed above.

1.2.2.3 Background Noise

This background noise can arise from many sources and is usually scattered light that is not of interest to the observer. It can be quantified by the parameter R_{bg} which is the rate at which photons are incident on an average pixel from the background. Hence the background noise can be expressed by modifying Eqn. (1.2a) as;

$$\sigma_b = \sqrt{R_{bg} Q_e T} \tag{1.6}$$

1.3 Analytical Expression of Signal-to-Noise Ratio (SNR)

By substituting the expressions (Eqns. (1.2), (1.3), (1.4) and (1.6)) for all types of noise discussed above, except the quantization noise, in Eqn. (1.1a), a reasonable estimate of the SNR for the overall imaging system can be made (Roper Scientific 2003):

$$SNR_{overall} = \frac{\rho Q_e T}{\sqrt{\left(\rho + R_{bg}\right) Q_e T + \left[\left(DT\right) + \left(N_r^2\right)\right]}} \tag{1.7}$$

where T = exposure time interval (seconds),
D = dark current (second^{-1}),
ρ = photon flux or intensity measured in photons per second
Q_e = quantum efficiency
R_{bg} = rate at which photons are incident on an average pixel from the background, and
N_r = read-out noise

Under low-lighting conditions, read-out noise (N_r) exceeds the photon noise and the image is said to be *read-noise-limited*. If the read-out noise is the dominant noise for short exposure times T, Eqn. (1.7) can be simplified to:

$$SNR_{read\text{-}noise\text{-}limited} \cong \frac{\rho Q_e T}{N_r} \tag{1.8}$$

Table 1.1 Average SNR for FDOT MPSV Cameras under Different Field Conditions

Camera	Conditions	Average SNR (dB)
Forward-View (area-scan CCD)	Aperture F4.0 Aperture F8.0	50.8 35.7
	Aperture F1.5	39.9
Pavement (line-scan CCD)	Concrete pavement, sunny, pavement lights ON	28.5
	Concrete pavement, mostly sunny, pavement lights OFF	30.4
	Asphalt pavement, sunny with shadow overcast, pavement lights ON	20.0
	Asphalt pavement, sunny with shadow overcast, pavement lights OFF	30.4
	Asphalt pavement, cloudy, pavement lights ON	33.1
	Asphalt pavement, cloudy, pavement lights OFF	34.1

If the integration time is prolonged (Figure 1.2), photon noise exceeds the read-out noise (N_r) and at this point the image is said to be *photon-noise limited.* Then, Equation (1.7) can be written as:

$$SNR_{photon\text{-}noise\text{-}limited} \cong \frac{\rho Q_e}{\sqrt{\left(\rho + R_{bg}\right)Q_e + D}}\sqrt{T} \tag{1.9}$$

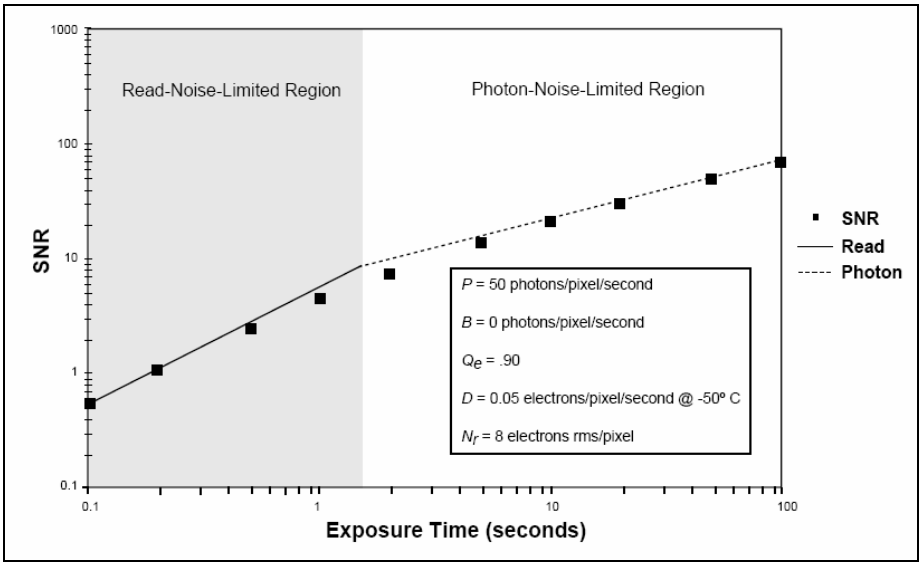

Figure 1.2 SNR vs. Exposure time for digital camera (Courtesy of Roper Scientific)

1.4 Enhancement of digital images

1.4.1. Linear mapping

Enhancement of the quality of pavement distress images is essential for improved accuracy of crack evaluation. The simplest image enhancement technique is linear mapping. Linear mapping involves the adjustment of brightness, contrast, or color in an image. The simplest operation on single pixels is linear mapping where the overall adjustment of brightness (*b*) and contrast (*c*) is made. Brightness is defined as a relative expression of the intensity of the energy output of a visible light source while contrast is defined as a variation in intensity of an image formed by an optical system. A general expression for brightness and contrast modification is as follows:

$$g_{m,n} = c \cdot z_{m,n} + b \tag{1.10}$$

where $g_{m,n}$ represents *post-processed* intensity value for a given pixel *(m,n)* and $z_{m,n}$ is the original intensity value of that pixel. If the brightness $b > 0$, the overall brightness is increased and if $b < 0$, it is decreased. Similarly, if $c > 1$, the contrast is enhanced, whereas if $c < 1$, it is reduced. Brightness and contrast modification are the simplest image processing operations that can be applied to a pavement distress image to improve its overall quality. These modifications will magnify the tiny residual variations in contrast to reveal enough detail to allow proper interpretation of the features, such as pavement cracks. An isolated pixel carries information on the intensity and color but it cannot express any information about the manner in which these properties vary spatially. Therefore, processes such as linear mapping cannot be used to investigate or control spatial variations in image intensity or color.

1.4.2 Convolution operation

One of the fundamental neighborhood operations of image processing is *convolution* which can be used to filter images and suppress noise. In convolution, the weighted sum of intensity values, or gray levels, from the neighborhood surrounding that pixel is evaluated. The neighborhood includes the pixel under consideration and it is generally symmetrical about the considered pixel (Efford 2000). Usually, a square neighborhood is selected with odd dimensions, e.g. 3 x 3, 7 x 7, etc. In this approach, the intensity values of the neighborhood of the considered pixel are weighted by coefficients that are elements of a matrix called the *convolution kernel.* The size of

the kernel determines a reasonable neighborhood but has to be small enough relative to the image size. During convolution, each kernel coefficient is multiplied by an intensity value from the neighborhood that defines the kernel. The effect of the convolution operation on any pixel (m,n) performed by a $p \times q$ kernel can be expressed as:

$$g_{m,n} = \sum_{k=-q}^{q} \sum_{j=-p}^{p} h_{j,k} z_{m-j,n-k} \tag{1.11}$$

where p and q are odd numbers that represent the width and the height of the kernel respectively and $h_{j,k}$ defines the normalized kernel. Further, $g_{m,n}$ is the post-processed intensity of the pixel (m,n). Finally, the kernel is then successively moved across the image until every pixel has been operated on. For the example, for a 3 x 3 neighborhood, the operation in Eqn. (1.11) can be expressed as:

$$g_{m,n} = \sum_{k=-1}^{1} \sum_{j=-1}^{1} h_{j,k} z_{m-j,n-k} \tag{1.12}$$

On the other hand, convolution operation can also significantly reduce the contrast of details of interest, such as cracks in a pavement, making their edges less well defined. This is because this technique of convolution is based on the assumption that most points in an image must be spatially coherent with their neighbors, a hypothesis that is not valid at the edge or feature points such as cracks (Owens 1997). Therefore, the use of alternative noise- filtering algorithms are required to enhance digital images that are used to evaluate pavements cracks and other distress features.

The most common image enhancement techniques such as Kalman or Wiener filtering techniques are based on the assumption of suitable noise quantification models (Lee 1981). On the other hand, the filtering technique developed by Lee (1981) based on the use of local statistics is more applicable in enhancing pavement distress or crack images. Lee's (1981) adaptive filtering technique is based on the use of the locally derived pixel intensity statistics (mean and variance). As part of the research documented in this report, the investigators modified the Lee (1981) method by using a new technique in which the pixel intensity statistics are obtained from a Standard Grayscale Target. In order to illustrate the above technique the concepts of probabilistic modeling of noise in digital images must be presented.

1.4.3 Probabilistic representation of noise

The intensity of digital images such as those from the FDOT MPSV can be theoretically separated using the following expression:

$$z_{m,n} = x_{m,n} + \omega_{m,n} \tag{1.13}$$

Where $z_{m,n}$ and $x_{m,n}$ represent the actual intensity and the noiseless intensity of a pixel *(m,n)* while $\omega_{m,n}$ is the noise in that pixel. If one can identify $\omega_{m,n}$, then one could determine the noiseless intensity as $x_{m,n}$. Consequently, various efforts have been made to describe $\omega_{m,n}$ using probabilistic methods.

For relatively high mean pixel intensities ($\mu \geq 20$), the noise in an imaging system can be assumed to be Gaussian and signal independent (Fisher et al. 2000). Then, in order to completely describe the distribution of noise from pixel to pixel, one must also determine the mean and the standard deviation of the noise distribution within the image.

1.4.4 Filtering Method Based on Local Statistics

In most filtering algorithms (ex. Kalman filtering), the mean and variance of $\omega_{m,n}$ (Eqn. (1.13)) is obtained from an assumed noise model while in the local-statistics method (Lee, 1981) the following algorithm is used to modify the intensity of a given pixel *(m.n)*.

$$\hat{x}_{m,n} = \bar{z}_{m,n} + k_{m,n}\left(z_{m,n} - \bar{z}_{m,n}\right) \tag{1.14}$$

Where $k_{m,n} = \dfrac{Q_{m,n}}{Q_{m,n} + \sigma^2}$ (1.15)

and $Q_{m,n} = E\left[\left(z_{m,n} - \bar{z}_{m,n}\right)^2\right] - \sigma^2$ (1.16)

It is noted that $\bar{z}_{m,n}$ is the mean pixel intensity of a local area surrounding the considered pixel (*m,n*) that is judged by the analyst to be uniform in intensity and σ^2 represents the noise variance of the population of similar pixels. The technique expressed in Eqns. (1.14)-(1.16) is

generally valid in low-contrast areas such as the non-cracked or non-distressed areas where the estimated pixel intensity value can be approximated by the local mean intensity value. However, to ensure that this algorithm is applicable in high-contrast areas such as cracked locations in pavement images, redefinition of the neighborhood must be implemented. Hence incorporation of an edge detection algorithm is essential for the implementation of the above algorithm for FDOT MPSV digital images.

As an example, it is seen from Figure 1.3 (a) that the point *(m,n)* is more likely to be a member of the subset of pixels in the unshaded area rather than the entire neighborhood. If the local mean and variance are computed based on pixels in the unshaded subset, the new $Q_{m,n}$ (Eqn. 1.16) would be considerably lower than the $Q_{m,n}$ obtained from the entire set. Hence the noise will be smoothened at the edge.

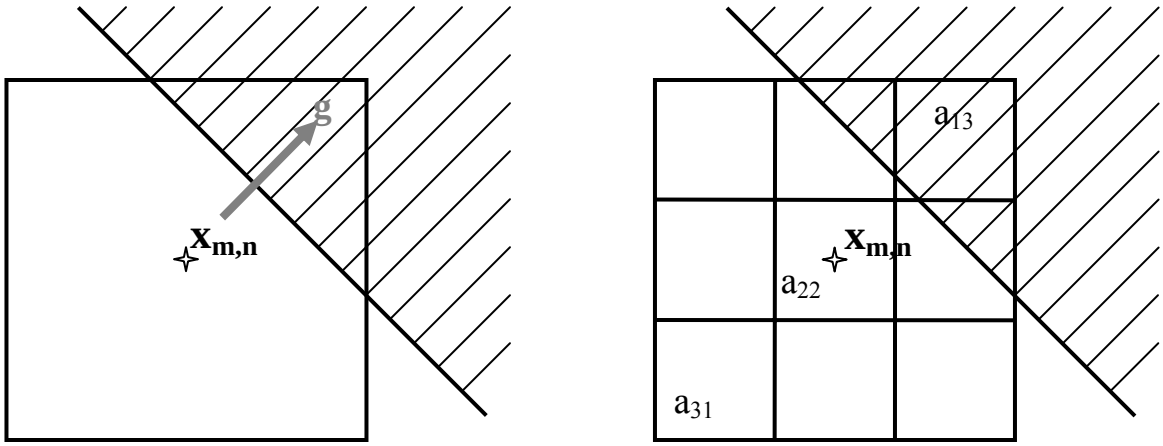

Figure 1.3 (a) High Contrast Neighborhood (9x9) of a Pixel; (b) Demarcation of 3 x 3 Sub-areas in the Neighborhood of Pixel in Figure 1.3(a)

1.4.5 Algorithm used for edge detection

In the edge detection algorithm used in the work reported here, for each pixel with a high local variance or high contrast over a preset threshold of pixels, gradients (of intensity) are computed in the local area in specified spatial orientations. The relative magnitudes of these gradients computed using well-defined gradient masks, would generally indicate the orientation of the

edge of a crack. The direction of the gradient mask with the maximum absolute value of the gradient is identified as the direction of the edge. Lee (1981) also introduced directional gradient masks for orientation intervals of 45 degrees. In this research, the investigators refined the directional indices proposed by Lee (1981) to evaluate the orientations (θ) at intervals of 15 degrees (Figure 1.4).

In the next step, the subsets of pixels (7x7) associated with each of the above orientations are defined in the neighborhood of the considered pixel. For the orientations indicated in Fig. 1.4, the directional subsets are illustrated in Fig. 1.5. Once an edge is identified based on the maximum gradient of intensity, the two subsets of pixels on either side of the crack edge are selected from Fig. 1.5. Finally it must be first determined to which of the above subsets the pixel under consideration belongs, based on how closely the mean and the variance of the pixel under consideration matches the local mean and variance on the above two subsets.

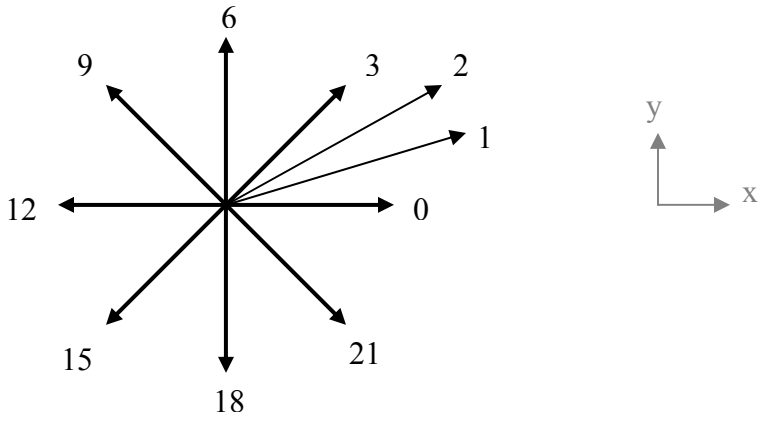

Figure 1.4 Modified Directional Indices

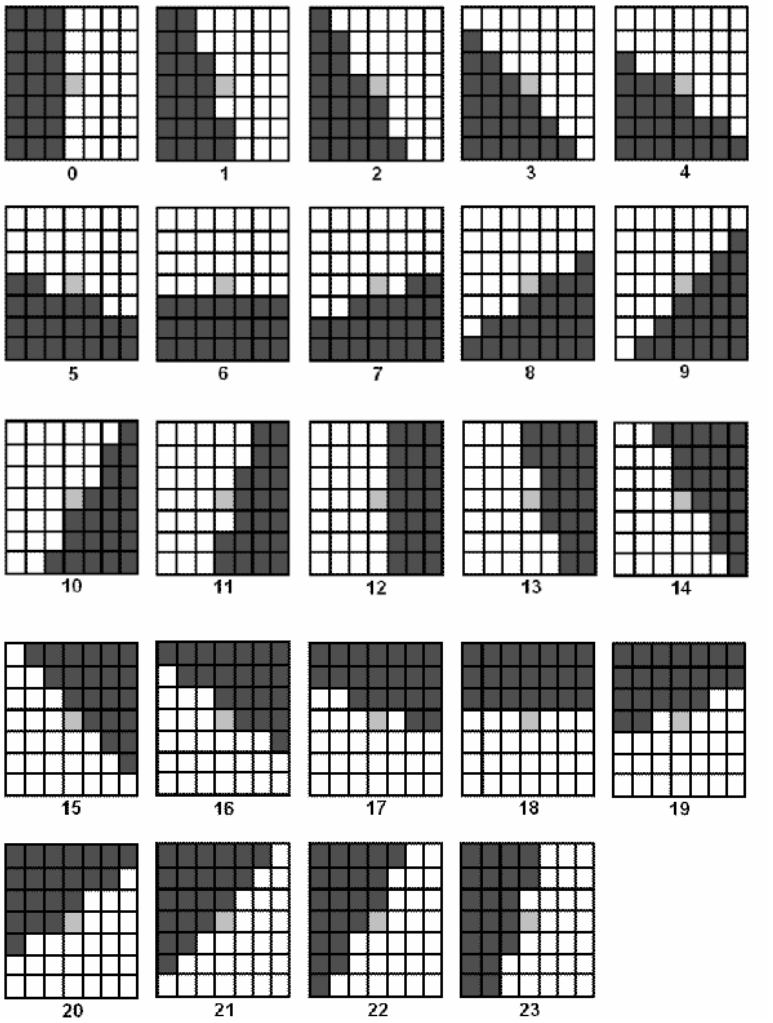

Figure 1.5 Definition of Directional Subsets (unshaded areas)

1.4.5.1 Computation of pixel gradients

As described above, a local-gradient mask is used to determine the edge orientation. To minimize the noise effect on the local gradient, 3 x 3 sub-areas as shown in Figure 1.3(b) can be demarcated. Then, a 3x3 gradient mask is applied to estimate the local means of these sub-areas as shown in Fig. 1.6. Then, to determine the direction of the gradient, Sobel kernels expressed in Eqn. (1.17) are applied to the means of the sub-areas as expressed by the *x* and *y* directional convolution operations in Eqns (1.18) and (1.19) (Sonka et al. 1999):

$$s_x = \frac{1}{4}\begin{bmatrix} -1 & 0 & 1 \\ -2 & 0 & 2 \\ -1 & 0 & 1 \end{bmatrix} \text{ and } s_y = \frac{1}{4}\begin{bmatrix} 1 & 2 & 1 \\ 0 & 0 & 0 \\ -1 & -2 & -1 \end{bmatrix} \tag{1.17}$$

$$g_{x_{m,n}} = s_x * z_{m,n} \tag{1.18}$$

$$g_{y_{m,n}} = s_y * z_{m,n} \tag{1.19}$$

The s_x kernel is sensitive to intensity changes in the *x* direction, or to edges running vertically while s_y is sensitive to intensity changes in the *y* direction, or to edges that run horizontally. To retain the gradient intensities, g_x and g_y within the usual intensity range of 0 - 255, the kernels s_x and s_y are normalized by a factor of ¼ (Eqn. 1.17). The gradients $g_{x_{m,n}}$ and $g_{y_{m,n}}$ can be considered as the components of a gradient vector **g** expressed by:

$$\mathbf{g} = \begin{bmatrix} g_x \\ g_y \end{bmatrix} \tag{1.20}$$

This vector is oriented along the direction of change and normal to the direction in which the edge runs. Hence the magnitude and direction of the gradient can be expressed as:

$$g = \sqrt{g_x^2 + g_y^2} \tag{1.21}$$

$$\theta = \tan^{-1}\left(\frac{g_y}{g_x}\right) \tag{1.22}$$

where θ is measured relative to the *x* axis (Figure 1.4).

Once the edge orientation is identified, the mean pixel intensities of the sub-areas (Figure 1.6) orthogonal to the edge are compared to determine on which side of the edge the considered pixel (m,n) must belong in. For the specific example in Figure 1.3(b), a comparison of $|a_{31} - a_{22}|$ and $|a_{13} - a_{22}|$ determines whether the relevant subset is in direction 3 or 15 (Figure 1.4). If $|a_{31} - a_{22}| < |a_{13} - a_{22}|$, then Subset 15 (Figure 1.5) will be chosen as the one which contains the pixel (m,n). Accordingly, all the pixels in the unshaded area of the Subset 15 (Figure 1.5) will be used in the computation of the local mean and variance. This will ensure that the intensity

variation among pixels of similar brightness would be less marked. Moreover, areas of inherently different brightness would acquire a much higher contrast, possibly leading to much easier identification of crack boundaries.

a_{11}	a_{12}	a_{13}
a_{21}	a_{22}	a_{23}
a_{31}	a_{32}	a_{33}

Figure 1.6 Mean Intensity Values of Sub-areas

For easier implementation of edge orientation identification, a 7 x 7 window within an image of a crack is very often preferred, with each sub-area containing a 3 x 3 pixel overlapping matrices, as shown in Figure 1.7.

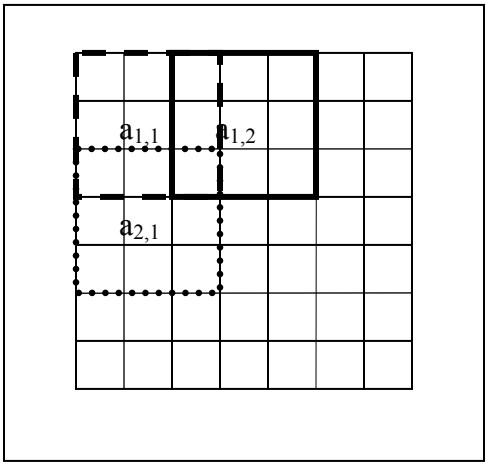

Figure 1.7 Overlapping of the 3 x 3 Sub-areas in the 7 x 7 Neighborhood

1.5 A Novel and Effective Technique for Determination the Variance of Noise

In most practical applications, the variance of noise, (σ^2) in Eqn. (1.16) is spatially variant and indeterminate. The method of determining σ^2 implemented in the technique developed by Lee (1981) is based on the assumption that the noise variance of a local area can be estimated reasonably well by the local variance of a more or less equally intense (flat) area. Therefore the implementation of the original Lee (1981) technique is cumbersome and time consuming, since one needs to evaluate each pixel in a 7 x 7 window for local mean and variance and then average the smallest variances to determine the population noise variance, σ^2.

An alternative approach was developed by the investigators to obtain the appropriate noise variance using evaluation of noise of the grayscale target (Figure 1.8). The implementation of this technique would result in an effective and practical noise filtering algorithm that will preclude the need for either apriori image modeling as in the case of Kalman or Wiener filtering techniques or the assumptions made by the adaptive filtering technique (Lee 1981).

Each patch of the grayscale target (Figure 1.8) represents a flat area (wedge) with a reasonably uniform optical density. Because imaging systems used in highway evaluation are not ideal systems, noise composed of undesirable signal components that arise from various sources described in Section 1.1 are introduced. As a result, slight variations in measured intensity values can occur even within a uniform wedge or patch of the target. Therefore, any variation from the mean value for a given wedge represents the variance $\left(\sigma^2\right)$ of the noise.

Figure 1.8 Fifteen-wedge Grayscale Target

For each wedge, the mean and variance of intensity can be computed using image editing software such as the *ImageJ* (Rasband 2004), as shown in Figure 1.9 (a) and 1.9 (b).

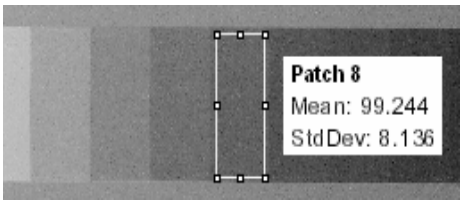

(a)

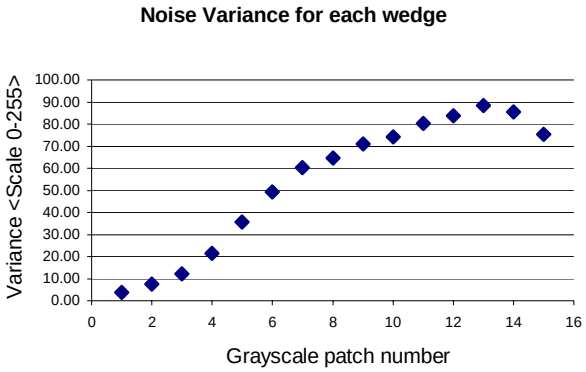

(b)

Figure 1.9(a) Evaluation of the Mean and Standard Deviation of the Intensity of One Patch Using *ImageJ* Software; (b) Plot of Variances of Each Patch of the Grayscale Target

After the subset mean is computed for a pixel of an image under consideration using Eqn (1.14), the noise variance $\left(\sigma^2\right)$ of any pixel of that image can be determined through linear interpolation of noise variance values in Figure 1.9(b) corresponding to the patches with the closest mean intensity. This method would provide a more precise estimate of the true level of noise for a given pixel than Lee's (1981) method which assumes the variance to be the average of the five smallest variances computed from 7 x 7 window in the neighborhood. The latter assumption would hold better if all the pixels used for computation of the mean value and variance were originally represented by the flat area and any change in intensity values was due to noise. On other hand, this is in fact the case for each uniform wedge of the grayscale target since any deviation of the signal is caused by different sources of noise described in Section 1.1.

In deducing the magnitude of noise in a given pixel in an image under consideration, it is assumed in the new method that the σ^2 of the intensity (or noise) is the same as that of the grayscale wedge with a mean intensity value approximate equal to the intensity of that pixel. In the opinion of the investigators, the above assumption can be justified by comparing the image enhancements accomplished by the new technique with those obtained from the existing techniques.

Moreover, the new method is also more efficient than the Lee (1981) method as one can preclude the need for computation of mean and variances for each pixel inside of 7 x 7 window.

1.5.1 Illustration of the Target-based Filtering Technique

An example of a vertical noisy edge (Figure 1.10 (a)) in a 7 x 7 window (Figure 1.10 (b)) is provided to illustrate the application of the concepts discussed in the previous sections. The image is that of an Edmund Optics Optical Density Target. A Minolta DiMage5 camera was used for capturing this image in a non-compressed TIFF format. The sensitivity of the camera was set to an equivalent of ISO800 at which the noise is most visible. Then, *ImageJ's* plugin *PhotoES_AM* programmed by the investigators was used for evaluating the mean and variance values for each patch and also for intensity updating computation associated with the process described in Eqns. (1.14) – (1.16).

The intensity values for pixels inside the window (Figure 1.10 (b)) are shown in Table 1.2. Pixel $(4,4)$ highlighted in Figure 1.10(b) has been chosen to illustrate the novel noise filtering method presented in this chapter.

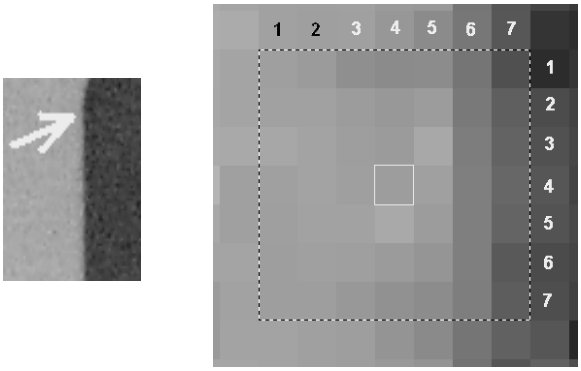

(a) (b)

Figure 1.10 (a) Evaluated Image; (b) Zoomed-in 7 x 7 Window with the Pixel Under Consideration at its Center

Table 1.2 Intensity Values for 7 x 7 Window with the Central Pixel Highlighted

158.72	155.03	140.17	135.18	137.40	115.24	80.08
160.24	160.07	153.18	145.01	153.54	119.85	94.49
166.27	162.37	156.05	149.29	166.16	123.82	97.88
158.70	163.23	157.82	155.06	158.51	126.33	101.06
157.39	162.15	161.72	167.25	153.70	125.31	98.71
157.01	160.04	158.80	153.74	145.85	123.44	85.74
158.23	158.00	151.85	144.13	137.25	121.57	90.42

The intensity value of central pixel (4,4) under consideration is 155.06. If local statistics are used in filtering (Lee, 1981), the mean and the variance of the 7 x 7 area are given by $\overline{x}_{4,4} = 141.29$ and $\sigma^2_{orig} = 590.74$. Next, the 3 x 3 mask (Figure 1.6) is applied to obtain the mean values of the sub-areas $(a_{11}, a_{12}, \ldots, a_{33})$ as shown in Table 1.3.

Table 1.3 Mean Values of the Sub-areas

156.9	148.4221	120.94
160.633	158.396	127.942
158.354	152.699	120.221

By applying Eqns (1.17) – (1.22), the magnitude and direction of the gradient are evaluated as $g = 34.95$ and $\theta = -4°$ respectively. The gradient direction of -4° approximately corresponds to the directional index of 0 (zero) as shown in Figure 1.4. To determine on which side of the edge the pixel under consideration a_{22} is located, the value of $|a_{22} - a_{21}| = 2.24$ is compared to the value $|a_{23} - a_{22}| = 30.45$. Therefore, based on the criterion defined in Section 1.4, the pixel under consideration must lie on the left of the edge. Thus, out of the directional subsets of the 7 x 7 window (Table 1.2) the subset that is most appropriate for the estimation of the mean and variance of the pixel $(4,4)$ is selected from Fig. 1.5 as the Subset 12. This subset is separately shown in Table 1.4.

Table 1.4 Intensity Values for the Relevant Directional Subset 12

158.72	155.03	140.17	135.18
160.24	160.07	153.18	145.01
166.27	162.37	156.05	149.29
158.70	163.23	157.82	155.06
157.39	162.15	161.72	167.25
157.01	160.04	158.80	153.74
158.23	158.00	151.85	144.13

The mean intensity ($\bar{x}_{sub}$) and the variance (σ^2_{sub}) of the relevant subset are 155.95 and 55.81 respectively. This represents a reduction of σ^2_{orig} by a factor of 10 when compared to the original variance, σ^2_{orig} , of 590.74.

In the following section, the noise variance σ^2 (Eqn. (1.16)) will be determined using the method described in Section 1.5.

1.5.2 Determination of variance using the Grayscale Target

First, the image of the Edmund's Optics Density Target is captured by a digital imaging system and then loaded into *ImageJ* imaging software. Then, the mean and variance values are computed for each wedge and the results are shown in Table 1.5 and Figure 1.9 (b).

Table 1.5 Statistics of Luminance Values of the Gray-scale Target

PATCH	AVE_SCALE_MEAN	AVE_SCALE_VAR
1_white	221.67	3.80
2	206.47	7.55
3	193.44	12.08
4	170.08	21.41
5	144.43	35.61
6	121.74	49.21
7	104.50	60.31
8	94.96	64.60
9	81.76	70.87
10	74.44	74.34
11	65.69	80.27
12	60.22	83.84
13	53.37	88.36
14	50.38	85.63
15_black	48.39	75.43

Since the mean intensity of the subset where the pixel under consideration belongs, $\bar{x}_{sub}$, is 156, the corresponding noise variance obtained from Table 1.5 through linear interpolation is $\sigma^2 = 29.21$. Using Eqn. (1.16), the variance of directional subset $\left(Q_{4,4}\right)$ is determined to be 26.6. Finally, using Eqns. (1.14) and (1.15), the modified intensity value $\left(\hat{x}_{4,4}\right)$ for pixel $\left(4,4\right)$ is estimated to be 155.5.

1.5.3 Verification of the Filtering Technique

The above filtering technique was coded in *PhotoES_AM* plugin of *ImageJ* software (Rasband 2004). To illustrate applicability of the proposed filtering technique, two sets of tests were conducted. First, a synthetic image (Figure 1.11) was created in the Microsoft Paint program so that background and feature intensity values are equal to 130 and 42, respectively. Then, using the *Add Noise* built-in function of the *Jasc Paint Shop Pro* program (Jasc Software 2004), three different magnitudes (5%, 10%, and 15% of coefficients of variation) of Gaussian noise were introduced artificially into the original image. The different levels of noise could perhaps be correlated to the severity levels of cracks. However, this task was beyond the scope of this research.

Finally, these noisy images were filtered using the *PhotoES_AM* plugin under *ImageJ* image editing software and then the SNR for both noisy and filtered images were computed and the results are presented in Table 1.6. The effectiveness of the noise removal technique is illustrated in Figure 1.12.

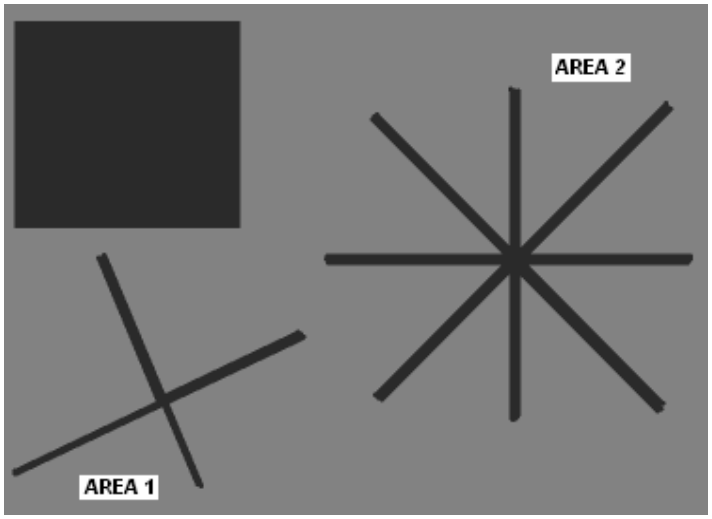

Figure 1.11 Verification of the Filtering Technique

Table 1.6 Results of the Noise Filtration Test on Synthetic Image

Area	Coefficient of Variation	Type	SNR Background [dB]	SNR object [dB]	SNR Improvement Background [dB]	SNR Improvement Object [dB]
Area 1	5%	Before	29.1	29.0	-	-
		After	42.1	40.9	13.0	11.9
	10%	Before	21.6	21.5	-	-
		After	35.2	29.9	13.6	8.4
	15%	Before	17.9	18.0	-	-
		After	32.3	29.7	14.4	11.7
Area 2	5%	Before	29.1	29.0	-	-
		After	42.8	38.4	13.7	9.4
	10%	Before	21.9	21.7	-	-
		After	36.3	34.4	14.4	12.7
	15%	Before	17.9	17.7	-	-
		After	32.2	27.0	14.3	9.3

Table 1.6 shows that the improved filtering technique based on the local statistics and the use of grayscale target do improve the image quality of both the object representing the crack and background substantially.

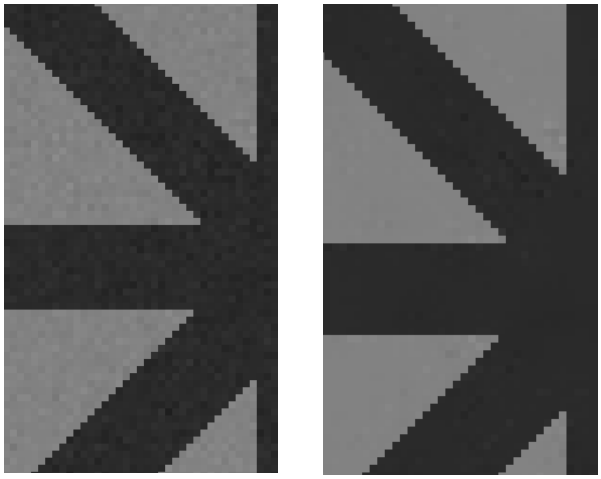

(a) noisy image (5%) (b) filtered image

Figure 1.12 Example of Noise Removal from Synthetic Image

The second evaluation was based on removal of noise from actual pavement images captured by the FDOT MPSV. Figures 1.13 and 1.14 show examples of noise filtration from concrete and asphalt pavements, respectively.

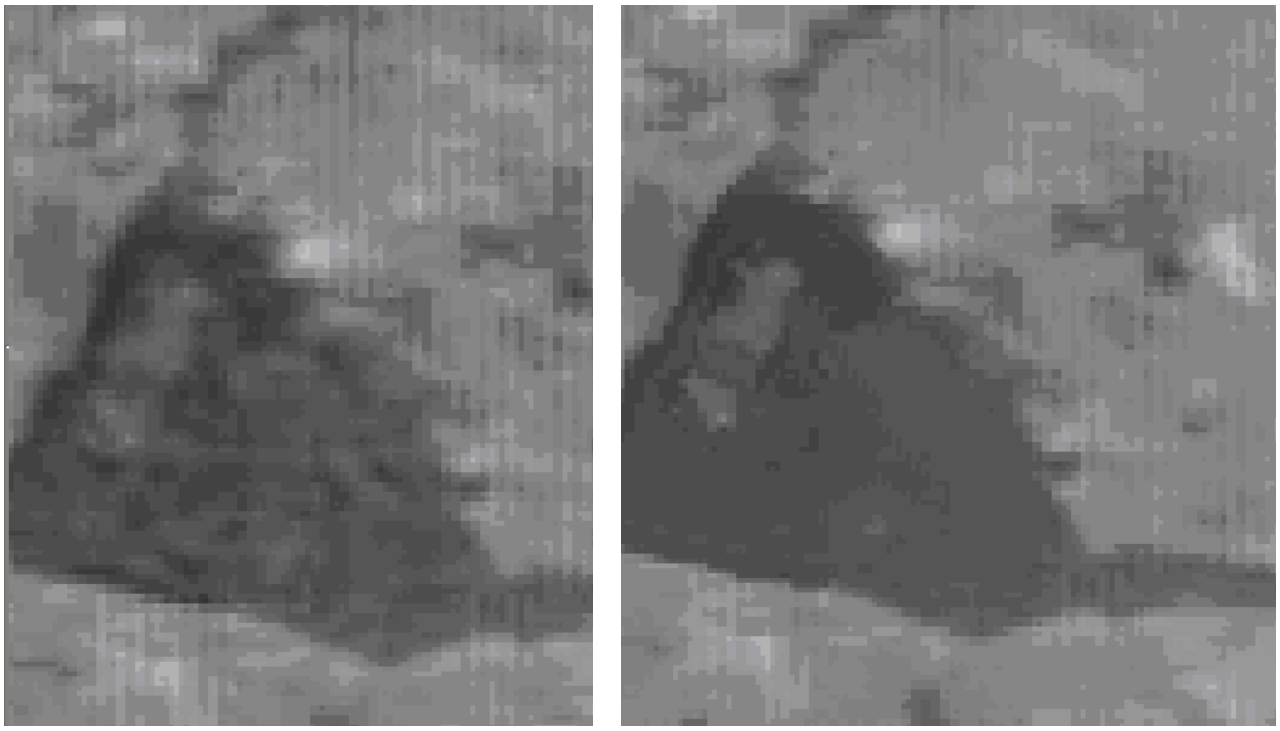

(a) original image (b) filtered image

Figure 1.13 Example of Noise Removal from PCC Pavement Image

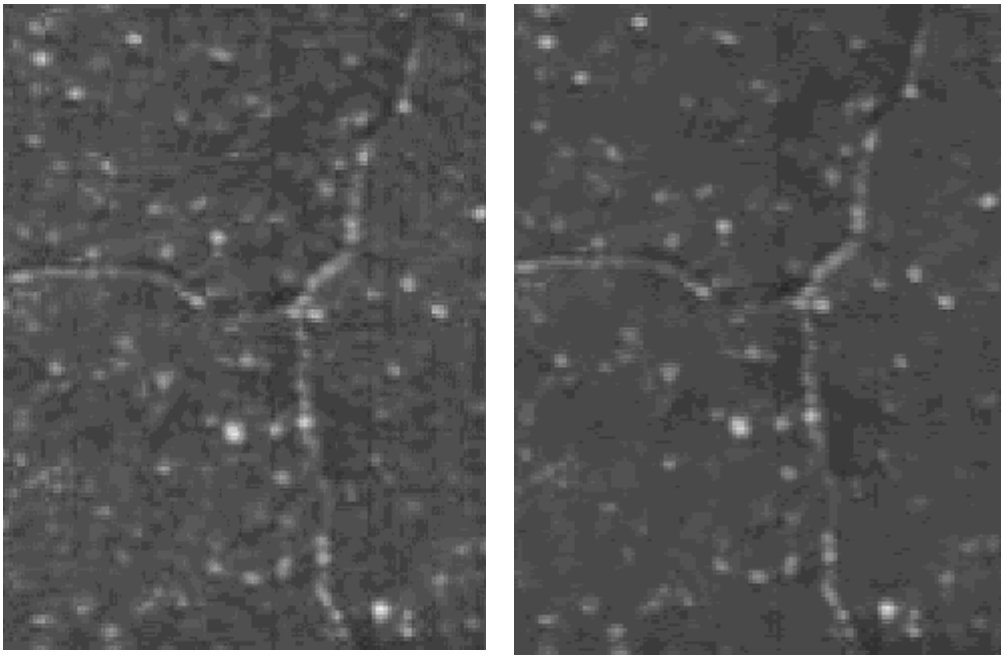

(a) original image (b) filtered image

Figure 1.14 Example of Noise Removal from Asphalt pavement

1.6 Application to digital images of the FDOT MPSV

The results presented in the preceding section indicate that the new image enhancement technique, which employs (1) the edge location algorithm, (2) local pixel intensity statistics derived after edge location, and (3) the corresponding intensity measurements from the grayscale target, is potentially effective in improving the quality of pavement crack images. However, programming of this enhancement technique was beyond the scope of this investigation. Therefore, if one can accomplish the automation of the new enhancement technique, then one would be able to incorporate the following procedure recommended by the investigators, in pavement crack evaluations.

1. Demarcate the areas of pavement where crack evaluation is desired.
2. Place the grayscale target on a control section of the pavement so that the FDOT MPSV would capture the image of the target and the cracks under the same conditions.
3. Use the automated version of the new enhancement procedure to enhance all the images.
4. Evaluate the pavement cracks at an improved accuracy.

It will be shown in Chapter 2 that lower SNR values generally result in improved crack evaluation accuracy. Hence the newly developed image enhancement technique would be a valuable tool in automated crack evaluations.

CHAPTER 2
EVALUATION OF THE MPSV PAVEMENT IMAGING SYSTEM

2.0 Introduction

The efficiency and accuracy of crack evaluation depends not only on the quality of pavement images but also on the accuracy and precision of the imaging system. Although digital imaging technology has evolved vastly during the recent years, there are no definitive standards to gauge the accuracy and precision of a given imaging system. Therefore, the objective of the second phase of the investigation was to conduct an experimental program designed to determine the precision and accuracy of the pavement imaging system.

2.1 Design of Experiment

In order to explore the optimum conditions for vehicle operation, the imaging system was tested under the following evaluation conditions:

(1) different lighting conditions (sunny, cloudy, and overcast),

(2) with and without the pavement lighting system,

(3) different vehicle speeds (25 mph, 35 mph, and 45 mph), and

(4) different pavement types (asphalt and concrete).

Table 2.1 illustrates the experimental combinations. All the other significant variables such as the aperture setting, focus setting, etc. were fixed while the gain and exposure time were regulated automatically by the image capturing software to suit the lighting conditions. A secondary objective of this research task was to evaluate the effect of vehicle vibration and the image distortion on the quality of images. For this purpose a grid of small bright colored tacks was set up at one test site location of the relatively new asphalt (Figure 2.1b) pavement.

Table 2.1 Description of Experimental Conditions

Test Section	Direction	Date	Surveying Time	Pavement Type	Lighting Conditions	Pavement Lighting System	Speed [mph]
SR 28	South	05/18	11.33 – 12.15 pm	Concrete	Sunny	On	25, 35, 45
SR 28	South	05/18	12.19 – 12.35 pm	Concrete	Sunny	Off	25, 35, 45
SR 331	North	05/18	03.25 – 03.45 pm	Asphalt	Cloudy	Off	25, 35, 44
SR 331	North	05/18	03.50 – 04.10 pm	Asphalt	Cloudy	On	25, 35, 43
US 441	North	05/19	10.45 – 11.05 am	Asphalt	Overcast	On	25, 35, 45
US 441	North	05/19	11.11 – 11.40 am	Asphalt	Overcast	Off	25, 35, 45

First, the three (3) selected pavement test sections were temporarily closed for traffic during testing. Then, longitudinal, transverse, and alligator crack patterns were designated in the selected pavement sections and a number of selected features were manually traced on a transparent paper to determine the crack dimensions (both length and width). In selecting the crack features it was assured that they covered a wide range of sizes. Then in order to verify the manual measurements, the cracks were imaged by a hand-held Minolta DiMage5 3.3-megapixel camera and saved as uncompressed TIFF files. In addition, poster boards containing the grayscale standard target (Figure 2.1(a)) were placed in front of the selected crack locations so that the FDOT MPSV would image the targets prior to imaging the selected cracks. Intensity data obtained from the images of these targets would be useful in quantifying the effect of noise on images. The vehicle performed three (3) replicate runs at each speed to account for statistical variations and evaluate the repeatability (precision) of the pavement imaging system.

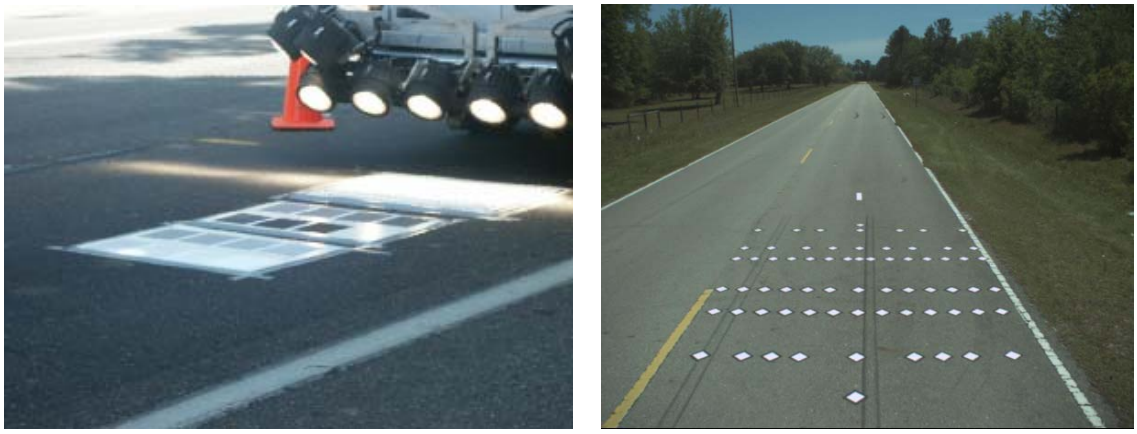

(a) (b)

Figure 2.1 (a) FDOT MPSV Driven Through the Testing Area; (b) Testing Area for Evaluation of Image Distortion

Finally, the FDOT MPSV was driven over the tested area (Figure 2.1(a)) while capturing the images of the targets and the cracks under the experimental combinations in Table 2.1. Subsequently, the acquired data were analyzed to test the quality of the images and verify the accuracy of the pavement camera in recording crack information, based on the following criteria:

(1) Signal-to-Noise Ratio (SNR) of the pavement images. SNR is defined as the ratio of the mean and the standard deviation of the intensity of various pixels in an image (Equation 1.1),
(2) Evaluated crack length – based on the measured lengths of the cracks from the imprint on the transparency and the image. The software ImageJ [Rasband, 2005] was employed to determine the length of a given crack based on the number of pixels forming its image,
(3) Evaluated crack width – based on the measured width of the cracks as in the case of crack length, and
(4) Degree of distortion of the crack image – based on the measurements made on the grid of tacks (Figure 2.1(b)) and comparison with the corresponding dimensions of its image.

2.2 Evaluation of pavement image quality

2.2.1 Evaluation of Image Quality Due to the Lighting System

Noise is referred to as the unrelated energy fluctuations that can occur during image capture, transmission, or processing (Section 1.1). At a pixel level, noise is a random variation in the charge on a pixel that is due to factors other than the pavement being captured. At the image level, noise manifests itself by a random detail in an image that deviates from the real detail that originates from the scene being captured. At a certain level of noise, an experienced technician or automated detection software will fail to accurately recognize and distinguish pavement distress from its background. Therefore, noise reduces the quality of digital image noticeably. Signal to Noise Ratio (SNR) is a single number that reflects the quality of captured image by comparing relative magnitude of signal and noise. As described in Eqn. (1.2), SNR is commonly expressed as a logarithmic measure in decibels (dB):

$$SNR = 20\left(\log \frac{signal}{noise} \right) \tag{2.1}$$

In this study, the quality of pavement images was measured objectively by the SNR of the grayscale target shown in Fig. 2.1(a). This is because the images of the black and white patches of the grayscale target provide areas of more or less uniform intensity with any intensity variation within each patch attributed to noise only. Therefore, during the entire experimentation, the grayscale target was placed next to the areas to be evaluated and the image of the grayscale target was analyzed for SNR. Figure 2.2 shows a sample variation of SNR on US 441 at a speed of 45 mph based on the average from the three (3) repeated trials under specific lighting conditions. Similar plots were also developed for the other testing locations and speeds and results of the repeatability study are presented in Table 2.2.

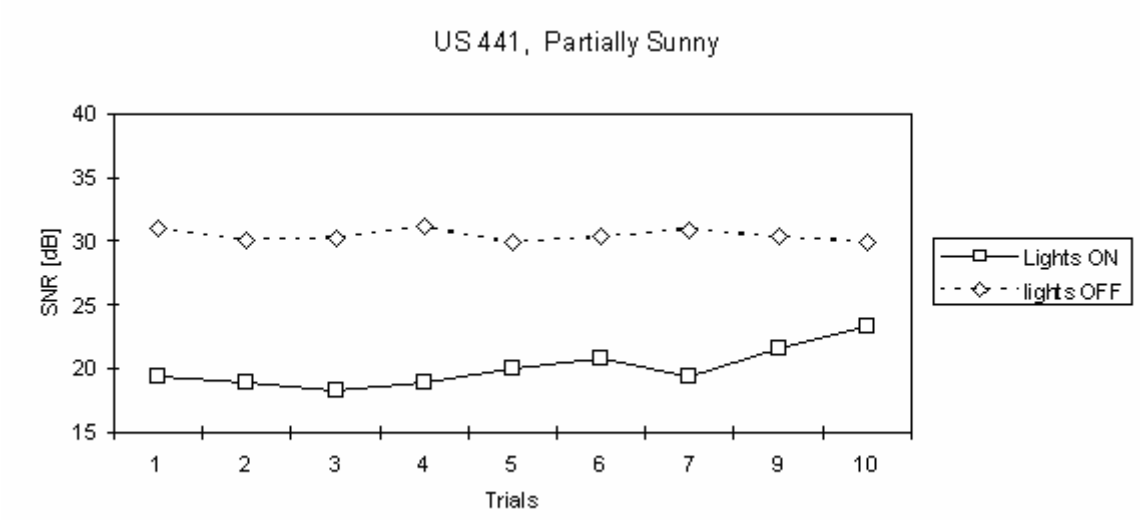

Figure 2.2 Repeatability of SNR Variation on US 441 (Exposure 1/40,000 sec, 45 mph)

Table 2.2 Repeatability of SNR Measurements (Speeds of 25, 35 and 45 mph)

Road ID	Surface Type	Lighting Conditions	Pavement Lighting	Coeff. of Variation of SNR	% Max Error Based on Mean for All Speeds	95% Confidence Interval of the Error (as % of mean)	Average Error in Distance Before Correction (mm)	Average Error in Distance After Correction (mm)	Improve-ment (%)
US 441	Asphalt	Overcast	On	0.07	24.5	14%	3.4	1.3	60.5%
			Off	0.0	3.9	0%	3.0	1.2	60.2%
SR 331	Asphalt	Cloudy	On	0.01	10.0	20%	2.7	1.2	53.4%
			Off	0.01	13.3	20%	4.1	1.4	65.1%
SR 28	Concrete	Sunny	On	0.04	20.7	8%	1.7	0.7	54.6%
			Off	0.03	27.9	6%	2.1	0.9	56.9%

Table 2.2 shows that the coefficient of variation SNR (Column 5) of pavement images is significantly low among repeated runs under any given ambient and artificial lighting condition. The results in Table 2.2 also shows that the maximum percentage error based on the mean (Column 6) among repeated runs under a given set of testing conditions is less than 27.9%

illustrating the repeatability of the quality of captured digital images . Figure 2.3 (for US 441) and the corresponding results for SR 331 and SR 28 (Mraz, 2004) indicate that, when the pavement lighting system is on, there is a tendency for SNR to be lowered for all runs in both asphalt and concrete pavements under any outside lighting condition. Although artificial light reduces SNR, it will be shown later that the user will benefit from its usage in low-light conditions when absence of the artificial light would disable crack evaluation or decrease the accuracy of it. Moreover, the usage of the artificial light helps to minimize shadow overcast by the objects on the side of road or survey vehicle itself. Later, it will be illustrated that the average SNR at any given speed would be reduced with the pavement lighting system.

2.2.2 Evaluation of Image Quality With Respect to Speed

The SNR measurements were also used to evaluate the effect of the vehicle speed on the quality of pavement images. The average SNR value from repeated runs on each individual testing condition was determined and the results for US 441 are presented in Figure 2.3. For Basler L-103 line-scan camera the maximum SNR based solely on the quantization noise would be 59 dB (Young, 2005) and Equation 1.5 (Chapter 1). However, it was also shown in Chapter 1 (Table 1.1) that due to the presence of other sources of noise, the measured SNR value is seen to be significantly lower than the above maximum value. Based on all the plots exhibiting the relationship of SNR versus speed, similar to Figure 2.3, the computed standard deviations and the corresponding coefficients of variation of SNR are indicated in Table 2.3. From Table 2.3 it can be concluded that the SNR and hence the image quality does not indicate a significant systematic dependence on the vehicle speed. Moreover, based on the results presented in Figures 2.3 and similar figures for other roadways (Mraz, 2004), it was concluded that the lighting system of the vehicle does introduce a reduction in SNR of 10 dB for asphalt pavements under overcast conditions, presumably due to the presence of photon noise and saturation effects. Since

the SNR of a crack image will be correlated in this work to the accuracy of crack evaluations based on that image, one would expect the artificial lighting system to improve the accuracy of crack evaluation under overcast conditions.

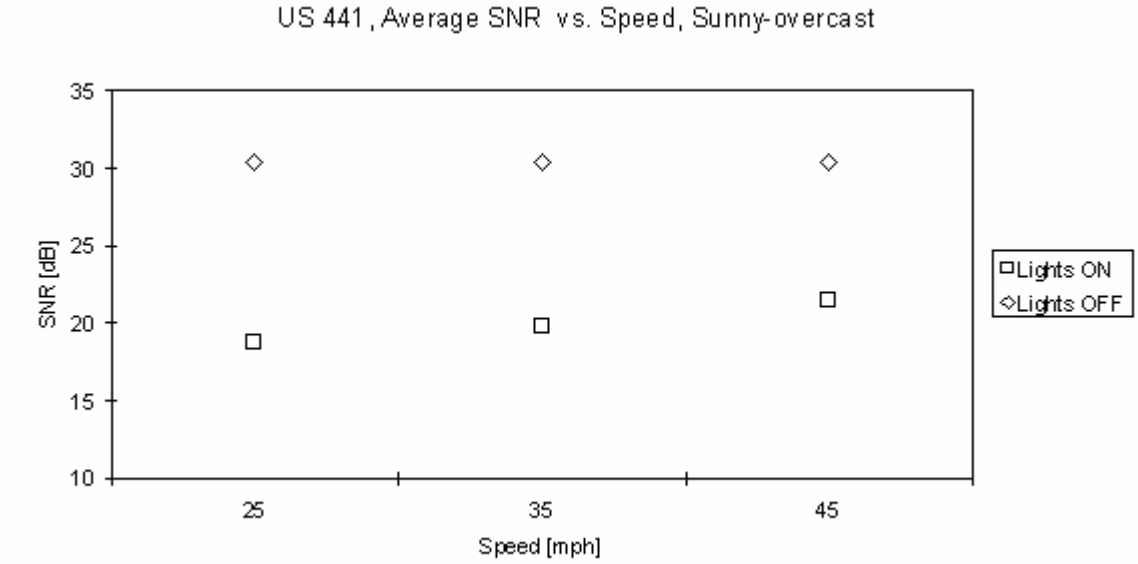

Figure 2.3 SNR vs. Speed Plot for US 441

Table 2.3 Variation of Average SNR with Speed

Road ID	Surface Type	Lighting Conditions	Pavement Lighting	Std. Deviation			Coefficient of Variation			% Max Error Based on Mean SNR		
				Speed (mph)								
				25	35	45	25	35	45	25	35	45
US 441	Asphalt	Overcast	On	0.6	1.0	1.9	0.3	0.9	3.6	6.0	1.0	7.0
			Off	0.5	0.6	0.5	0.2	0.4	0.3	0.0	0.0	0.0
SR 331	Asphalt	Cloudy	On	1.8	1.5	0.4	3.2	2.3	0.2	1.0	0.4	1.4
			Off	0.3	0.3	2.2	0.1	0.1	4.9	0.8	0.1	0.7
SR 28	Concrete	Sunny	On	2.0	1.5	0.8	4.2	2.3	0.7	4.1	2.6	1.5
			Off	0.2	3.8	3.7	0.0	14.4	14.0	3.1	3.2	0.1

2.3 Evaluation of pavement image for crack measurements

2.3.1 Verification of Manual Survey

In the next test, the accuracy of crack evaluation based on the images captured by the FDOT MPSV was investigated. First, the widths and lengths of crack features traced on a transparent paper during the manual survey were measured between distinctive points. Next, the images of the same features captured by the hand-held Minolta DiMage5 3.3-megapixel camera (Figure 2.4(a)), were also evaluated. Then, using image measurements, the sizes of the same features were re-computed based on the common lens equation (Mraz, 2004). The investigators feel that the latter technique provides more accurate means of evaluating crack features than manual measurements of the traced cracks. Therefore, the results of the manual survey were verified by comparing the sizes of the features from the manual survey with the corresponding ones computed from the images of the hand-held Minolta DiMage5 digital camera. The magnitude of the error for the length and width of most crack features was found to be less than 10%. Therefore, it was concluded that the manual survey was reasonably accurate and provides a sound basis for determining the accuracy of the same measurements obtained from pavement images. Above all, these results also ascertain the validity of the analytical techniques that were employed to measure distances from digital images.

2.3.2 Repeatability (Precision) of Crack Evaluation

After verification of the manual measurement of crack widths and lengths, the same features were evaluated from the images captured by the pavement imaging system of the FDOT MPSV. First, the repeatability (precision) of crack measurements was studied by comparing the evaluation of the same pavement features during three repeated runs at 25, 35 and 45 mph. The results of this comparison for US 441 are shown in Tables 2.5 and 2.6. Table 2.7 summarizes the results of the repeatability study for all three sections with the features categorized based on the

AASHTO crack severity designations. Table 2.4 describes the notation used for identification of crack features.

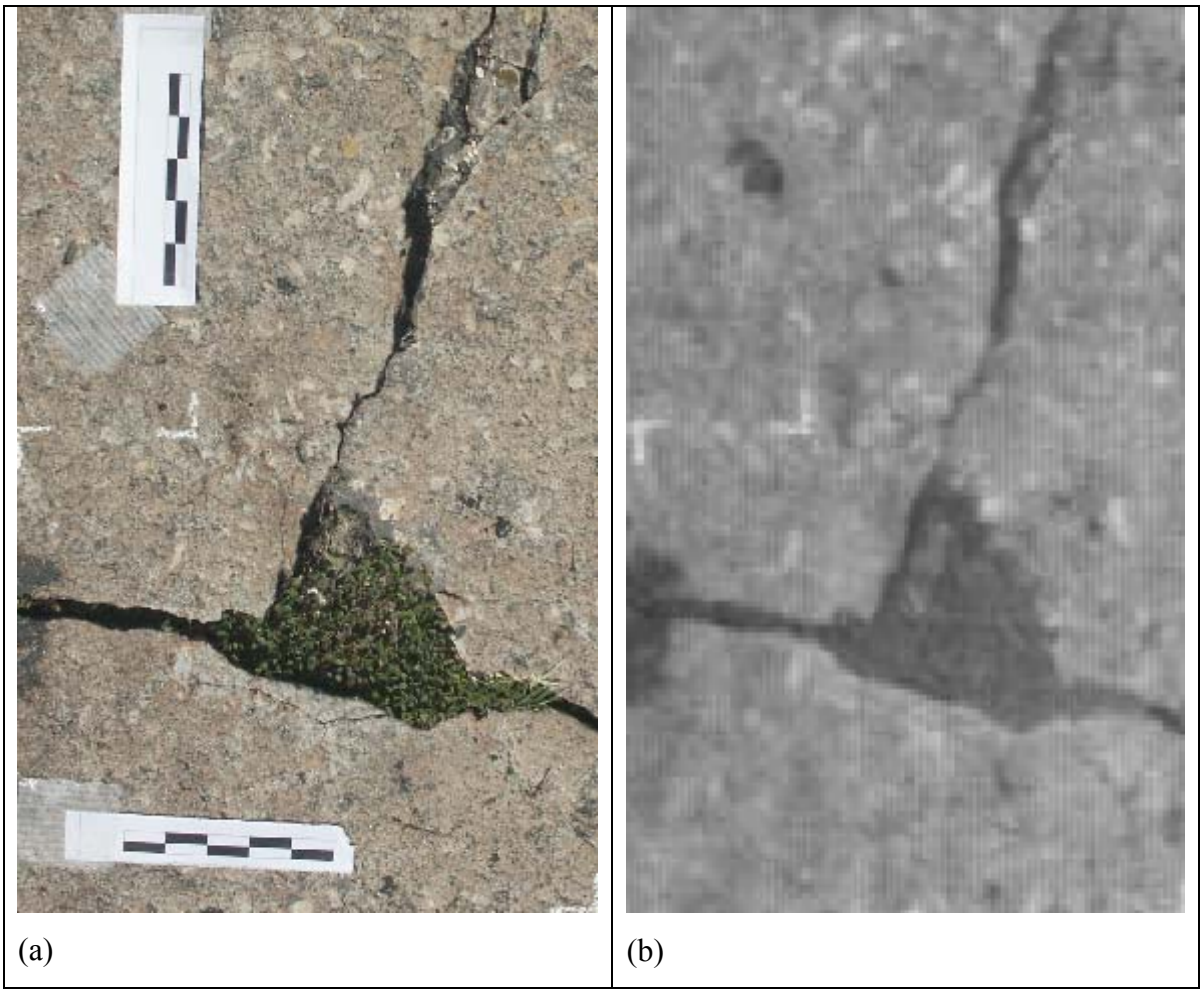

(a) (b)

Figure 2.4 Example of Pavement Captured by (a) Minolta DiMage5, and (b) Line-scan Camera of FDOT MPSV

Table 2.4 Definition of Notation Used in Figure 2.5 and Tables 2.5, 2.6, 2.8, and 2.9

Notation Name	Description
a_vert1 – a_vert3	US 441 sections C, D, E, longitudinally oriented ruler
a_hor1 – a_hor3	US 441 sections C, D, E, transversally oriented ruler
a_c1_w, a_c2_w	US 441 section C, width of cracks 1 and 2
a_d8_w – a_d10_w	US 441 section D, width of cracks 8 – 10
a_e1_w, a_e2_w	US 441 section E, width of cracks 1 and 2
a_e3_t, a_e5_t	US 441 section E, length of cracks 3 and 5
a_f1_w, a_f3_w, a_f5_w	US 441 section F, width of cracks 1, 3, 5
c_a1_w, c_a2_w, c_a4_w	SR 28 section A, width of cracks 1, 2, 4
c_c3_w – c_c5_w, c_c7_w – c_c9_w	SR 28 section C, width of cracks 3 – 5 and 7 – 9
c_d1_w – c_d3_w, c_d5_w	SR 28 section D, width of cracks 3, 4, 8
a, b, c, d, e	represents locations containing at least one distress measured manually
1, 2, 3, …, 10	identification number of the particular distress measured manually

Table 2.5 Crack Measurements at Different Speeds (US 441, lights off)

Crack Feature ID	Dimensions from Line-scan Camera Image											
	25 mph				35 mph				45 mph			
	Run 1	Run 2	Run 3	Variation from Mean (%)	Run 1	Run 2	Run 3	Variation from Mean (%)	Run 1	Run 2	Run 3	Variation From Mean (%)
a_f1_w	-	-	-	-	-	-	-	-	-	-	-	-
a_f3_w	-	-	-	-	-	-	-	-	-	-	-	-
a_f5_w	-	-	-	-	-	-	-	-	-	-	-	-
a_vert1	17.0	17.0	18.9	10.7	18.9	17.0	17.0	10.7	18.9	18.9	17.0	10.3
a_vert2	17.0	17.0	17.0	0.0	18.9	18.9	15.1	21.4	15.1	17.0	17.0	11.5
a_vert3	18.9	18.9	18.9	0.0	18.9	18.9	15.1	21.4	18.9	18.9	18.9	0.0
a_hor1	20.8	22.7	22.7	8.6	24.6	23.4	22.7	8.0	22.7	24.6	20.8	16.7
a_hor2	22.7	22.7	20.8	8.6	22.7	20.8	22.7	8.6	22.7	20.8	20.8	8.8
a_hor3	22.7	20.8	22.7	8.6	22.7	22.7	22.7	0.0	22.7	22.7	20.8	8.6
a_d8_w	-	-	-	-	-	-	-	-	-	-	-	-
a_d9_w	-	-	-	-	-	-	-	-	-	-	-	-
a_d10_w	-	-	-	-	-	-	-	-	-	-	-	-
a_e1_w	9.4	8.7	7.6	22.0	8.7	7.6	9.4	22.0	7.9	5.7	5.7	34.3
a_e2_w	8.7	8.7	9.9	13.2	6.1	5.7	6.1	7.5	6.1	7.2	6.1	17.3
a_e3_t	-	-	-	-	-	-	-	-	-	-	-	-
a_e5_t	-	-	-	-	-	-	-	-	-	-	-	-
a_c1_w	-	-	-	-	-	-	-	-	-	-	-	-
a_c2_w	-	-	-	-	-	-	-	-	-	-	-	-

Table 2.6 Repeatability of Crack Measurements at Different Speeds (US 441)

Crack Feature ID	Variation From Mean(%)					
	25 mph		35 mph		45 mph	
	Lights on	Lights off	Lights on	Lights off	Lights on	Lights off
A_f1_w	14.4	Not visible	25.6	Not visible	31.2	Not visible
A_f3_w	65.0	Not visible	60.5	Not visible	30.0	Not visible
A_f5_w	30.6	Not visible	42.9	Not visible	0.0	Not visible
A_vert1	10.3	10.7	0.0	10.7	10.7	10.3
A_vert2	10.3	0.0	0.0	21.4	0.7	11.5
A_vert3	0.0	0.0	22.2	21.4	10.7	0.0
A_hor1	0.0	8.6	0.0	8.0	8.1	16.7
A_hor2	0.0	8.6	18.2	8.6	8.8	8.8
A_hor3	8.6	8.6	8.6	0.0	8.6	8.6
A_d8_w	19.0	Not visible	17.0	Not visible	16.3	Not visible
A_d9_w	19.0	Not visible	28.7	Not visible	15.7	Not visible
A_d10_w	27.7	Not visible	123.6	Not visible	109.4	Not visible
A_e1_w	83.3	22.0	3.4	22.0	15.1	34.3
A_e2_w	33.7	13.2	43.4	7.5	23.7	17.3
A_e3_t	5.0	Not visible	3.4	Not visible	9.2	Not visible
A_e5_t	17.8	Not visible	1.7	Not visible	8.5	Not visible
A_c1_w	22.0	Not visible	35.4	Not visible	12.8	Not visible
A_c2_w	23.1	Not visible	23.1	Not visible	37.5	Not visible

Table 2.7 Repeatability (Precision) of Crack Evaluation

Road ID	Average Percent Variation from Mean					
	US 441 (asphalt) Partly Sunny		SR 331 (asphalt) Cloudy		SR 28 (concrete) Sunny	
Light. System / Feature Size	On	Off	On	Off	On	Off
(< 3 mm)	24.5	*NA	55.1	33.3	49.3	58.8
(3 – 6 mm)	55.5	*NA	35.1	33.0	30.2	35.6
(> 6 mm)	15.0	11.6	20.6	11.7	8.8	8.6

*No data were available for these categories

2.3.3 Accuracy of Crack Measurements

Next, the accuracy of crack evaluation based on images under different lighting conditions and speeds was evaluated. The difference between the crack dimensions obtained from manual survey and the images, Δ_{dist} (error in the evaluation) is computed as:

$$\Delta_{dist}[\%] = \left[\frac{\left(d_{crack} - d'_{crack} \right)}{d_{crack}} \right] 100 \qquad (2.2)$$

where d_{crack} = crack dimensions obtained from the manual survey

d'_{crack} = crack dimensions computed from the pavement images

Results of the above evaluation, shown in Figure 2.5 for US 441 and in [Mraz, 2004] for the other pavements (SR 331 and SR 26) indicate that the evaluation of crack dimensions (width and length) is not sensitive to vehicle speed. Tables 2.8 illustrates the comparison of crack features on US 441 (with and without illumination) evaluated from images captured at different speeds with the corresponding manual measurements. In asphalt pavements, there were a number of situations where recognition of cracks was not possible in the absence of the lighting system. These cases are denoted in Table 2.8 as “n/a”.

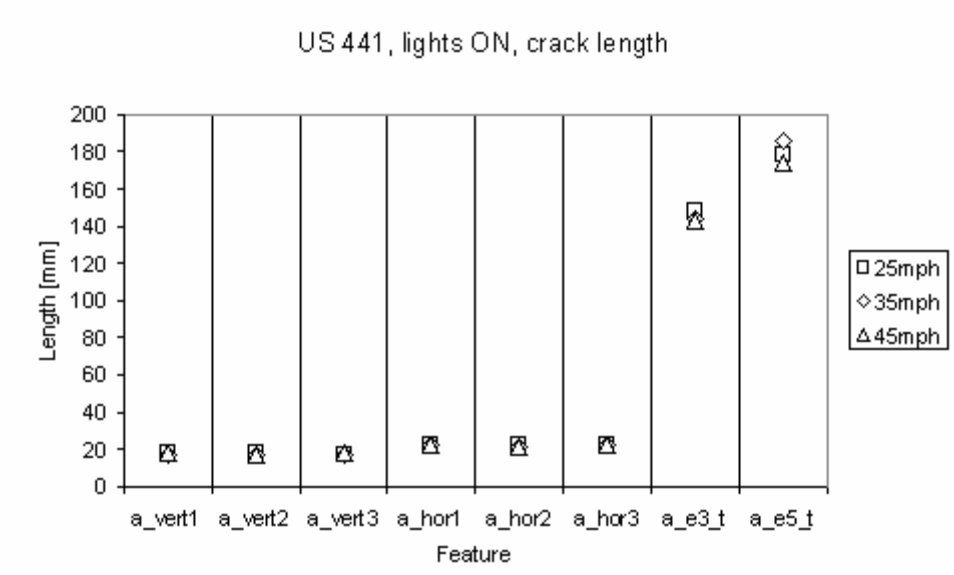

Figure 2.5 Lengths of the Crack Features Measured from Images

For concrete pavements (SR 28) on the other hand, the recognition ability was not a significant issue (Mraz, 2004). In general, the errors resulting from crack evaluation with the lighting system was seen to be larger than that without it. Similar results for pavement sections on SR 331 and SR 28 are presented in (Mraz, 2004). A summary of results on crack evaluation accuracy is provided in Table 2.9 where evaluation errors are determined with respect to the manual estimates of crack dimensions. Based on the error estimates from all surveyed pavement sections, it is seen that as the feature size decreases, the error of evaluation generally increases. This is to be expected since, in an image, one pixel represents a pavement area as large as 2 mm x 2 mm. Therefore, if a hairline crack is only 3 mm wide and it is visually approximated as consisting of two full pixels, its width is evaluated as 4 mm resulting in an error of 50%.

Table 2.8 Dimensions of Crack Features and Corresponding Errors (Δ) (US 441)

Crack Feature ID	Manual Distress Measurement [mm]	Percent Error (Δ) [%] in Distress Measurement from Images					
		25 mph		35 mph		45 mph	
		Lights on	Lights off	Lights on	Lights off	Lights on	Lights off
a_f1_w	16.5	4.9	n/a	20.7	n/a	13.6	n/a
a_f3_w	4.0	45.4	n/a	42.7	n/a	57.5	n/a
a_f5_w	2.5	103.2	n/a	76.4	n/a	24.4	n/a
a_vert1	20.0	8.7	11.8	15.0	11.8	11.8	8.7
a_vert2	20.0	8.7	15.0	15.0	11.8	14.8	18.1
a_vert3	20.0	15.0	5.5	15.0	11.8	11.8	5.5
a_hor1	20.0	13.4	10.2	13.4	17.8	10.4	13.4
a_hor2	20.0	13.4	10.2	3.9	10.2	7.1	7.1
a_hor3	20.0	10.2	10.2	10.2	13.4	10.2	10.2
a_d8_w	9.0	14.2	n/a	7.2	n/a	23.8	n/a
a_d9_w	18.5	2.4	n/a	0.7	n/a	9.4	n/a
a_d10_w	4.0	39.9	n/a	17.5	n/a	9.8	n/a
a_e1_w	12.0	5.5	28.6	12.8	28.6	5.3	46.7
a_e2_w	15.0	3.5	39.3	3.0	60.2	24.8	56.7
a_e3_t	157.0	5.3	n/a	8.5	n/a	8.9	n/a
a_e5_t	168.0	5.9	n/a	10.6	n/a	3.8	n/a
a_c1_w	16.0	10.4	n/a	7.4	n/a	8.6	n/a
a_c2_w	6.0	36.5	n/a	36.5	n/a	16.0	n/a

Table 2.9 Accuracy of Crack Evaluation

Road ID	Average Percent Error in Imaged Crack Length					
	US 441 (asphalt) – partly sunny		SR 331 (asphalt) - cloudy		SR 28 (concrete) - sunny	
Lighting System / Feature Size	On	Off	On	Off	On	Off
(< 3 mm)	51.7	n/a	64.2	69.8	244.4	325.4
(3 – 6 mm)	25.5	n/a	27.8	56.7	48.3	64.0
(> 6 mm)	8.7	19.3	15.0	25.2	9.4	11.2

2.4 Relationship between the accuracy of crack evaluation and SNR of images

In the next stage of the investigation, the images were evaluated to explore the possible correlation between the SNR values and the error associated with the evaluation of crack widths and lengths. A sample of these results is indicated in Figures 2.6. The data required to perform this comparison were extracted from repeated measurements of the same crack features that resulted in significantly different SNR values (Figs 2.2 and 2.3) and the error assessments (Table 2.8). Only the plots where the difference between the maximum and minimum SNR values of more than 1 dB were used to generate Figure 2.6. Figure 2.6 shows that the higher the SNR the lower the error associated with the measured crack features. Although the available range of SNR was too small to reach a definitive conclusion, a tendency is observed where prior evaluation of SNR using grayscale targets could provide a basis for pre-determining the accuracy of crack evaluation. Therefore, it is recommended that FDOT personnel pursue this investigation by building a broader database of error in crack evaluation and the corresponding SNR values using the grayscale target in their routine crack evaluations. This exercise can be implemented easily by first imaging the grayscale target under the same conditions in which crack evaluation is to be performed and then deriving the relevant SNR from the images of the grayscale target.

2.5 Evaluation of the geometrical distortion of images

In order to capture distress images on lane widths up to 14 ft, FDOT's MPSV uses a line-scan digital camera equipped with fisheye optics with a 15 mm focal length. Use of such a short focal length optics introduces significant optical distortion only in the transverse direction, reaching up to 25% in the outermost areas of a lane. On the other hand, the line-scan camera creates the full pavement image by stitching together individual 2 mm wide image lines. Hence any error in the distance measurement instrument (DMI) can cause an additional longitudinal distortion. Therefore, one has to incorporate the relevant corrections for both longitudinal and transverse distortions to achieve accurate pavement distress evaluation.

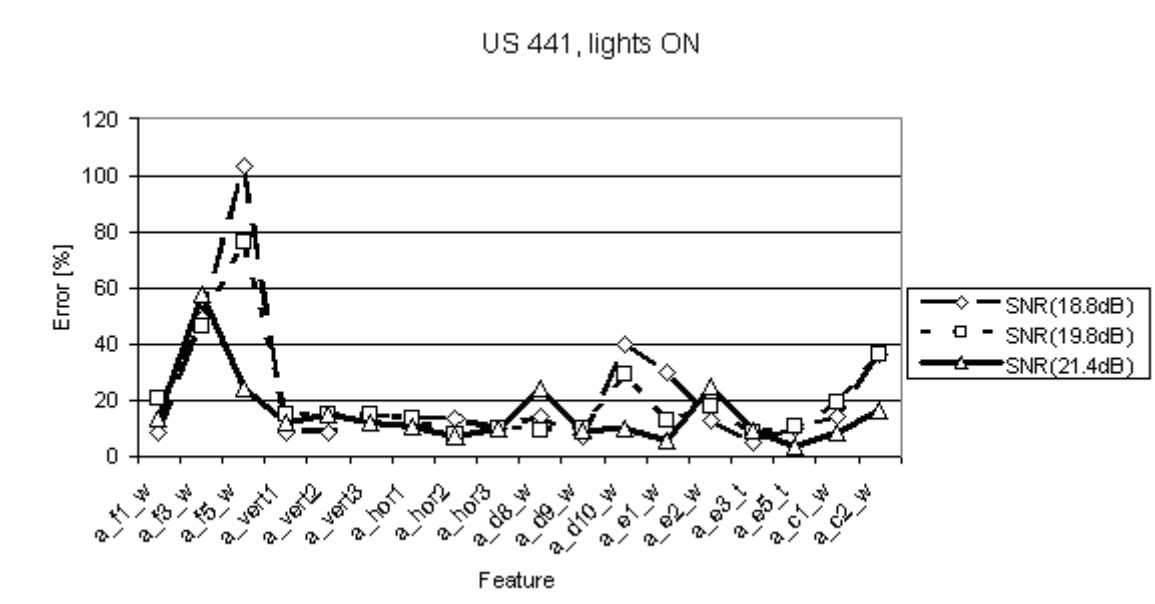

Figure 2.6 Correlation Between Variability in Crack Measurements and SNR for US 441

To estimate the geometrical distortion of a pavement image and derive an appropriate correction, the testing grid shown in Figure 2.7 was used. It consists of a number of white tacks placed on the pavement at predefined intervals measured to an accuracy of ± 0.5 mm. After creating the testing grid, FDOT MPSV was driven over it ten (10) times and the distances between the tacks were computed from the images captured in each trial. Based on the above comparison of manually measured distances and those evaluated from the images, suitable correction factors were determined. Table 2.10 shows an example of the optical distortion error with the corresponding correction factors for rows R2, R3, and R4 of testing grid. Figure 2.8 presents a plot of the derived optical distortion correction based on the lateral position of the measured feature on the pavement image. For Basler L-103 line-scan camera with Sigma fisheye optics of 15 mm focal length, the correction in the transverse direction is defined mathematically as:

$$y = 2 \cdot 10^{-13} x^4 - 9 \cdot 10^{-10} x^3 + 2 \cdot 10^{-6} x^2 - 0.0018x + 1.6591 \quad (2.3)$$

where x and y represent the position on the pavement image (in pixels) and the correction factor, respectively.

Similarly, the DMI-based error in the longitudinal distance was found to be 2.4 % which corresponds to a correction factor of 1.024. Thus, whenever one evaluates images of cracks, one has to determine and apply the above correction factor to the longitudinal distances measured in images.

Based on the combined corrections, the images captured on US 441, SR 331, and SR 28 were post-processed and the re-evaluated results are summarized in the last three columns of Table 2.11. From Table 2.11, it can be seen that based on the distortion correction, the average improvement in measurement of crack dimensions from images ranges from 53-65% for both asphalt and concrete pavements. As seen in Fig. 2.8, the optical distortion error is systematic depending on the location of the crack features with respect to the centerline of the lane, i,e. the farther they are from the camera axis, the larger the error is. Hence the investigators recommend that FDOT makes it a routine practice to incorporate this correction in crack evaluation based on images.

Table 2.10 Line-scan Image Optical Distortion Error in FDOT MPSV

Row	Patch Number	Error (%)	Kcor
R2	1 – 2	14.2	1.17
	2 – 3	8.1	1.09
	3 – 4	2.6	1.03
	4 – 5	1.9	0.98
	5 – 6	1.1	0.99
	6 – 7	3.1	1.03
	7 – 8	7.7	1.08
	8 – 9	14.7	1.17
R3	1 – 2	19.4	1.24
	2 – 3	12.8	1.15
	3 – 4	7.5	1.08
	4 – 5	2.0	1.02
	5 – 6	1.2	0.99
	6 – 7	1.1	0.99
	7 – 8	3.6	0.96
	8 – 9	0.5	1.00
	9 – 10	3.3	1.03
	10 – 11	7.7	1.08
	11 – 12	13.1	1.15
	12 – 13	19.7	1.24
R4	1 – 2	20.8	1.26
	2 – 3	13.5	1.16
	3 – 4	8.4	1.09
	4 – 5	3.9	1.04
	5 – 6	0.6	0.99
	6 – 7	0.7	0.99
	7 – 8	2.2	0.98
	8 – 9	0.1	1.00
	9 – 10	4.2	1.04
	10 – 11	8.8	1.10
	11 – 12	15.7	1.19

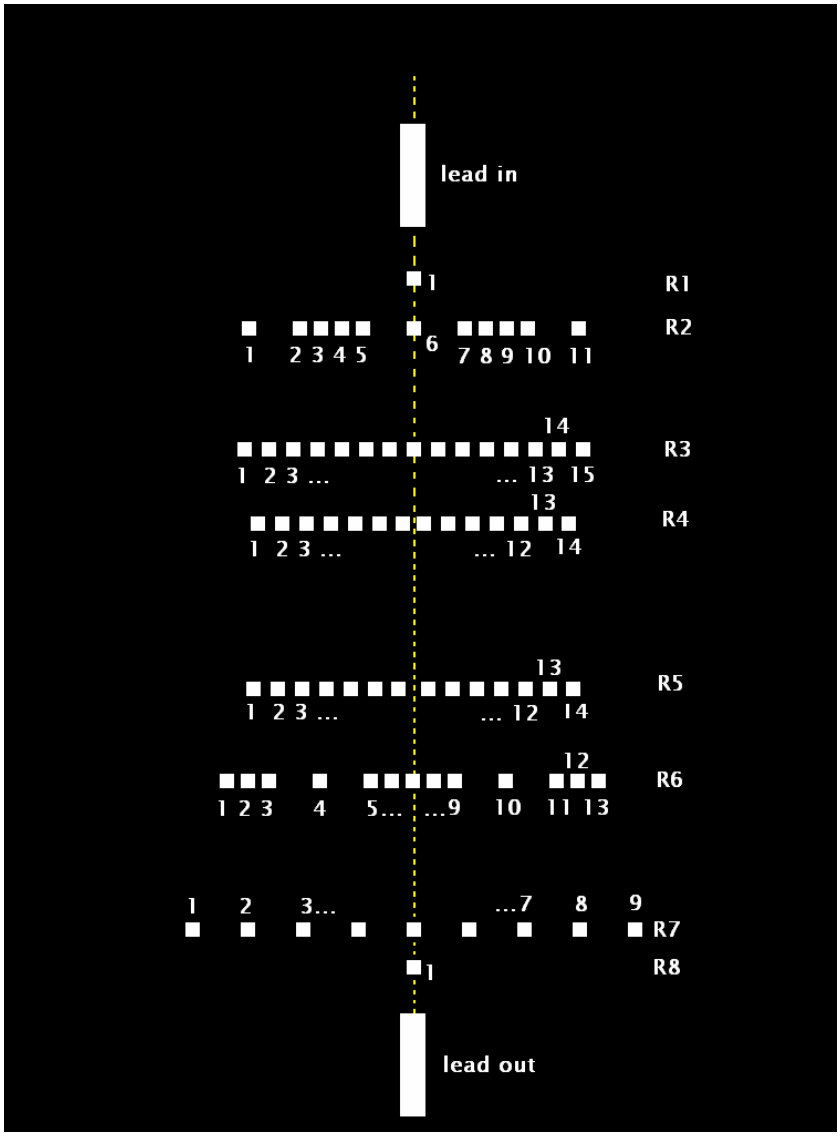

Figure 2.7 Grid Area Used for Optical Distortion Testing

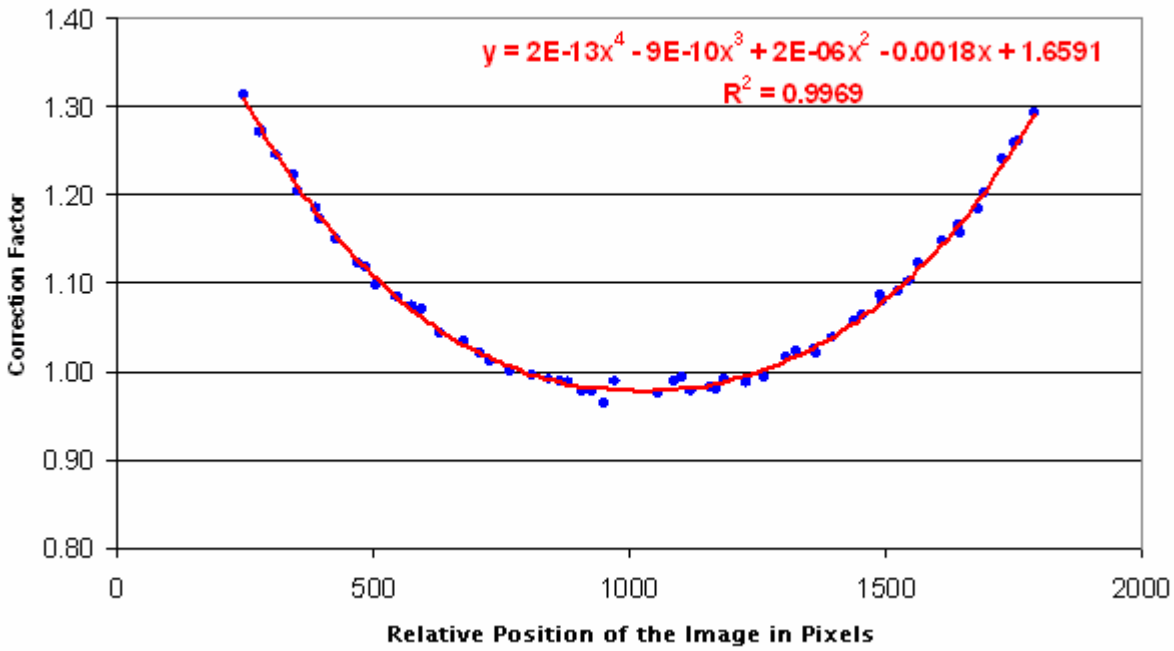

Figure 2.8 Correction for Optical Distortion in the Pavement Camera of FDOT MPSV

Table 2.11 Improvement of Crack Evaluation due to Distortion Correction

Road ID	Surface Type	Lighting Conditions	Pavement Lighting	Average Error in Distance Before Correction (mm)	Average Error in Distance After Correction (mm)	Improve-ment (%)
US 441	Asphalt	Overcast	On	3.4	1.3	60.5%
			Off	3.0	1.2	60.2%
SR 331	Asphalt	Cloudy	On	2.7	1.2	53.4%
			Off	4.1	1.4	65.1%
SR 28	Concrete	Sunny	On	1.7	0.7	54.6%
			Off	2.1	0.9	56.9%

2.6 Effect of the vehicle movement on image

Data from the Inertial Measurement Unit (IMU) in the FDOT MPSV are integrated by the Position and Orientation System (POS) computer for georeferencing and evaluation of roadway geometry. Therefore, the kinematic data relevant to a given image can be extracted from the IMU based on the specific time interval within which that image had been captured.

Velocities in the global coordinate system (Xg – Geographical West, Yg – Geographical North, and Zg – Vertically downwards) and accelerations in the body coordinate system (Xb – direction of vehicle movement, Yb – transverse direction to the right, and Zb – perpendicular to XbYb plane and downwards) were processed through the *Applanix POSPac* program. Then, the velocity of the vehicle expressed in the global coordinate system were transformed into the corresponding velocities in the body coordinate system. Finally, the incremental distances traveled by the vehicle, or the relative displacement of a given object captured by the imaging system, was computed numerically based on the corresponding body velocities (v_{body_i}) and body accelerations (a_{body_i}) as:

$$\Delta = d_{object} = \frac{v_{body_i} + v_{body_{i+1}}}{2}\left(t_{i+1} - t_i\right) = \frac{v_{body_i} + \left[v_{body_i} + \left(\frac{a_{body_i} + a_{body_{i+1}}}{2} \right)\left(t_{i+1} - t_i\right) \right]}{2}\left(t_{i+1} - t_i\right) \qquad (2.3)$$

where $\left(t_{i+1} - t_i\right)$ is the time interval corresponding to the data acquisition period of 0.05 seconds based on IMU's data collection frequency of 200 Hz.

Furthermore, the maximum and average displacements within a period of 0.05 seconds were extracted from the plots of Eqn. (2.3) presented in Mraz (2004). Subsequently, the simple lens formula was used to determine the corresponding displacement of the pavement features on the

sensor during that time interval. Finally, the displacement was computed in terms of pixel lengths, Δ_{sensor} , using the pixel pitch (p) of the Basler L103 line-scan camera as:

$$\Delta_{sensor} = \frac{d_{sensor}}{p} \tag{2.4}$$

The complete results of this evaluation are presented in Table 2.12. Based on Table 2.12, it can be seen that the maximum error occurring under any imaging condition is approximately 0.32 pixels, which is below the critical (Nyquist) frequency limit of 0.5 pixels. This occurs at highway speeds and exposure times of 1/19,000 seconds in the direction of travel only. Hence it can be concluded that even low exposure time would not become a limiting factor in image quality evaluation.

Table 2.12 Number of Pixels in Image Displacement Due to Vehicle Movement (25 mph)

Road ID	Body Coordinates	Average Distance traveled [mm] in 1/200 s	Max Distance Traveled [mm] in 1/200 s	Average Displacement of Image in Pixels in 1/19,000 s	Max Displacement of Image in Pixels in 1/19,000 s	Average Displacement of Image in Pixels in 1/40,000 s	Max Displacement of image in pixels in 1/40,000 s
US 441	X	56.0	57.0	0.320	0.310	0.150	0.150
	Y	0.7	2.5	0.014	0.004	0.007	0.002
	Z	1.0	4.5	0	0	0	0
SR 331	X	54.0	57.0	0.320	0.300	0.150	0.140
	Y	0.2	1.2	0.007	0.001	0.003	0.001
	Z	0.5	1.25	0	0	0	0

CHAPTER 3

IMPROVED ALGORITHM FOR PREDICTION OF ROAD CURVATURE AND PRELIMINARY VALIDATION OF INERTIAL MEASUREMENTS.

3.0 Introduction

Position and orientation location systems equipped with Inertial Navigation Systems (INS) coupled with Differential Global Positioning System (DGPS) have become quite popular in a variety of applications including the highway evaluation operations. The FDOT Multi-functional Survey vehicle (MPSV) is also equipped with an INS/DGPS coupled system that can measure the vehicle's spatial location and the orientation at any given instant during field operations. This system has the ability to automatically collect roadway geometric data at highway speeds.

DGPS navigation on its own can accurately identify the location of a moving vehicle using two antennas that receive signals transmitted by four satellites orbiting the earth. On the other hand, a typical INS system contains an Inertial Measurement Unit (IMU) with three gyroscopes and three linear, single-degree, accelerometers installed along the three orthogonal axes to measure, respectively, the 3-D orientation and acceleration components. It also includes a navigational computer that facilitates the navigation solution through its interaction with the DGPS unit. However, INS and DGPS integrated systems are widely used in navigation due to the advantages they offer when used as an integrated system as opposed to separate units [Scherzinger, 2000].

In the FDOT Survey vehicle, the INS/DGPS system uses state-of-the-art fiber optic gyroscopes and silicon accelerometers in its IMU. The integration of the INS and the DGPS is achieved using a statistical algorithm which minimizes the error involved in the position prediction [Scherzinger, 2000]. This algorithm and many other relevant programs are executed on the POS Computer System (POS) that controls the above system.

3.1 Scope of Investigation

The roadway geometric data typically obtained by the INS/DGPS coupled system are (1) cross-slopes, (2) grades of vertical curves (3) radii of curvature of horizontal curves, and (4) GPS data. High sensitivity of the instruments in the IMU unit and the relatively high frequency of data gathering (i.e.200 Hz) combined with even small scale variability caused by either the roadway, the operator or the instruments themselves can introduce significant errors in the INS/DGPS readings. The results of an experimental program that was executed to compare the INS/DGPS geometric data with the corresponding manual measurements is reported in this chapter.

3.2 POS Measurements

Measurements of the POS/LV system are generally provided in two different coordinate systems. The IMU is used to determine the orientation of the vehicle based on the angles of tilts about a set of coordinate axes called the body coordinates based on three orthogonal axes [POSLV, 2000, POSPac User manual, 2000]; (1) X oriented towards the front of the vehicle, (2) Y to the right of the vehicle and (3) Z towards the bottom of the vehicle. Figure 3.1 illustrates the body coordinate system used in the FDOT pavement evaluation vehicle. The above angles of tilts are also known as roll, pitch and yaw respectively [*POSPac* User manual, 2000]. In order to measure the angles of tilt, the IMU uses three fiber-optic gyroscopes setup along the three orthogonal axes defined above. First the gyroscopes measure the *rates* of angular rotation about the three axes.

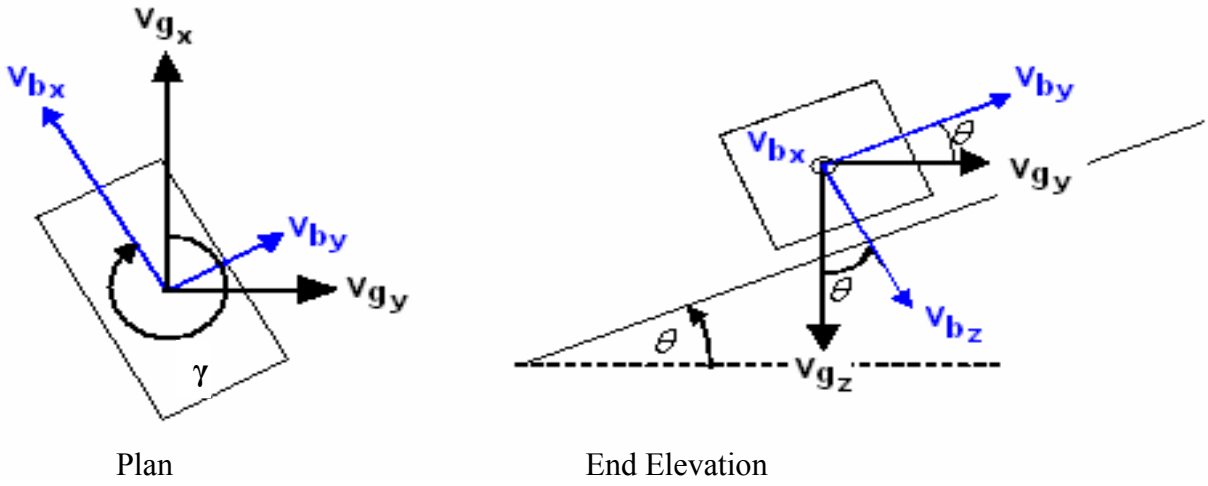

Plan End Elevation

Figure 3.1 The Local or Body Coordinate System Used in the Vehicle.

Then the corresponding angles of tilt are estimated by integrating the rates of rotation with respect to time. In addition to the gyroscopes, the IMU uses three different single degree accelerometers fixed along the same three orthogonal axes defined above, to measure the respective acceleration components. Then, the traveled distances are computed by double integrating these accelerations. However, the integration operation cannot be performed on the body coordinate system since the body coordinate system varies as the vehicle travels. Therefore, before the integration operation, the angular rotation rates and accelerations must be transformed to the global system of coordinates that is fixed in space such that the positive X axis is towards positive geographical east, the positive Y axis is towards positive geographical north and the positive Z axis is parallel to the gravity vector but in the opposite direction. Therefore, the overall transformation matrix from the body coordinate frame to the navigation or the global coordinate frame is expressed as:

$$T = \begin{bmatrix} \cos(\theta)\cos(\gamma) - \sin(\theta)\sin(\phi)\sin(\gamma) & -\sin(\gamma)\cos(\phi) & -\cos(\theta)\sin(\phi)\sin(\gamma) + \sin(\theta)\cos(\gamma) \\ \cos(\gamma)\sin(\phi)\sin(\theta) - \cos(\theta)\sin(\gamma) & \cos(\gamma)\cos(\phi) & \cos(\gamma)\sin(\phi)\cos(\theta) + \sin(\gamma)\sin(\theta) \\ \cos(\phi)\sin(\theta) & -\sin(\phi) & \cos(\theta)\cos(\phi) \end{bmatrix} \tag{3.1}$$

Where θ, ϕ and γ are roll, pitch and heading of the vehicle measured by the IMU. Then, the global coordinates can be obtained as:

$$\begin{pmatrix} x_G \\ y_G \\ z_G \end{pmatrix} = \mathbf{T} \begin{pmatrix} x_b \\ y_b \\ z_b \end{pmatrix} \tag{3.2}$$

3.2.1 Integration of IMU Data for Specification of Orientation and Position

The cumulative tilt of the vehicle about any given axis is given by

$$Angle = \int_{t_0}^{t} \Omega dt \tag{3.3}$$

Where Ω is rate of angular rotation in that direction obtained from IMU and transformed to the global coordinate system. Similarly the accelerations expressed in the global coordinate system are integrated once with respect to time in estimating the corresponding velocities (v) and twice with respect to time in estimating the displacements along the respective axes (d), as follows:

$$v = \int_{t_0}^{t} a dt \tag{3.4}$$

$$d = \int_{t_0}^{t_1} \int a dt \tag{3.5}$$

Therefore, the IMU measurements can be used to describe the complete orientation and the location of the vehicle with respect to the global coordinate system.

Verification of orientation data:

The second, third and fourth columns of Table 3.1 shows the initial orientations, global velocities and body accelerations for a brief test run that lasted 0.05 seconds and incorporated 10 IMU readings at a frequency of 200 Hz (t =10/200 = 0.05 s). Global accelerations are computed from the body accelerations using:

$$[\mathbf{a_g}]_1 = [\mathbf{T}][\mathbf{a_b}]_1 \tag{3.6}$$

Where T is given by Eqn (3.1) and a_g and a_b are global and body accelerations, respectively. The a_g values are indicated in the fifth column of Table 3.1. Using ten computational steps with each step corresponding to one IMU data point, the global velocities are computed from Eqn (3.4) and compared with the corresponding measured values in the eighth and ninth columns of Table 3.1. Similarly the distances traveled along the moving direction was calculated using Eqn (3.5) and compared with the corresponding distance obtained from the vehicle's Distant Measuring Instrument (DMI). These results are shown in the tenth and the eleventh columns of the Table 3.1.

Table 3.1 Verification of the Integrated IMU Readings After 10 Steps (t=0.05 s)

Axis	Initial conditions (t=0)			After ten time steps (t= 0.05s)						
	Angle (rad)	Global vel. (m/s)	Body accel (m/s^{-2})	a_g (ms^{-2})	Angle (rad). Eq.3.3	Measured angle (rad.)	Global velocities(m/s)		Distances (m)	
							Eqn. 3.4	Meas.	Eqn. 3.5	Meas. (DMI)
(1)	**(2)**	**(3)**	**(4)**	**(5)**	**(6)**	**(7)**	**(8)**	**(9)**	**(10)**	**(11)**
x	0.0320	0.0554	0.2365	0.0527	0.0325	0.0324	0.0566	0.05586	0.4672	0.5000
y	-0.0005	-9.3467	0.1260	0.2393	-0.0002	-0.0002	-9.3486	-9.3508		
z	4.7205	0.0960	0.9700	0.0750	4.7204	4.7204	0.1333	0.06424		

Table 3.1 shows reasonably close agreement between the distances computed using IMU data (Eqn. 3.5) and those obtained from the DMI, within the brief test run. Finally, the sixth and seventh columns of Table 3.1 illustrate the rotations obtained from Eqn (3.3) and the corresponding values obtained from the IMU unit after 10 computational steps.

3.3 Evaluation of cross-slope

The function of the cross-slope provided in a roadway is to accelerate the drainage of rain water and reduce the hydroplaning potential. The typical cross-slope requirement of a roadway is 2% in order to avoid *ponding* of water and facilitate runoff from the roadway. In addition, roads are sloped in the lateral direction to control the lateral wandering of vehicles traveling on a bend by meeting the centripetal force requirement of the vehicle. This construction feature is commonly known as the super-elevation at the curve and is

different from the roadway cross-slope in that the former is only provided in the direction of the curve, in all of the lanes. For a curve, the super elevation has to be estimated based on the speed limit of the roadway, the radius of curvature, and friction characteristics [Glennon et al, 2003].

$$e + f = \frac{v^2}{127R} \tag{3.7}$$

Where e is the super-elevation of the roadway in m/m, f is the side friction factor, v is the travel velocity in km/h and R is the radius of curvature of the curve in m.

When measuring the cross-slope, the standard procedure is to measure the height at two different locations across the lane, typically at the edge of pavement and the roadway crown. From the ratio of this height difference and the lane width, one would obtain the cross-slope of the lane (Figure 3.2) as:

$$\text{Cross - slope} = \frac{\Delta \text{H}}{\text{L}} = \frac{(y_2 - y_1)}{\text{L}} \tag{3.8}$$

In the FDOT pavement evaluation vehicle, the subsystems used to measure the cross-slopes include four laser sensors that are attached to the front bumper and the Inertial Measurement Unit (IMU). The four laser sensors provide distances from the front bumper of the vehicle to the roadway surface. Of the four bumper lasers, one is at the right corner of the bumper while the others are located at distances of $33.25^{//}$, $54.25^{//}$ and $68^{//}$ respectively from the right corner of the bumper. The best-fit straight line of the heights measured by the laser sensors provides the slope of the road with respect to the vehicle bumper. In addition, the tilt of the vehicle body and the bumper in the lateral direction can be obtained by the IMU, which is firmly fixed to the floorboard of the van. Then by considering the difference between the above two readings, (1) the tilt of the vehicle floor or the vehicle bumper and (2) the slope of the road visualized by the lasers or the vehicle bumper, one can approximately determine the cross-slope of the roadway. Figure 3.2 illustrates the above measurements.

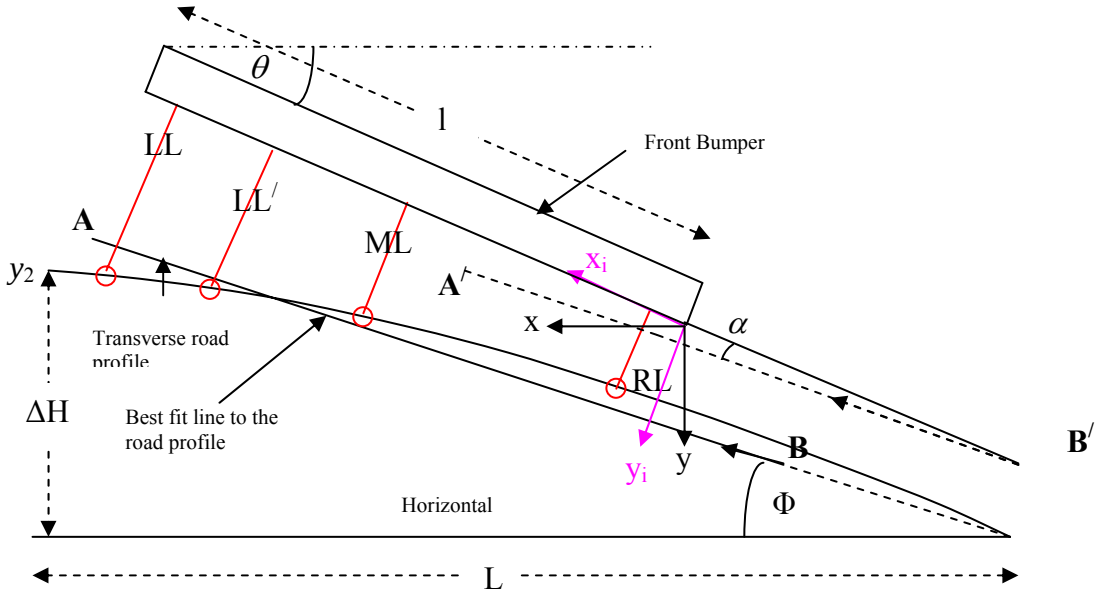

Figure 3.2 Relationship among the Road Cross-slope, Laser Slope and the Roll Measured by the IMU.

Where,

AB- Best fit line for the laser sensor readings.

$A^{/}B^{/}$- Parallel line to AB drawn at $B^{/}$.

α - Slope measured by the laser sensors with respect to AB.

Φ- Slope of the best fit line AB.

θ- Roll angle measured by the IMU.

RL- Laser sensor located at the right corner of the bumper.

ML- Laser sensor located in the middle of the bumper.

LL- Laser sensor located at the left corner of the bumper.

$LL^{/}$- Laser sensor located in between LL and ML.

l: Width of the vehicle bumper (in inches).

L: Width of the lane (in feet).

(x_i,y_i): Coordinates with respect to the bumper plane.

(x, y): Horizontal and Vertical coordinate pair.

y_2, y_1: measured heights at the crown and the shoulder of the lane respectively, expressed in horizontal-vertical (x,y) coordinate system.

From Fig. 3.2, the cross-slope of the roadway estimated by the best-fit line for the road profile, AB, is given by:

$$\Phi = \theta - \alpha \,. \tag{3.9}$$

An alternative method was also explored in this study in determining the cross-slope of the roadway from the available test data. Basis for the second method in estimating cross-slope was the Least Squares Approximation (LSA) of the laser sensor readings using a parabolic fit. All of the laser measurements obtained from the vehicle are specified with respect to the coordinate system originating from the right corner of the vehicle bumper (Fig 3.2). Therefore, Eqn. (3.11) is used to convert the laser coordinates from vehicle bumper frame to the vertical and horizontal (x,y) coordinate system shown in Figure 3.2.

Transformation matrix for the coordinate transformation can be expressed as:

$$\mathbf{t} = \begin{pmatrix} \cos(\theta) & \sin(\theta) \\ -\sin(\theta) & \cos(\theta) \end{pmatrix} \tag{3.10}$$

And the (x, y) coordinates are obtained as:

$$\begin{pmatrix} x \\ y \end{pmatrix} = \mathbf{t} \begin{pmatrix} x_i \\ y_i \end{pmatrix} \tag{3.11}$$

Linear LSA fit based on the existing ICC algorithm;

The equation of LSA linear fit can be given as:

$$y = a_m x + b_m \tag{3.12}$$

Least Squares Parabolic fit (The modified algorithm);

A more accurate estimate of the transverse road profile can be obtained by using a second order (parabolic) fit expressed as:

$$y = a_m x^2 + b_m x + c_m \tag{3.13}$$

Once the least squares linear or the parabolic fit is obtained, the two curves are extended to the total width of the road to determine the road cross-slope as measured by the evaluation vehicle. To achieve this it is required to make the assumption that the vehicle travels in the middle of the lane. After the height difference is estimated using Eqn (3.13), one can obtain the cross-slope from Eqn (3.8).

3.3.1 Preliminary Experimental Verification of Highway Geometric Data:

Two experimental data sets obtained by the FDOT highway evaluation vehicle on two separate sections were used to verify the algorithms used in the INS/DGPS system. The first data set was obtained from a test run on Interstate-10 in Florida, where cross-slope data measured by a manual survey were also available. The second data set obtained on a reverse curve along the NE 8th Avenue in Gainesville, Florida contained all of the raw roadway geometric data acquired using a PC card. Figure 3.3 illustrates the parabolic fit obtained at one location within the I-10 test section. Tables 3.2 and 3.3 compare the results obtained from I-10 on two consecutive runs using the three different methods, (1) slope obtained from the manufacturer's (ICC) software (2) slope obtained by the manual survey, (3) slope obtained by LSA fits, both linear (ICC) and parabolic.

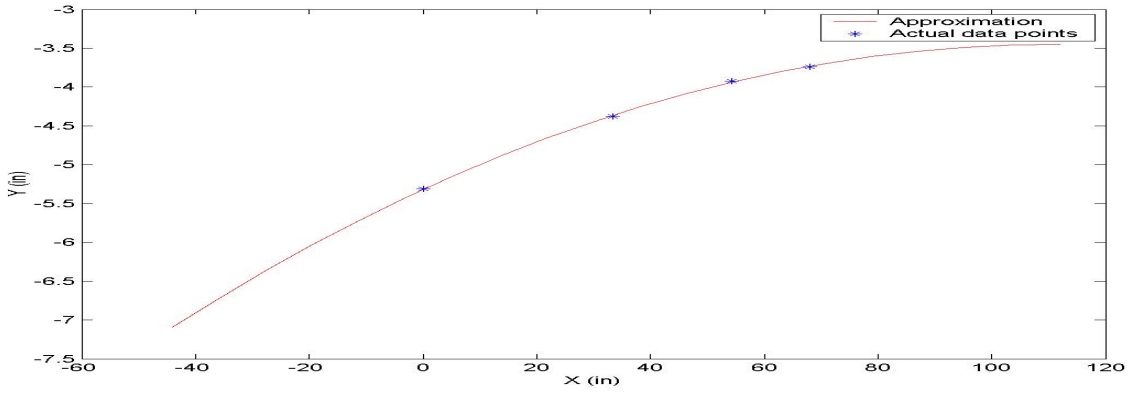

Figure 3.3 Parabolic Fit at a Point Along the Test Section, 50 ft From the Starting Point of the Test Section.

Table 3.2 Comparison of Cross-slopes for First Run on I-10

Distance from start (ft.)	(1) ICC slope (%)	(2) Survey slope (%)	(3) LSA Fit		Error (%)			Correlation coefficient	
			Linear slope (%)	Parabolic slope (%)	ICC	Linear fit	Parabolic fit	Linear fit	Parabolic fit
50	1.123	2.46	2.300	2.273	54.35	6.50	7.60	0.9805	≈1
200	0.676	1.44	2.010	1.996	53.06	39.60	38.61	0.9914	0.9969
800	-0.996	-1.84	-1.774	-1.792	45.87	3.57	2.61	0.9891	0.9985

Table 3.3 Comparison of Cross-slopes for Second Run on I-10

Distance from start (ft.)	(1) ICC slope (%)	(2) Survey slope (%)	(3) LSA Fit		Error (%)			Correlation coefficient	
			Linear slope (%)	Parabolic slope (%)	ICC	Linear fit	Parabolic Fit	Linear fit	Parabolic fit
50	1.248	2.46	2.362	2.337	49.27	3.98	5.00	0.9847	0.9997
200	0.450	1.44	1.049	1.034	68.75	27.15	28.19	0.9641	0.9884
800	-1.006	-1.84	-1.531	-1.550	45.33	16.80	15.76	0.9859	0.9999

The results in Tables 3.2 and 3.3 indicate that the LSA parabolic fit approximates the roadway cross-slopes much more accurately than any other method. Also, comparison of the results in Tables 3.2 and 3.3 shows reasonable repeatability except at the location of 200 ft from the start. The significant differences observed between the surveyed cross-slope values and all of the fitting methods at one location at a distance of 200 ft from the starting point (Tables 3.2 and 3.3) can perhaps be attributed to the inaccurate identification of the manually surveyed location. This hypothesis is further supported by the unsatisfactory accuracies of IMU measurements observed at this location as seen in Tables 3.2 and 3.3.

3.4 Radius of curvature

The proper design of the radius of curvature of a roadway at a horizontal curve is vital to making the roadway safe for its users at the design speed. Therefore, an important task of pavement infrastructure evaluations is the verification of radius of curvature to be within the acceptable limits at all horizontal curves of a roadway. This especially applies to rural roads and minor arterials that have been constructed without adhering to appropriate standards. In addition, due to the relationship between the super-elevation and the radius of curvature (Eqn 3.7), knowledge of the radius of curvature at a location is essential in checking the adequacy of super-elevation of that location. This becomes a critical issue when pavement evaluators are called upon to perform safety inspections of specific locations that are known to present safety hazards. Automated and rapid curvature information provided by the IMU system would be immensely helpful in such situations especially from the survey crew's safety perspective as well as cost effectiveness.

Roadways are designed in such a way that when a vehicle moves from a straight section of a road onto a curved section, the vehicle would experience a relatively smooth transition in curvature. This is achieved by designing transition curves at the extremes of the actual curve. Typically, this transition can be provided by two spiral curves: (1) a lead-in, which is the roadway section that starts asymptotic to the straight line segment and merges with the circular curve, and (2) a lead-out, the roadway section which diverges from the circular curve and merges with the second linear segment (Fig 3.4). In order to achieve this transition curve, designers use a gradually varying radius of curvature from a straight run to the design circular curvature of the horizontal curve. Also the lead-in and lead-out play a major role in adjusting the super-elevation from the regular cross slope on a straight roadway to the maximum super-elevation at the curve on a gradient basis. This is also known as the super-elevation runoff.

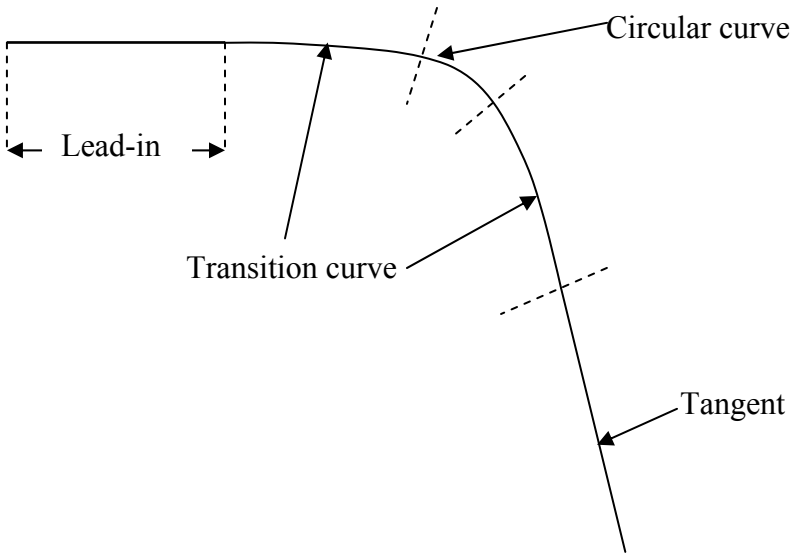

Figure 3.4 Geometry of the First Segment of a Reverse Curve Section.

Generally, two methods can be employed to determine the radius of curvature of a horizontal curve using the IMU readings. They are,

1. The kinematic method which uses the velocity in the longitudinal direction and the centripetal acceleration.
2. The geometric method where a plot of the actual vehicular horizontal trajectory is made using the velocity vector and then the radius is determined.

3.4.1 Determination of Curvature Using Kinematics

The radius of the curvature of the circular section of the horizontal curve can be determined using the following equation of circular motion:

$$r = \frac{v^2}{a} \tag{3.14}$$

Where v is the velocity of the vehicle in the longitudinal (body X) direction and a is the centripetal acceleration of the vehicle on a horizontal plane. Since both v and a are obtained by the IMU, the algorithm used in the FDOT pavement evaluation vehicle uses Eqn (3.14) to determine the instantaneous radius of the horizontal curve.

Some horizontal curves are not completely circular due to the inclusion of spiral shaped transition curves at the extremities (lead-in and lead-out) which ensure a gradual change of curvature from a straight run to the circular curve. Therefore, the generalized kinematic theory must be used in determining the instantaneous radius at any point. On a non-circular curve, the following relationships must be applied to relate the kinematic variables of vehicular motion and geometric parameters of the roadway [Beer et al, 1977].

Velocities:

$$v_r = \dot{r} \tag{3.15-a}$$

$$v_\theta = r\dot{\gamma} \tag{3.15-b}$$

Accelerations:

$$a_r = \ddot{r} - r\dot{\gamma}^2 \tag{3.16-a}$$

$$a_\theta = r\ddot{\gamma} + 2\dot{r}\dot{\gamma} \tag{3.16-b}$$

Where r and γ are respectively the radial and angular coordinates of the vehicle in a horizontal plane. Within the circular curve since r is a constant; $\dot{r} = \ddot{r} = 0$. Then it can be shown that the expression for the radius of curvature (r) reduces to Eqn (3.14).

3.4.2 Determination of Curvature Using Geometry

The velocity vector obtained from the IMU can be used to plot the trajectory of the vehicle. Because of the high frequency of the data collection (200 Hz), the error associated with the linear approximation tends to be relatively low with respect to the distance traveled. The basis for estimating the longitudinal displacement of the vehicle between two consecutive data points i and $(i+1)$ using the average velocities at those two points is illustrated in Eqn (3.17). Because the horizontal curve is two dimensional, only the horizontal velocities must be considered.

$$ds = \frac{1}{2}(v_i + v_{i+1})dt \tag{3.17}$$

Where *ds* is the longitudinal displacement that occurs when the vehicle travels between the points *i* and *(i+1)*, v_i and $v_{(i+1)}$ are the respective velocities at points *i* and *(i+1)* and the *dt* represents the time elapsed during the travel between points *i* and (*i+1*).

If the vehicle trajectory on the x-y plane is described by the function *y=f(x)*, the radius of curvature can be evaluated by the following equation;

$$R = \frac{\left(1+\left(\frac{dy_i}{dx_i}\right)^2\right)^{3/2}}{\left(\frac{d^2y_i}{dx_i^2}\right)} \tag{3.18}$$

Since x and y coordinates are found in terms of time as discrete quantities, the second order Forward Difference formulae can be used to evaluate Eqn (3.18) numerically.

$$x^{/} = \frac{(-x_{(i+2)} + 4x_{(i+1)} - 3x_i)}{2h} \tag{3.19}$$

$$x^{//} = \frac{\left[-x_{(i+3)} + 4x_{(i+2)} - 5x_{(i+1)} + 2x_i\right]}{h^2} \tag{3.20}$$

Where, $h = t_{(i+1)} - t_i$ and *i* is the index that represents any ith data points. Similarly expressions can be written for $y^{/}$ and $y^{//}$ as well.

Then the numerical forms of the derivatives needed for Eqn (3.18) can be expressed as:

$$\frac{dy_i}{dx_i} = \frac{y^{/}}{x^{/}} \tag{3.21}$$

$$\frac{d^2y_i}{dx_i^2} = \frac{[y^{//}x^{/} - x^{//}y^{/}]}{[x^{/}]^2} \tag{3.22}$$

3.4.3 Estimation of Curvature in the field:

Two common methods of estimating the radius of curvature of a horizontal curve used by accident investigators are given in [Ganguly, 2004]. Both of these methods yield accurate results when used on a circular section. Due to the ease of measurement and minimal labor requirement, these methods are widely used in the field. The two methods are outlined below:

3.4.3.1 Chord-Offset method:

This method uses a 100-foot tape and a carpenter's ruler to determine the radius of curvature. The 100-foot tape is placed on either end at the precise edge of the roadway so that an arc is separated from the curve. Then the carpenter's ruler is used to measure the distance between the mid-point of the 100-foot tape and the edge of the roadway perpendicularly across from the mid point of the 100-foot tape (offset). Once these two measurements are obtained, the radius of the curvature can be estimated by the following geometrical relationship (Fig. 3.5):

$$R = \frac{b^2}{8m} + \frac{m}{2} \tag{3.23}$$

where,

R is the radius of the curvature.

b is the chord length.

m is the measured middle offset.

3.4.3.2 Compass method:

This method uses the distance traveled along a segment of the circular section, or the arcual length, and the angle subtended by that segment of the curve on the center of the circle (included angle) to estimate the radius of curvature. Arc length can be measured by a measuring wheel or the vehicle DMI. A compass can be used to find the included angle, since it is equal to the deviation between the tangents to the circular segment at its extremes. Once the arc length and the included angle are available, the radius of the curvature can be estimated by (Fig. 3.5),

$$R = \frac{s}{\phi} \tag{3.24}$$

where,

R is the radius of the curvature of the horizontal curve.

s is the arc length of the considered circular segment.

ϕ is the included angle measured in radians.

3.5 Experimental verification of radius of curvature

A reverse curve on NE 8th Avenue in Gainesville, Florida, was used to test the above algorithms for determining the radius of curvature.

Application of the geometric method of determining the radius

Based on the algorithm in Eqn (3.18), Figure 3.6 (a) shows the variation of the radius of curvature as a function of the time spent on the curve by the survey vehicle.

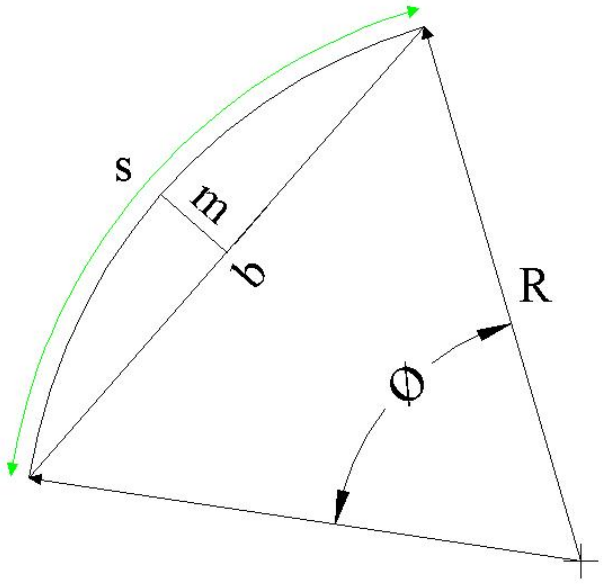

Fig. 3.5 Illustration for Chord-Offset and Compass Methods

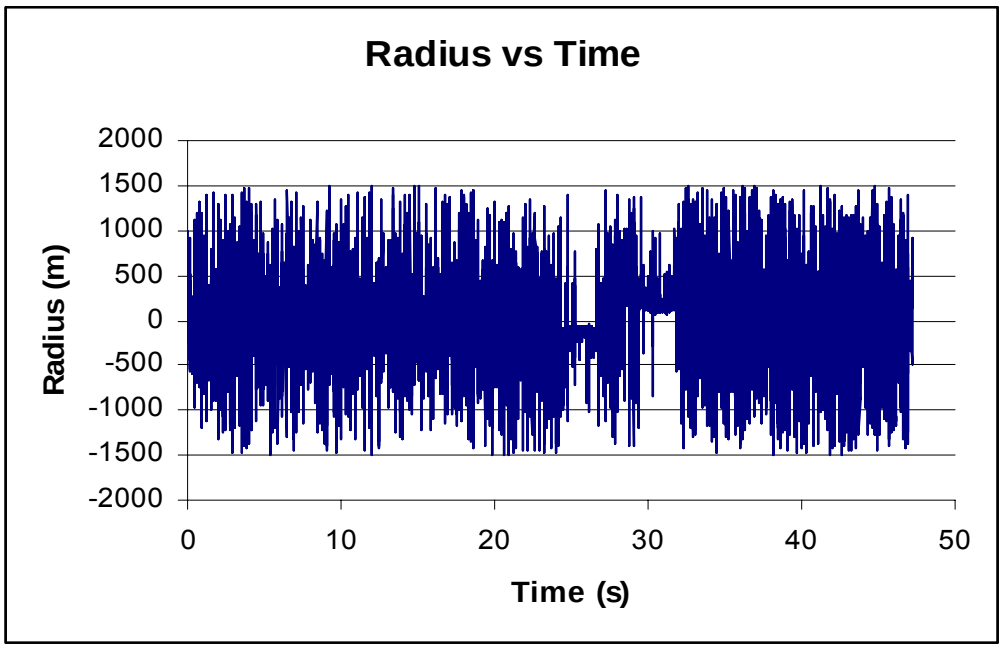

(a)

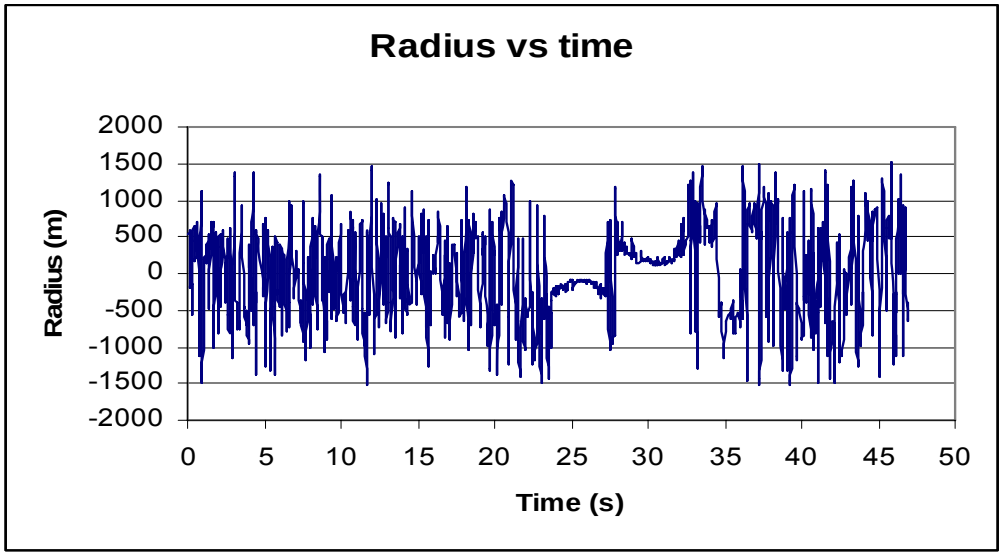

(b)

FIGURE 3.6 Radii Determined by the Geometric Method for a Data Acquisition Frequency of 200 Hz (a) Without Averaging, (b) With Averaging

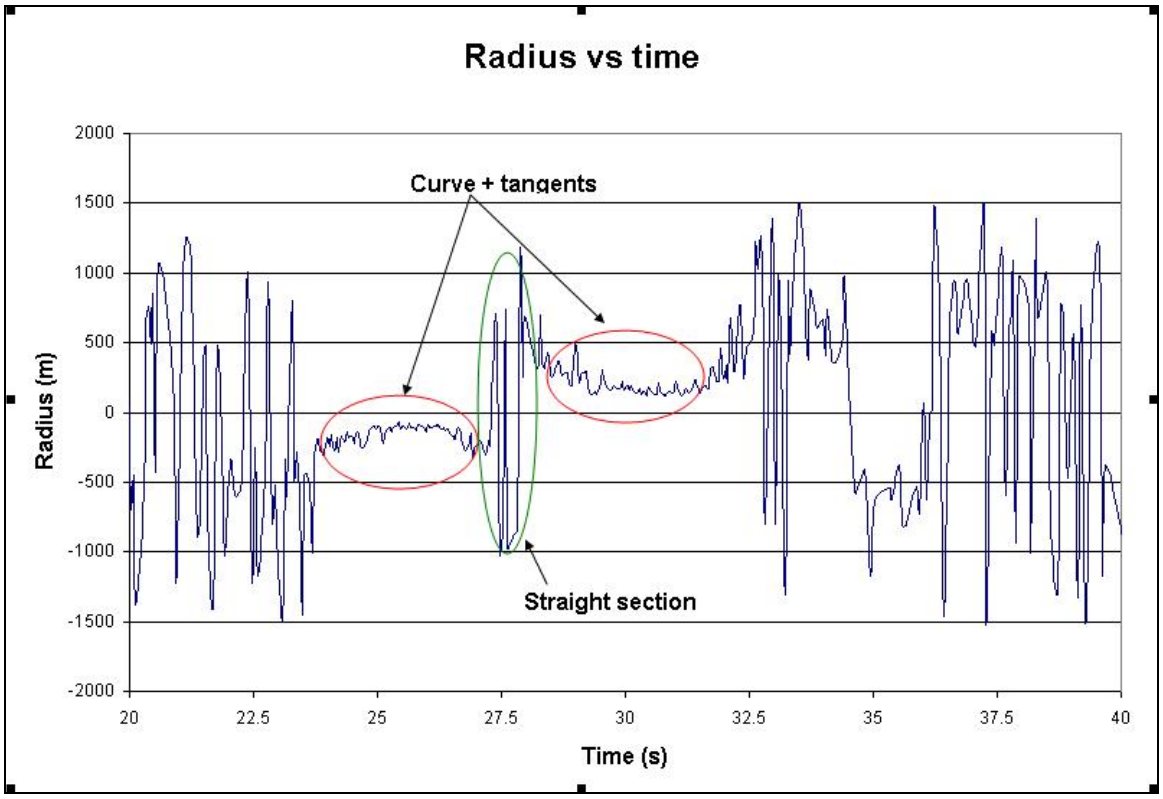

(c)

FIGURE 3.7 Radii of the Curve Determined by the Geometric Method for a Data Acquisition Frequency of 200 Hz (with averaging)

In order to address the undulations of the predicted radius values, the same data are first averaged and then plotted in Figure 3.6 (b). Averaging has been performed by considering a pre-determined number (n) of consecutive data points at one time, according to Eqn (3.25).

$$p_{avg} = \frac{(p_1 + p_2 + p_3 ..... + p_n)}{n} \tag{3.25}$$

where p denotes the variable that needs to be averaged. The average values for points (x_i,y_i) obtained from the operation of Eqn (3.25) are then used as the updated x and y coordinates for the averaged time period (i = 1…..n). The optimum interval size for data averaging in Fig 3.6(b) was found to be 10. Even though the averaging given by Eqn (3.25) smoothens the undulations, variability involved in the data and outliers still complicate the estimation of radius of curvature. To resolve this a combined moving average and moving median algorithm [Ganguly, 2004] was used in analyzing the data. The former reduces the variability while consideration of the moving median is expected to eliminate outliers. Subsequently, the second order forward difference algorithm (Eqns. 3.19–3.20) was applied to the x and y coordinates to find the first and second derivatives needed for Eqn 3.18.

Based on the trends observed in Figure 3.6(b) and its enlarged version in Fig. 3.7, the test section can be divided into three main sections. They are;(1) two tangents or straight sections at the extremities of the reverse curve, (2) two circular curves (curve segment-1 from 24 to 27 s and curve segment-2 from 28 to 32s), and (3) a short tangent section (27-28 seconds) at the point of inflexion. Ideally, the short tangent section (3) and the tangent sections (1) must indicate infinite radii values, but due to the high variability in measurements, the value of the radius of curvature oscillates rapidly in these two sections. On the other hand, the two sections where there is no significant oscillation in the value of the radius of curvature represent the two circular curves. From Fig. 3.7 it is clearly seen that, in the curved section, the variation of the radius of curvature is confined to only one side of the time axis. Comparison of Fig 3.6(a), 3.6(b) and Fig. 3.7 shows that

the uncertainty in determining the radius of curvature of the circular curve section has been certainly reduced by the averaging operation.

Figure 3.8 shows the variation of the radius with time calculated based on $v_{\theta,}$ the velocity in the longitudinal direction and $\dot{\gamma}$, the first derivative of platform heading with respect to time (Eqn (3.15-b)) numerically determined using Eqn (3.19).

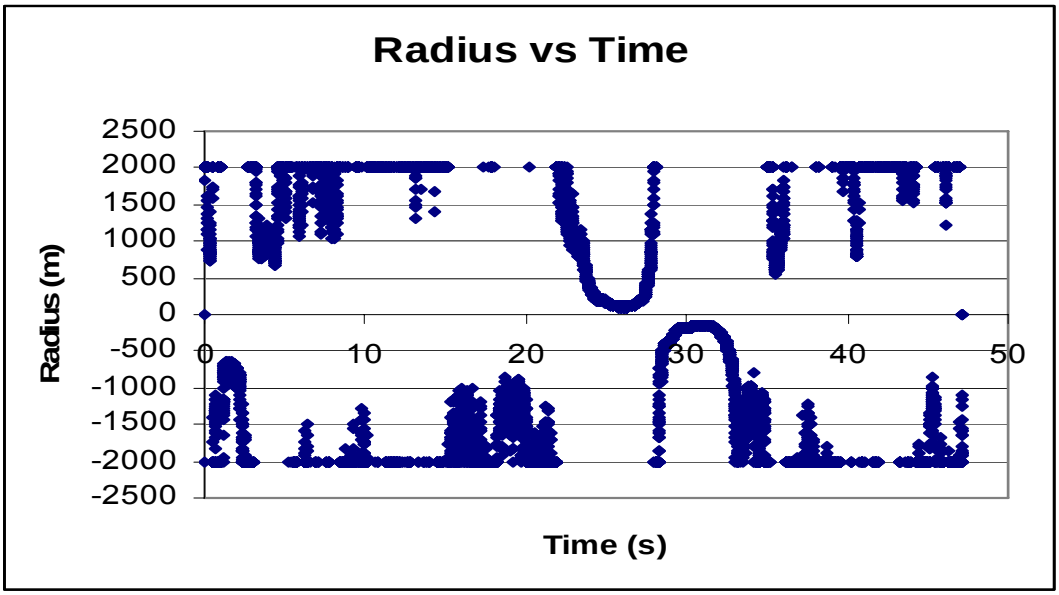

Figure 3.8 Variation of Radius With Time Evaluated From Eqn (3.14-b) (Frequency 200 Hz).

In Figure 3.8 a cut-off value of 2000 meters is imposed on the radius value to overcome the issues of undulations caused by the large values of radii of curvature on the tangent sections. When comparing Fig. 3.8 with Fig 3.6 (a) and (b), it is seen that Fig. 3.8 (based on Eqn. 3.15(b) provides the radii values with less variability. Furthermore, in Fig. 3.8, both the tangents as well as the curved sections (24s – 33 s) show relatively low oscillation and are easily distinguishable.

Application of the kinematic method of determining the radius

Fig. 3.9 shows a typical plot of predicted body acceleration in the lateral (Y) direction (a_{by}) which also exhibits significant undulations especially within both tangents and the

curves. In an alternative exercise to distinguish the tangents from the curves, upper and lower bounds, $\mu \pm 3\sigma$, were used where μ and σ are the mean and the standard deviation of the lateral acceleration data obtained from the test section.

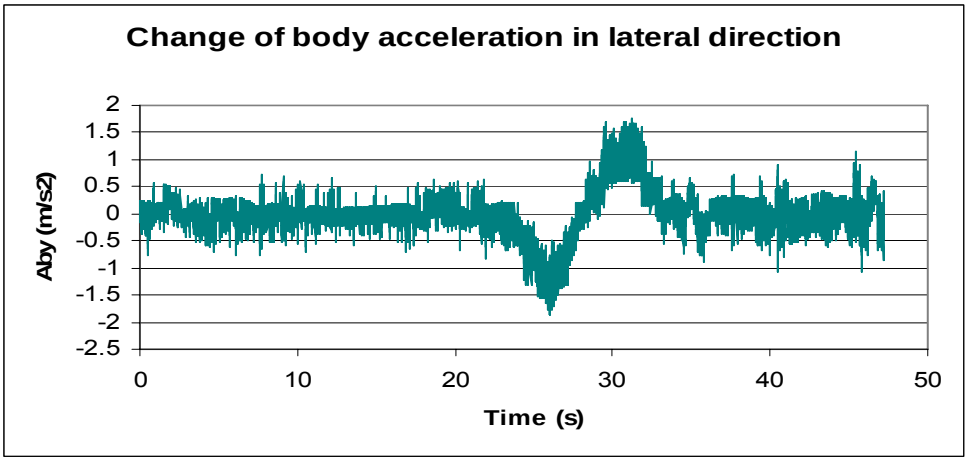

Figure 3.9 Plot of Body Acceleration in the Lateral (Y) Direction with Time for the Total Section.

The acceleration values of the tangent section in Figure 3.9 consistently lie within the upper and lower bounds defined for the tangent section. It is seen that this pattern changes once the vehicle enters the curve where the lateral acceleration component remains deviated from these bounds. By applying the above technique to the lateral acceleration (acceleration along the Y-axis of the body of the vehicle) record, it is possible to demarcate curved sections from tangent sections.

Figure 3.10 shows radii of curvature computed after separating the two curves from the linear sections using Eqn. (3.18). From Figure 3.10 one can also clearly observe the change in radius within the transition curves and the constant radius values in the circular sections.

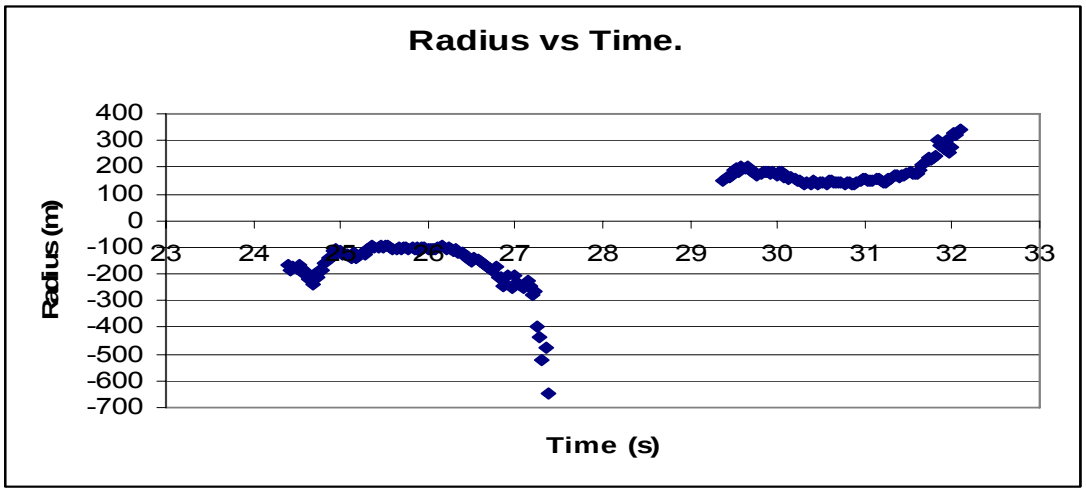

Figure 3.10 Curved Sections Separated from the Tangent Sections, Using Upper and Lower Bounds.

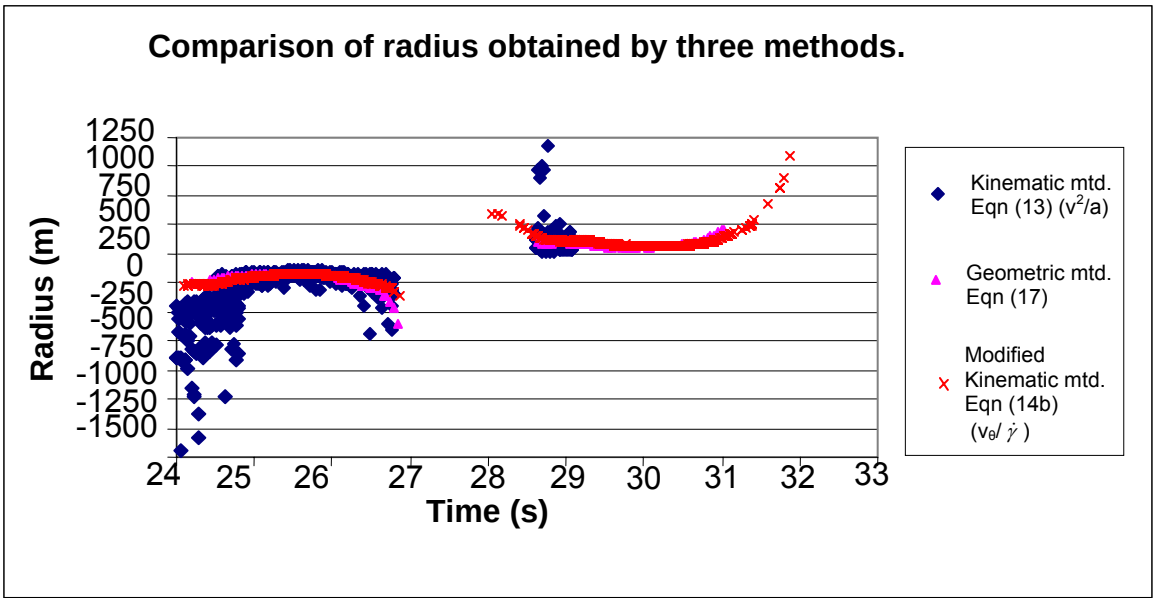

Figure 3.11 Comparison of Radii Values Calculated by (1) Using Eqn(3.14) , (2) Using Eqn (3.18), (3) Using Eqn (3.15-b).

Finally, in Figure 3.11 the radii values estimated by the three different approaches, (1) the kinematic method using Eqn (3.14), (2) the geometric method using Eqn (3.18) and (3) modified kinematic method using Eqn (3.15-b), are compared. It is clear that the radii values match well within the parts of the curve which are circular but deviate in the transition sections. The results emphasize the fact that the most accurate and stable solution for the transition sections are provided by the modified kinematic method.

3.6 Manual Estimation of Radius of curvature:

The radius of curvature was also estimated using a manual survey that involved using a total station to survey a number of stations along the curve (Fig. 3.12). The results of the manual survey are given in Table 3.4.

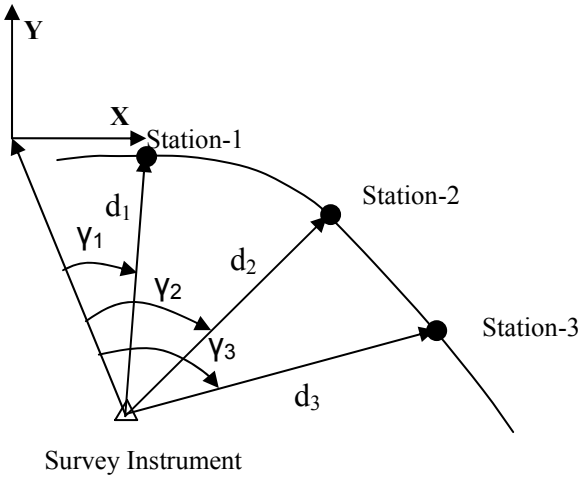

Figure 3.12 Illustration of notation used in Table 3.4

Table 3.4 Data obtained from the manual survey

Distance to stations (d) (ft)	Horizontal angle (γ)(deg)	X (ft)	Y (ft)
12.89	0	12.8900	0
28.36	58.37611	14.8703	-24.1488
46.33	68.54306	16.9476	-43.119
66.39	72.21167	20.2822	-63.216
86.58	73.74528	24.2344	-83.1191
106.36	74.20806	28.9453	-102.346
126.57	74.25056	34.3550	-121.818
161.37	73.59861	45.5652	-154.803
205.11	72.77528	60.7372	-195.911
225.29	72.7325	69.2826	-215.136
244.66	72.96361	72.4964	-233.672
264.86	73.38167	75.7486	-253.797
284.17	73.92778	78.6716	-273.063

In Table 3.4 third and fourth columns are calculated by Eqn. 3.26:

$$\begin{aligned} X &= d * \cos(\gamma) \\ Y &= d * \sin(\gamma) \end{aligned} \tag{3.26}$$

When three points that correspond to each of the two circular sections (curves 1 and 2) as identified by eye estimation are taken from Table 3.4 and fitted to a general equation of a circle (Eqn. 3.27), the results shown in Table 3.5 (manual evaluations) are obtained. The general equation of a circle can be given as,

$$(x-a)^2 + (y-b)^2 = r^2 \tag{3.27}$$

Where r is the radius of the circle and (a, b) are the coordinates of the center.

Table 3.5 Comparison of radius of curvature values obtained for the two curve segments.

	Manual method (m)	Compass method (m)	Geometric Method (m)	Kinematic method (m)	Modified kinematic method (m)
Segment 1	108.63	109.30	102.73	113.83	112.50
Segment 2	152.82	151.17	143.08	162.45	157.28

From Table 3.5 one can also see that the two curve segments of the reverse curve have different radii values and that the compass and modified kinematic methods agree well with the manually obtained values.

Figure 3.13 shows the radius of curvature calculated for curve 1 and curve 2 using the compass method described in Section 3.4.3.2. The angular difference at two consecutive points on the curve is obtained from the platform heading while the distance between two points was estimated by using Eqn. (3.17). Once the angular difference and the arc distance between two points are available the radius is calculated using Eqn (3.24).

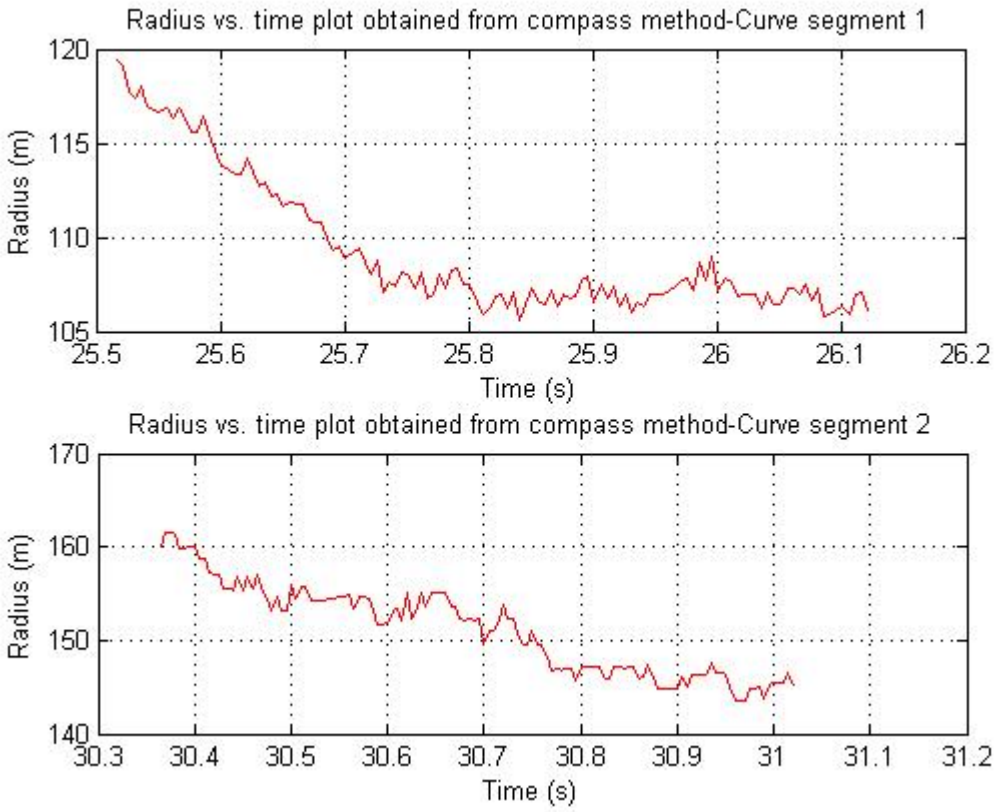

Figure 3.13 Radii values obtained by the compass method for two curves.

Finally, Fig. 3.14(a) and 3.14(b) show the comparison of radii curvature computed from all four methods (kinematic, Modified kinematic, Compass and Geometric) for both curve segments.

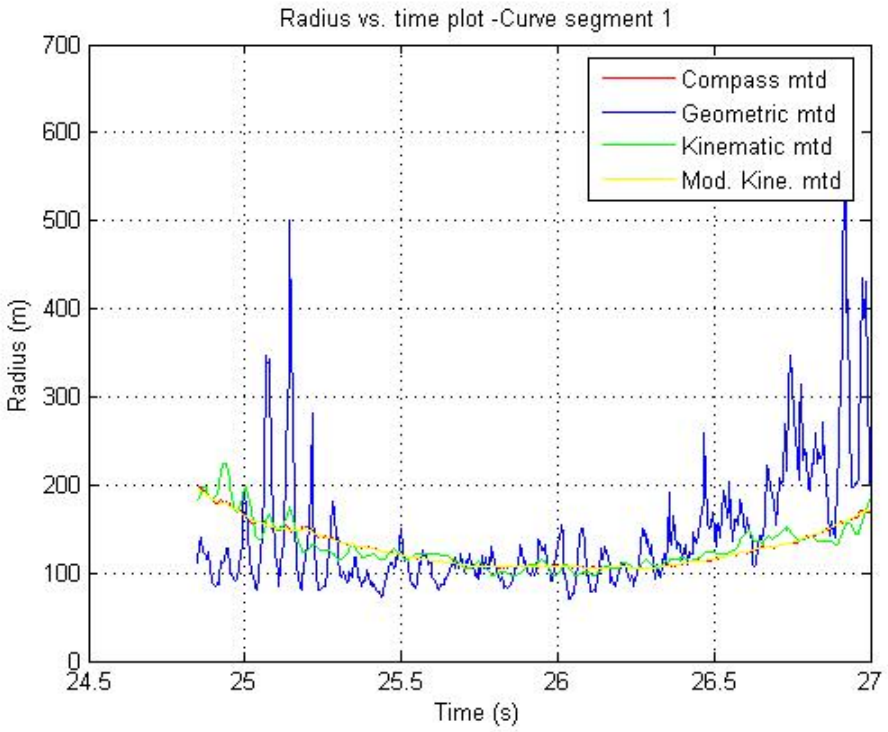

(a)

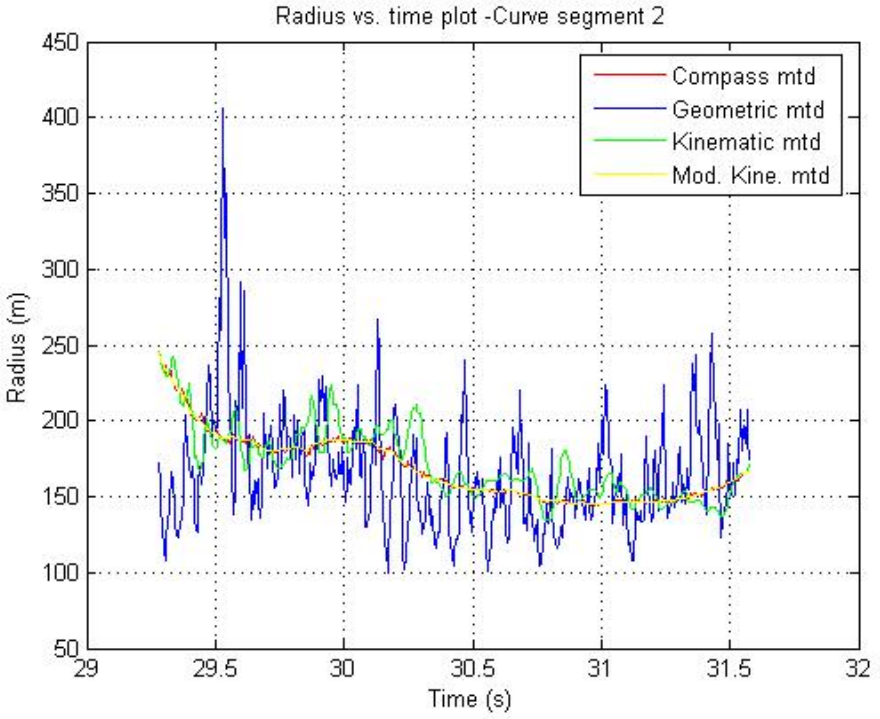

(b)

Figure 3.14 Comparison of Radius values obtained from 1) Compass method, 2) Geometric method, 3) Kinematic method and 4) Modified Kinematic method for (a) segment 1 and (b) segment 2 including transition curves.

3.7 Results from a preliminary study

The preliminary verification of the IMU data and the newly developed algorithms was continued during a preliminary study conducted on 39th Avenue, Gainesville, Florida in November 2004. During this study, a designated curved section of the above roadway was manually surveyed by FDOT to obtain (1) in-between wheel path cross-slopes and (2) edge-to-crown cross-slopes, at 37 locations, spaced at intervals of 50 to 100 feet. In addition, the radius of curvature of the roadway curve was also measured by FDOT.

Then, the MPSV was run along the designated roadway section at speeds of 30 mph, 40 mph, 50 mph and 60 mph with three (3) repetitions performed at each speed. Figures 3.15(a)-(d) illustrate how the average cross-slope measured at each speed compares with the manually measured cross slope between wheel paths.

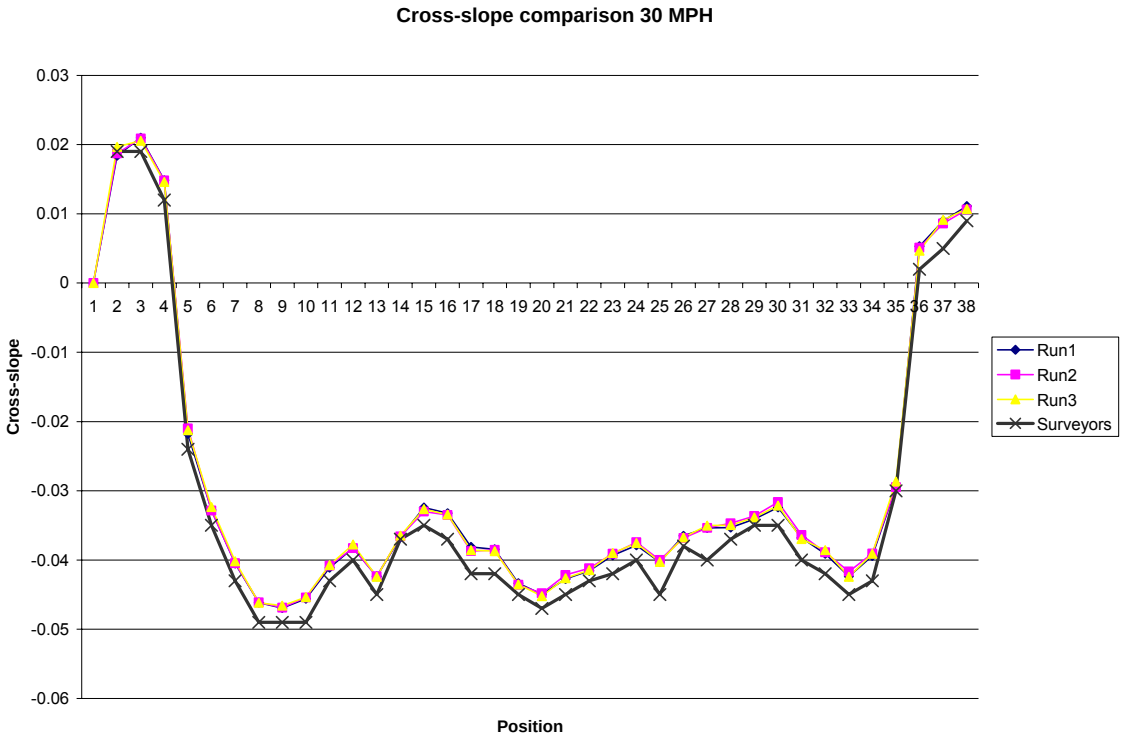

Figure 3.15(a) Comparison of IMU cross-slopes and surveyed cross-slopes at 30 mph

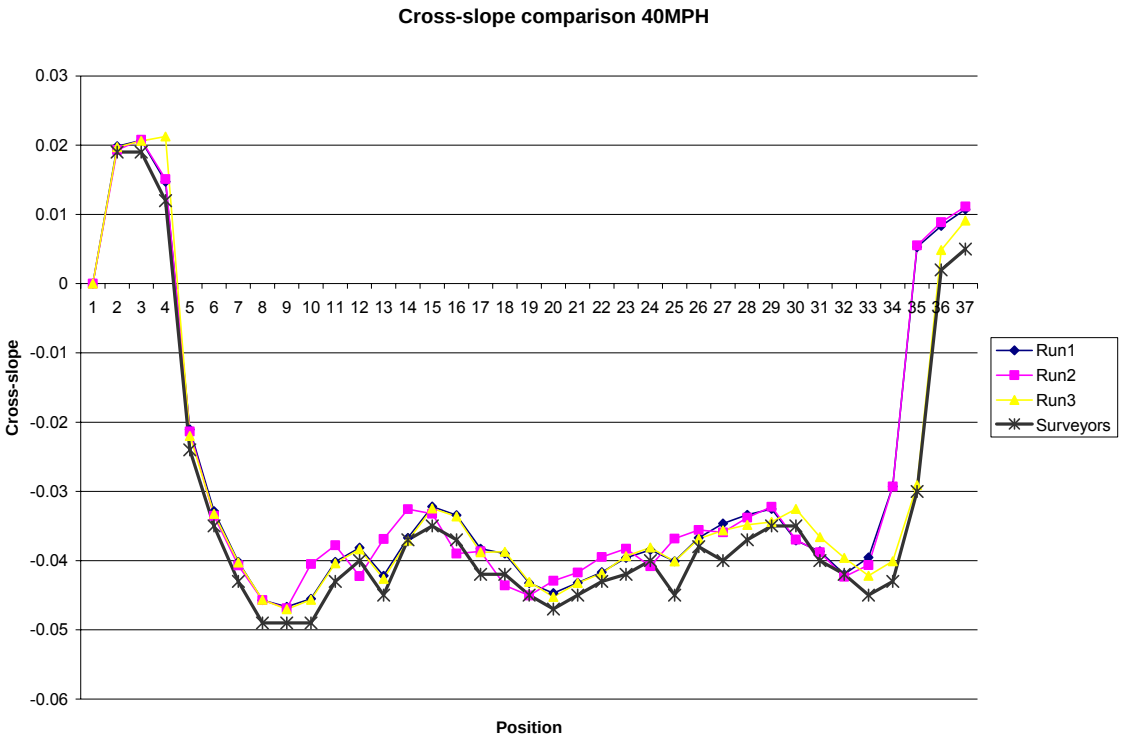

Figure 3.15(b) Comparison of IMU and surveyed cross-slopes at 40 mph

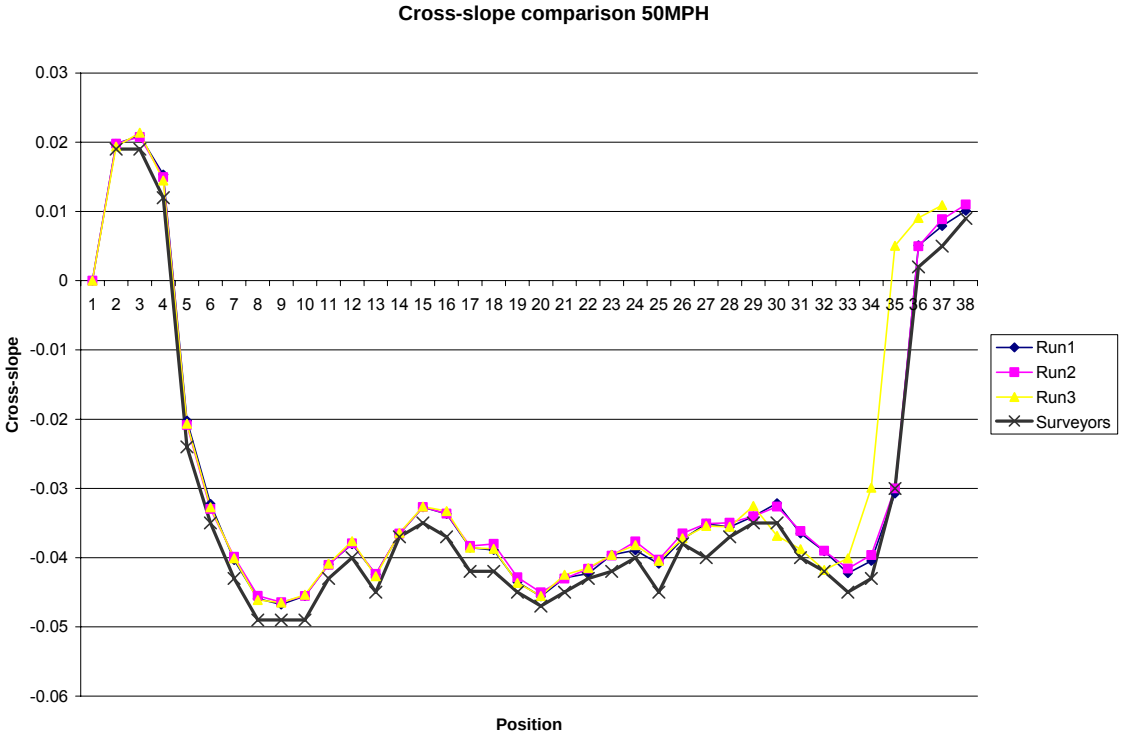

Figure 3.15(c) Comparison of IMU and surveyed cross-slopes at 50 mph

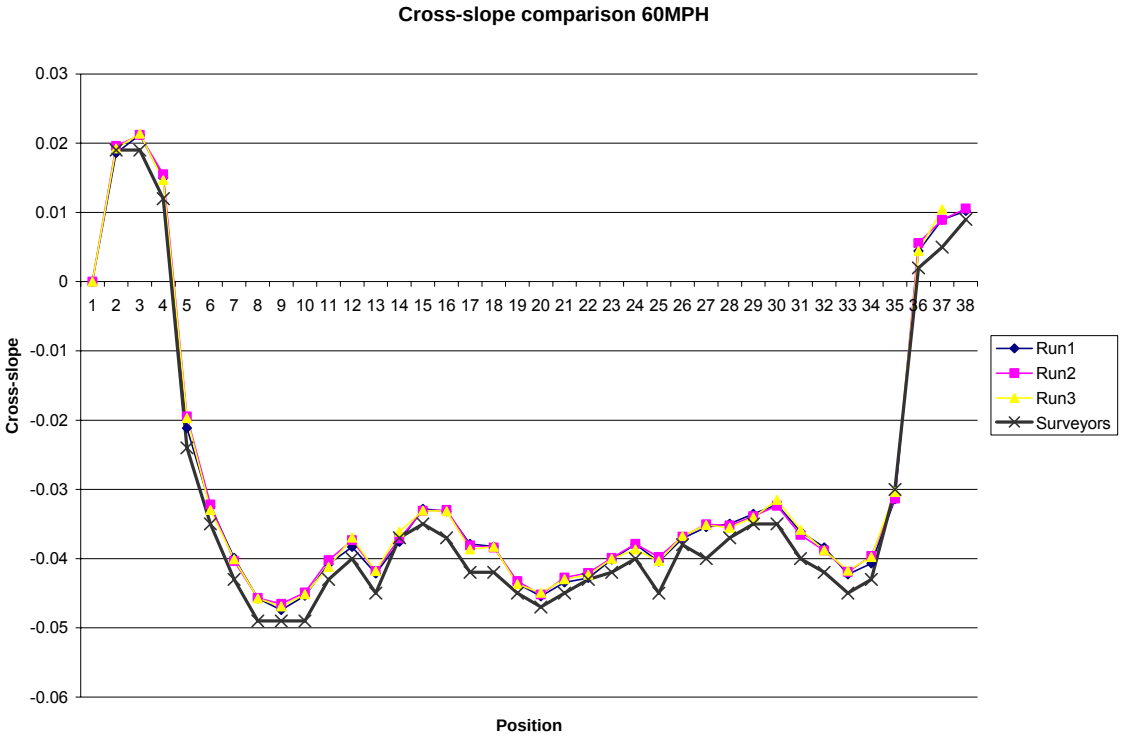

Figure 3.15(d) Comparison of IMU and surveyed cross-slopes at 60 mph

Inspection of the results presented in Figs. 3.15(a)-(d) indicates that the IMU cross-slope measurements are within the FDOT specified tolerance of 0.2% of the measured cross-slope except at one location (Station 35). Based on repeated manual measurements, it was concluded that the manual measurement was in error at this location.

Furthermore, Fig. 3.16 depicts the comparison between the variations of the radii of curvature along the above roadway section as predicted by (1) the modified kinematic method (2) the compass method, and (3) manual measurements.

From Fig. 3.16 it is seen that the radius of curvature results of both the modified kinematic method and the Compass method deviate from the surveyed measurement on a point to point basis. This is to be expected since it is extremely tedious for the vehicle

\

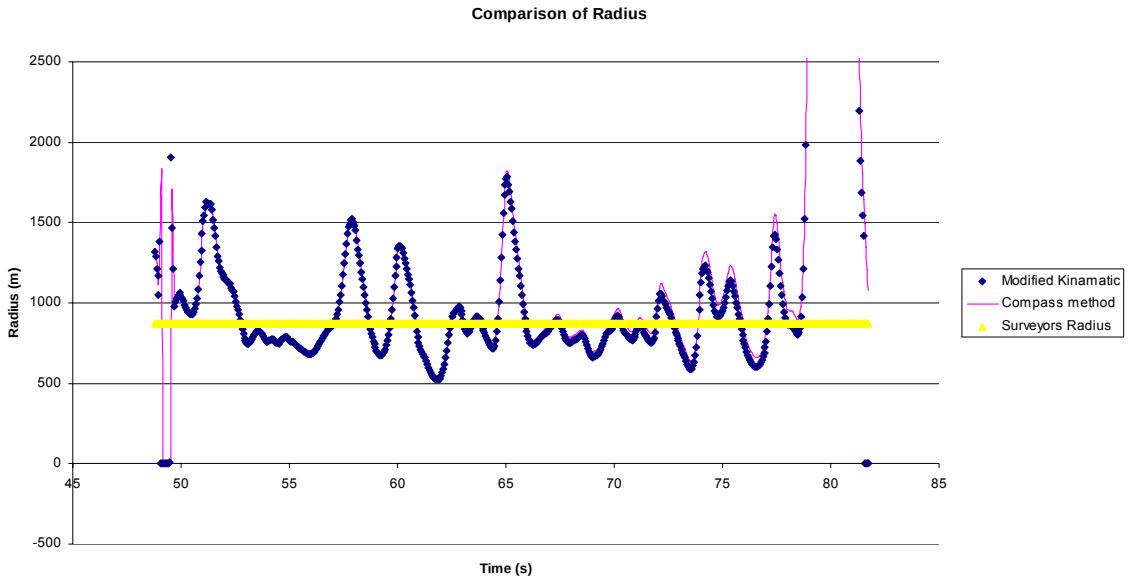

Fig. 3.16 Comparison of the variation of radii of curvature on the 39th Avenue (at 30 mph)

operator to track a curve without constant maneuvering the steering wheel. However, Fig. 3.16 also shows that the mean trends of the radius of curvature values predicted by both the kinematic and the Compass method closely agree with the radius of curvature obtained from the manual survey.

CHAPTER 4
DETAILED VALIDATION OF INERTIAL MEASUREMENTS

4.1 Introduction and Objectives:

The Position Orientation System/Land Vehicle (POS/LV) mounted on the FDOT Multi-functional survey vehicle is a high precision orientation system that uses military grade accelerometers and gyroscopes to measure the roll, pitch, and heading of the vehicle. Chapter 3 described how the information acquired with this orientation system coupled with laser height sensor measurements are used to determine the radii and super-elevations of horizontal curves, and cross-fall of straight roads, and grades.

Furthermore, during the preliminary investigation reported in Chapter 3, the above system was tested on the super-elevation of a newly overlaid asphalt pavement on 39th Avenue in Gainesville, FL. Therefore, the objectives of the extended study described in this chapter are to evaluate the accuracy and precision of the IMU (POS/LV) system. In this respect, measurements would be made on relatively new and distressed asphalt pavements (with relatively high IRI values) serving high speed facilities and urban arterials. The investigators were particularly interested in older road sections that exhibit distress due to cracking, rutting and raveling. On the other hand, concrete pavement sections were excluded from the study since they constitute only less than 4% of the state's highway network. In this exercise, the roadway cross-slope, grade, and horizontal curvature will be considered as the response variables (ASTM E177, E 950, E 1082, E 1489, E 1926). The controlled factors that have a pronounced effect on the geometric data are assumed to be (1) pavement surface distress, (2) vehicle speed, and (3) driver characteristics. The control treatment will also consist of conducting a conventional road survey of the test sections by the static level method (ASTM E 1364, AASHTO PP 31-04). Hence the specific objectives of the extended study are as follows:

i. The automated measurement of highway geometrics using the IMU and laser sensor subsystem that include:

a) Cross-slope,
b) Grade, and
c) Curvature,

ii. The manual measurement of cross-slope, grade, and horizontal curvature using conventional surveying instruments.
iii. Comparison of measurements in tasks (i) and (ii).

4.2 Design of the experimental procedure.

4.2.1 Effect of vehicle speed

Based on the typical speeds at which various road facility types are evaluated, it was determined to conduct the test runs at three speed levels. For the test runs on highways, it was decided to use the speeds of 45, 55 and 65 mph while in the case of urban arterials, testing would be conducted at 25, 35 and 45 mph.

4.2.2 Effect of driver characteristics

Once the minimum number of trials needed to achieve the desired accuracy is determined, two different drivers were expected to evaluate a given section for the above number of trials, to explore the effect of the driver characteristics on cross-slope survey results.

The above experimental details can be represented in a tree diagram as shown in Fig. 4.1

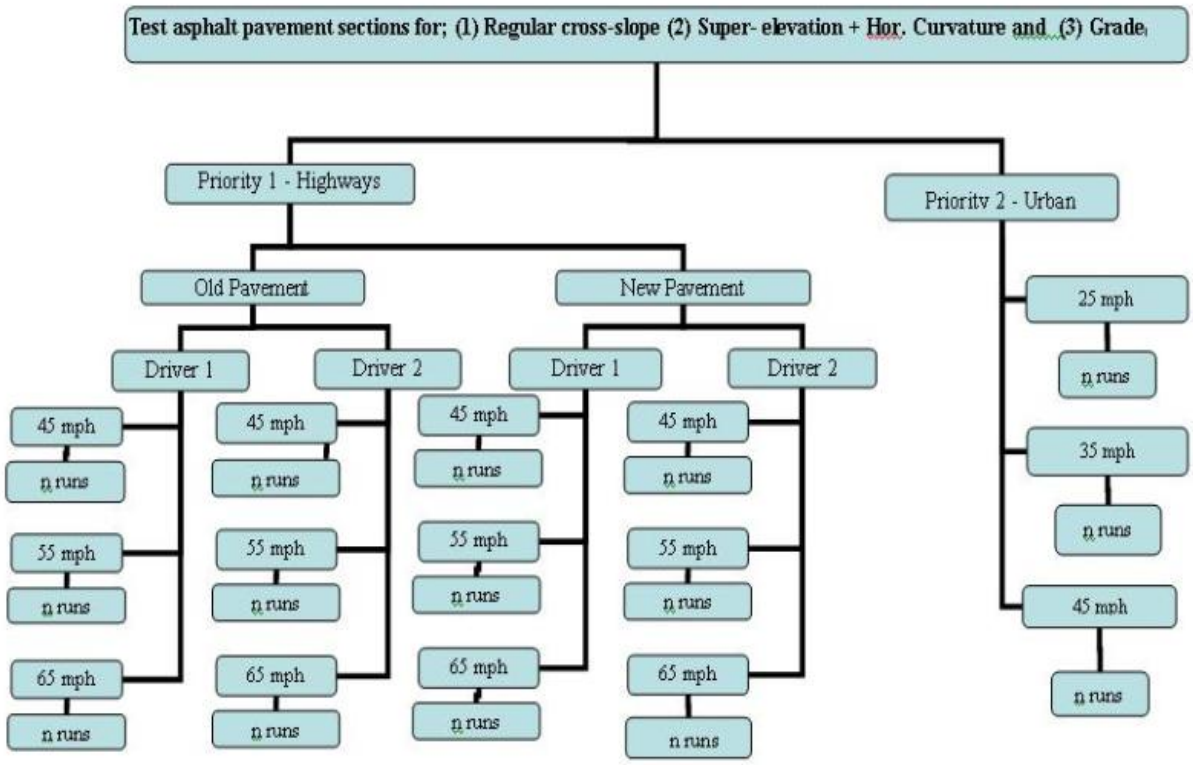

Figure 4.1 Tree diagram for the experimentation on evaluating cross-slope, grade and curvature on newly laid and distressed (high IRI) roadways

4.2.3 Determination of the number of trials, n.

For each combination of operating speed, roughness condition and driver, it is required to repeat the experiment for a minimum number of trials. This is done in order to ascertain that the results and conclusions would be statistically acceptable. The minimum number of trials required can be determined from the following statistical expression:

$$n = \left(\frac{SZ_{\alpha/2}}{\Delta} \right)^{1/2} \tag{4.1}$$

Where,

n = is the minimum number of trials for a given testing condition.

S = is the population standard deviation of the measurement variable

α= is the confidence level at which the considered measurement represents the actual value

Z = is the standard normal variate corresponding to a probability of α.

Δ = is the allowable tolerance between the measured values and the actual values.

S can be estimated from the standard deviation of an unbiased sample of representative road sections where cracking, rutting and raveling are manifested. Once *S* is found, one must decide on the confidence level α at which one would desire the IMU measurements to represent the actual geometric values. This value is taken typically as 95% to achieve a reasonably high accuracy. Finally, the tolerance allowed for the given road geometric measurement has to be determined. For the case of cross slopes, [FDOT, 2002] provides the typical allowable tolerance as 0.2%. On the other hand, the investigators were unable to find any such FDOT mandated tolerances for grade and curvature.

4.2.3.1 Computation of the number of trials, n, to achieve a specific confidence level in cross-slope measurements

The population standard deviation of the measurement variable, *S*, estimated from existing data of 15 runs in 10 locations was 0.0020194. The confidence level, α at which the measured cross-slope represents the actual value can be selected as (i) 90% or (ii) 95%. *Z*, the values of the standard normal variate corresponding to probabilities of α = 0.9 and 0,95 are found to be 1.65 and 1.96 from the standard normal distribution table, respectively. The allowable tolerance (Δ) between the measured values and the actual values is taken to be 0.2% (= 0.002).

Substituting in Eqn. (4.1),

Case (1) 90% Confidence

$$n = \left(\frac{0.0020194(1.65)}{0.002} \right)^2 \cong 3$$

Case (2) 95% Confidence

$$n = \left(\frac{0.0020194(1.96)}{0.002} \right)^2 \cong 4$$

Hence it was decided to use 5 repeat test runs at each speed.

4.3 Details of test sections

It was also decided that the test sections to be considered for this test must satisfy the following characteristics:

1. Only Asphalt Concrete pavement sections are considered with one of them significantly affected by both cracking and rutting since they are the most commonly manifested distress types in Florida's highway network. The remaining pavement section must be a relatively newly overlaid pavement.

2. When the experiment is performed on horizontal and vertical curves, the test sections must include lead-in and lead-out sections at their extremities that span at least 0.1 miles. This condition is required to allow the sensors of the IMU subsystem to stabilize before collecting data and allow for a safe stopping distance.

3. On a straight pavement section, the length of the section shall be greater than 0.2 miles [ASTM E 950] and it is advisable to allocate lead-in and lead-out sections of the same length.

Considering the above requirements it was decided to demarcate three sections; (1) straight run (2) horizontal curve with a super-elevation, and (3) vertical grade with an approximate lead-in and lead-out of 0.1 mile each for this experiment. It was found that two sections of SR-26 and US41 in Alachua county, Florida that borders neighboring Gilchrist and Levy County, not only satisfied the above testing pre-requisites but were also in close proximity to both the FDOT Materials Testing Center in Gainesvile, FL and the University of South Florida in Tampa. Of these, the relatively new pavement is a section on US 41 and the distressed section is a part of SR-26.

4.4 Other experimental considerations

Due to the unavailability of two trained drivers, it was decided to use only one driver. Furthermore, due to time and mandatory traffic control constraints it was also decided not to test urban arterials as envisaged in Section 4.1 and Fig. 4.1. The updated tree diagram showing the finally chosen experimental conditions is shown in Fig. 4.2

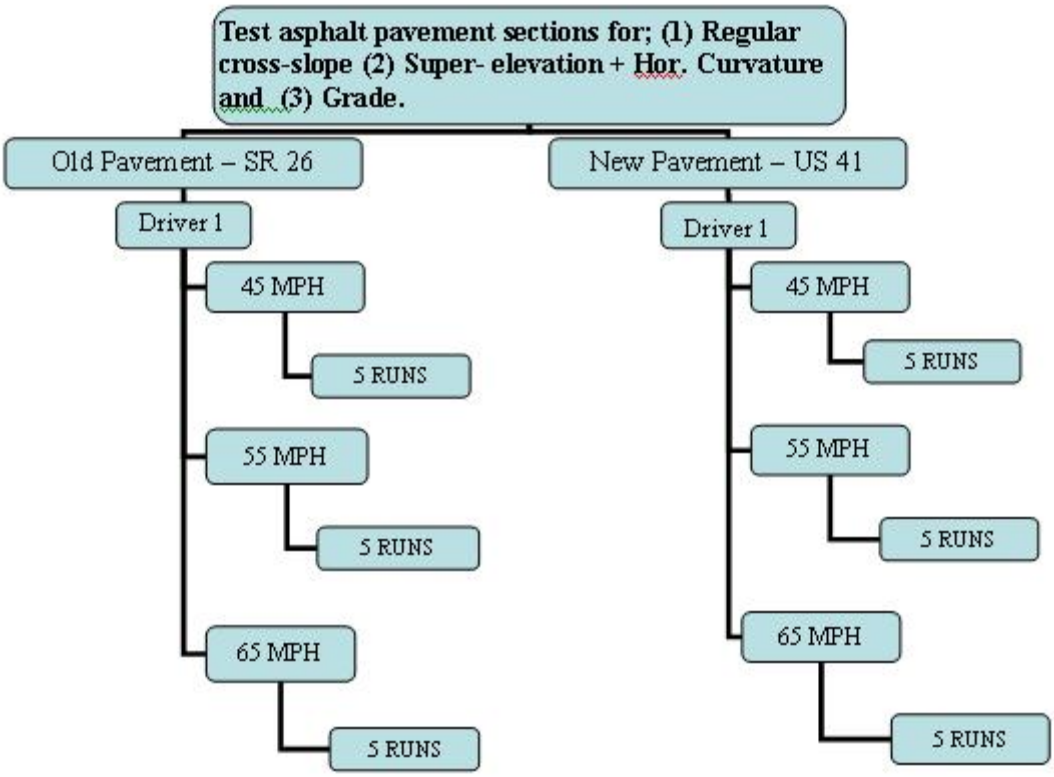

Fig. 4.2 Updated Tree diagram for the experimentation on evaluating cross-slope, grade and curvature on newly laid and distressed (high IRI) roadways

4.5 Calibration of the IMU and the laser subsystems and DMI

The preliminary investigation on smooth pavement sections reported in Chapter 3 has revealed the occurance of a systematic error in the cross-slope data. It is quite logical to attribute this systematic error to possible errors in the calibration of the IMU/laser subsystems. To address this issue it was decided to accurately calibrate the above

subsystems prior to actual testing. The IMU calibration procedure is documented in Appendix A.

Furthermore, a separate in-house testing program conducted by FDOT has shown a systematic error in the vehicle's DMI readings as well. This has been seen to occur especially during relatively long runs, and thus could be attributable to changes in the physical characteristics of the vehicle tires. In order to quantify the extent of this error, based on the duration of the vehicle operation it was decided to calibrate the vehicle's DMI as well. The relevant calibration procedure is documented in Appendix B.

4.6 Operational guidelines for testing:

In order to facilitate repeatable and accurate testing conditions, the following guidelines for testing were formulated:

1. The operator of the vehicle will be directed to perform evaluation of the pavement sections at the designated speeds for the specified number of trials in a systematic fashion, each time switching the data collection and recording systems on and off at previously designated locations .
2. Before the start of the test, the equipment must be calibrated as noted in Section 4.5. This must also include calibrating the lasers and checking the tire pressures and temperatures as recommended by the relevant standards [ASTM E 1082]. In addition, the accelerometers on the front bumper must also be checked under the weather condition that prevails during the test.
3. A constant speed must be maintained during the test and the vehicle must attain this speed during the "lead-in" to the test section. If the vehicle operator fails to maintain the required constant speed during the run that run shall be aborted.
4. All the runs required for one particular section must be made under similar weather and traffic conditions.

4.7 Manual surveying of the test sections

The manual survey of cross-slope must be conducted on the straight run and the horizontal curve, while manual survey of grade must be performed on the vertical grade portion. In addition, the curvature of the horizontal curve must be determined by fitting a circular curve that traverses the stations surveyed on each curved section located on the curve with the maximum curvature or the minimum radius of curvature.

1. Frequency of measurements To be in par with the frequency of automated data logging, and in order to ground-truth the IMU data on a point by point basis, ideally the manual survey data must be available at intervals of 2.6 ft, 3.4 ft and 5.3 ft for speeds of 45, 55 and 65 mph respectively for highways. However, it is impractical to manually survey the sections for road geometry data at such small intervals. Therefore, from a practical point of view, the investigators believe that, for typical test sections specified in the experimental plan (Section 4.2) the manual survey must be conducted at every 100 ft interval. This would require cross-slope and grade readings to be obtained in the horizontal and vertical curves respectively at every 100 feet. Moreover, the cross-slope readings on the straight section must also be taken at the same interval of 100 feet. In addition, station locations must be measured at every 100 feet along the horizontal curve for accurate determination of the horizontal curvature.

Therefore, some reflective tape was laid out across the lane at 100 foot intervals at each of the test sections in order to prompt the IMU data recorder to track the manually surveyed locations. The tape locations were designated using a station number and the type of geometry (ex. curve, straight run or grade). As an example, the eighth station on the grade portion in each roadway is designated as Station 8G. At each designated station, The manual survey was performed by measuring heights of the stations in the two wheel-paths and the edge and crown of the pavement section using a calibrated survey rod and a Total Station. Thus, the investigators would be able to compare the vehicle's IMU readings with two sets of manually measured cross-slopes.

2. Allowable tolerance. Since the allowable tolerance for cross-slopes is 0.2%, the tolerance for manual survey measurements shall be no greater than 0.1% as the reference device must have a measurement uncertainty no greater than ½ of the required accuracy of the equipment. A number of trial manual surveys at the University of South Florida confirmed that the USF survey crew could achieve the above specified accuracy and precision. Therefore, it was assumed that the Rod and Total Station survey would suffice to achieve the above tolerance during the actual field experimentation as well. As an extra precaution, the investigators verified the reading by simply repeating each measurement at least twice.

4.7.1 Total Station Accuracy

A simple experiment was conducted at USF to establish the accuracy of the total station. In this experiment, two graduations spaced at 0.5 meters on a surveyor's level were surveyed by the total station in two trials. The horizontal distances (285 feet and 330 feet) for sighting the level were chosen so that they represented horizontal distances that were typically used during the manual survey of cross-slopes. The following results were obtained during the trials:

Trial 1

Ground-truth tangent (slope) of the angle subtended by the sighted graduations at the total station = 0.574%

Measured tangent (slope) of the angle subtended by the sighted graduations at the total station = 0.570%

Error in slope = -0.004%

Trial 2

Ground-truth tangent (slope) of the angle subtended by the sighted graduations at the total station = 0.496%

Measured tangent (slope) of the angle subtended by the sighted graduations at the total station = 0.499%

Error in slope = +0.003%

Hence it was concluded that the magnitude of the slope measurement error associated with the total station is less than 0.004%

4.8 Evaluation of IMU measurements

4.8.1 Precision of IMU measurements

Based on the precision concepts specified in ASTM (E177-90a), the precision (*P*) of the IMU measurement can be defined as:

$$P(\%) = 100 - \frac{Max\left|X_i - \frac{\sum X_i}{n}\right|}{\frac{\sum X_i}{n}} x100 \qquad (4.2)$$

Where X_i = IMU measurement of a geometric quantity (cross-slope, radius of curvature or grade) on the ith repetition.

n =Total number of repetitions

4.8.2 Accuracy of IMU measurements

Based on the accuracy concepts specified in ASTM (E177-90a), the Accuracy (*A*) of an instrument reading can be defined as:

$$A(\%) = 100 - \frac{\left|Y - \frac{\sum X_i}{n}\right|}{Y} x100 \qquad (4.3)$$

Where X_i = IMU measurement of a geometric quantity (cross-slope, radius of curvature or grade) on the ith repetition.

n= Total number of repetitions

Y= Corresponding manual measurement

4.9 Results of detailed testing program

In conclusion of the above described testing program, IMU measurements of road cross-slope (including super-elevations), two comparisons were made; (1) comparison of radii of curvature and grades among the repeated runs at the designated locations, and (2) comparison of the averages of radii curvature and grades with the results from the manual survey. The results from the two types of comparisons were expressed respectively, in terms of (1) repeatability (precision) of the IMU readings and (2) the accuracy (bias) with respect to the manual measurements.

4.9.1 Precision of cross-slopes

The precision of cross-slope readings provided by the IMU subsystem of MPSV as computed by Eqn. (4.2) is illustrated in Tables 4.1(a)-(c) for the newly laid pavement (US 41) for speeds of 45, 55 and 65 mph, respectively. On the other hand, the corresponding results for the relatively aged pavement (SR 26) are shown in Tables 4.2(a)-(b) corresponding to speeds of 45 and 55 mph, respectively. Data at 65 mph was not available for the latter section.

Table 4.1(a) Cross-slope Precision Results on New Pavement US-41 @45 mph

	Percent Cross-slope						
STATION/RUN	1	2	3	4	5	AVERAGE	PRECISION(%)
G21	2.72	2.73	2.80	2.75	2.75	2.75	98.31
G22	2.63	2.65	2.68	2.61	2.64	2.64	98.48
G23	2.34	2.35	2.39	2.33	2.33	2.35	98.27
G24	1.95	2.04	2.06	2.00	2.01	2.01	96.91
C31	2.42	2.48	2.44	2.40	2.46	2.44	98.36
C32	2.38	2.35	2.31	2.34	2.36	2.35	98.59
C33	2.37	2.29	2.32	2.30	2.31	2.32	97.96
C34	2.11	2.17	2.08	2.07	2.09	2.10	96.75

Average of cross-slope precision at 45 mph = 97.95%
Standard deviation of cross-slope precision at 45 mph =0.72%

Table 4.1(b) Cross-slope Precision Results on New Pavement US-41 @55 mph

STATION/RUN	Percent Cross-slope					AVERAGE	PRECISION(%)
	1	2	3	4	5		
G21	2.76	2.79	2.93	2.72	2.79	2.80	95.31
G22	2.72	2.75	2.78	2.72	2.74	2.74	98.71
G23	2.45	2.42	2.46	2.40	2.41	2.43	98.62
G24	2.09	2.06	2.16	2.09	2.07	2.09	96.92
C31	2.49	2.49	2.44	2.54	2.55	2.50	97.43
C32	2.40	2.39	2.29	2.44	2.45	2.40	95.94
C33	2.34	2.40	2.32	2.37	2.42	2.37	97.79
C34	2.24	2.20	2.12	2.23	2.27	2.21	95.94

Average of cross-slope precision at 55 mph = 97.08%
Standard deviation of cross-slope precision at 55 mph = 1.28%

Table 4.1(c) Cross-slope Precision Results on New Pavement US-41 @65 mph

STATION/RUN	Percent Cross-slope					AVERAGE	PRECISION(%)
	1	2	3	4	5		
G21	2.91	2.78	2.82	2.77	2.87	2.83	97.39
G22	2.75	2.65	2.69	2.72	2.74	2.71	97.70
G23	2.46	2.42	2.53	2.44	2.49	2.47	97.37
G24	2.11	2.10	2.15	2.11	2.15	2.12	98.70
C31	2.69	2.66	2.69	2.56	2.51	2.62	95.74
C32	2.47	2.49	2.46	2.40	2.40	2.44	98.02
C33	2.41	2.38	2.39	2.34	2.29	2.36	97.06
C34	2.37	2.33	2.33	2.27	2.26	2.31	97.48

Average of cross-slope precision at 65 mph = 97.43%
Standard deviation of cross-slope precision at 65 mph = 0.85%

Table 4.2(a) Cross-slope Precision Results on Old Pavement SR-26 @45 mph

STATION/RUN	Percent Cross-slope					AVERAGE	PRECISION(%)
	1	2	3	4	5		
13C	2.66	2.69	2.71	2.68	2.70	2.69	98.90
13C1	2.85	2.95	2.85	2.85	2.97	2.90	97.40
13C2	3.10	3.16	3.12	3.15	3.20	3.15	98.37
13C3	3.29	3.37	3.34	3.37	3.36	3.34	98.28
13C4	3.32	3.41	3.35	3.46	3.42	3.39	97.90
3S	1.56	1.66	1.60	1.60	1.62	1.61	96.89
3S1	1.39	1.46	1.44	1.42	1.44	1.43	97.12
3S2	1.06	1.20	1.17	1.08	1.14	1.13	93.67
3S3	0.50	0.63	0.55	0.50	0.58	0.55	Outlier

3S4	0.13	0.21	0.20	0.13	0.21	0.18	Outlier

Average of cross-slope precision at 45 mph = 96.1%
Standard deviation of cross-slope precision at 45 mph = 3.76%

Table 4.2(b) Cross-slope Precision Results on Old Pavement SR-26 @55 mph

	Percent Cross-slope						
STATION/RUN	1	2	3	4	5	AVERAGE	PRECISION(%)
13C	2.59	2.74	2.66	2.70	2.68	2.67	96.86
13C1	2.63	2.78	2.79	2.77	2.77	2.75	95.67
13C2	2.84	3.15	3.10	3.11	3.03	3.04	93.21
13C3	3.11	3.33	3.27	3.30	3.24	3.25	95.60
13C4	3.25	3.38	3.37	3.34	3.42	3.35	97.05
3S	1.50	1.57	1.63	1.54	1.58	1.56	95.81
3S1	1.36	1.47	1.47	1.45	1.47	1.44	94.46
3S2	1.15	1.17	1.25	1.22	1.17	1.19	94.81
3S3	0.60	0.65	0.68	0.67	0.62	0.64	93.33
3S4	0.18	0.19	0.24	0.25	0.19	0.21	Outlier

Average of cross-slope precision at 55 mph = 95.2%
Standard deviation of cross-slope precision at 55 mph = 1.29%

Table 4.2(c) Cross-slope Precision Results on Old Pavement SR-26 @65 mph

	Percent Cross-slope						
STATION/RUN	1	2	3	4	5	AVERAGE	PRECISION(%)
13C	2.60	2.69	2.72	2.71	2.72	2.69	96.58
13C1	2.69	2.63	2.69	2.66	2.71	2.68	98.46
13C2	2.83	2.89	2.93	2.89	2.88	2.89	98.12
13C3	3.10	3.14	3.13	3.11	3.10	3.12	99.18
13C4	3.26	3.35	3.30	3.31	3.28	3.30	98.43
3S	1.58	1.58	1.57	1.67	1.52	1.58	94.54
3S1	1.42	1.44	1.43	1.47	1.38	1.43	96.83
3S2	1.19	1.19	1.25	1.25	1.21	1.22	97.26
3S3	0.77	0.80	0.78	0.82	0.80	0.80	96.85
3S4	0.30	0.35	0.39	0.34	0.41	0.36	Outlier

Average of cross-slope precision at 65 mph = 96.0%
Standard deviation of cross-slope precision at 55 mph = 4.18%

The precision of cross-slopes can be summarized in Table 4.3. Based on the results in Table 4.3 it can be concluded at 95% confidence that, the cross-slope results from two repeated runs properly conducted on a newly laid pavement under similar evaluation conditions using the same laser and POS/LV systems, would be within 5% of their average. However, the above margin of error increases to 7% for relatively aged pavements.

Table 4.3 Summary of Cross-slope Precision

Speed (mph)	45	55	65	45	55	65
Precision parameter (%)/Facility	US 41 (Newly laid)			SR-26 (Relatively aged)		
Average	97.95	97.1	97.43	96.09	95.2	96.03
Std. Deviation	0.72	1.28	0.85	3.76	1.29	4.18
Lower bound of the 95% confidence interval	96.5	95.0	95.7	93.0	93.0	94.0
Margin of error	3.5	5.0	4.3	7.0	7.0	6.0

4.9.2 Cross-slope accuracy

The accuracy of the IMU cross-slope readings as computed by Eqn. (4.3) is illustrated in Tables 4.4(a)-(c). Similarly, the corresponding results for the relatively aged pavement (SR 26) are shown in Tables 4.5(a)-(c). Based on these results, it can be concluded that the accuracy of IMU cross-slope data is satisfactory for both the newly laid pavement and the aged pavement. However, for SR-26, at one location (station 9G) the accuracy of cross-slope measurement was around 60% at all evaluation speeds. Hence one could attribute this consistently low accuracy to an error in the manual cross-slope measurement at that location.

Table 4.4 (a) Cross-slope Accuracy Results on US-41 @45 mph

STATION	Percent Cross-slope		ACCURACY(%)
	IMU AVERAGE	MANUAL SURVEY	
G21	2.75	2.69	97.62
G22	2.64	2.50	94.23
G23	2.35	2.37	99.31
G24	2.01	2.32	86.60
C31	2.44	2.83	86.16
C32	2.35	2.65	88.54
C33	2.32	2.56	90.49
C34	2.10	2.13	98.99

Table 4.4 (b) Cross-slope Accuracy Results on US-41 @55 mph

STATION	Percent Cross-slope		ACCURACY(%)
	IMU AVERAGE	MANUAL SURVEY	
G21	2.8	2.69	95.78
G22	2.74	2.5	90.22
G23	2.43	2.37	97.23
G24	2.09	2.32	90.05
C31	2.5	2.83	88.48
C32	2.4	2.65	90.40
C33	2.37	2.56	92.42
C34	2.21	2.13	95.85

Average of cross-slope accuracy at 55 mph = 92.6%
Standard deviation of cross-slope accuracy at 55 mph = 3.3%

Table 4.4 (c) Cross-slope Accuracy Results on US-41 @65 mph

STATION	Percent Cross-slope		ACCURACY(%)
	IMU AVERAGE	MANUAL SURVEY	
G21	2.83	2.69	94.50
G22	2.71	2.50	91.49
G23	2.47	2.37	95.57
G24	2.12	2.32	91.37
C31	2.62	2.83	92.76
C32	2.44	2.65	92.15
C33	2.36	2.56	92.19
C34	2.31	2.13	91.33

Average of cross-slope accuracy at 65 mph = 92.7%
Standard deviation of cross-slope accuracy at 65 mph = 1.57%

Table 4.5 (a) Cross-slope Accuracy Results on SR-26 @45 mph

STATION	Percent Cross-slope		ACCURACY(%)
	IMU AVERAGE	MANUAL SURVEY	
13C	2.69	2.85	94.38
13C1	2.90	2.84	97.97
13C2	3.15	3.23	97.27
13C3	3.34	3.52	94.98
13C4	3.39	3.48	97.57
3S	1.61	1.63	98.31
3S1	1.43	1.42	99.06
3S2	1.13	1.17	96.88
3S3	0.55	0.52	93.81
3S4	0.18	0.12	Outlier

Average of cross-slope accuracy at 45 mph = 96.7%
Standard deviation of cross-slope accuracy at 45 mph = 1.86%

Table 4.5 (b) Cross-slope Accuracy Results on SR-26 @55 mph

STATION	Percent Cross-slope		ACCURACY(%)
	IMU AVERAGE	MANUAL SURVEY	
13C	2.69	2.85	94.38
13C1	2.90	2.84	97.97
13C2	3.15	3.23	97.27
13C3	3.34	3.52	94.98
13C4	3.39	3.48	97.57
3S	1.61	1.63	98.31
3S1	1.43	1.42	99.06
3S2	1.13	1.17	96.88
3S3	0.55	0.52	93.81
3S4	0.18	0.12	Outlier

Average of cross-slope accuracy at 55 mph = 93.49%
Standard deviation of cross-slope accuracy at 55 mph = 6.7%

Table 4.5(c) Cross-slope Accuracy Results on SR-26 @65 mph

STATION	Percent Cross-slope		ACCURACY(%)
	IMU AVERAGE	MANUAL SURVEY	
13C	2.69	2.85	94.41
13C1	2.68	2.84	94.25
13C2	2.89	3.23	89.23
13C3	3.12	3.52	88.55
13C4	3.30	3.48	94.78
3S	1.58	1.63	96.69
3S1	1.43	1.42	99.41
3S2	1.22	1.17	95.92
3S3	0.80	0.52	Outlier
3S4	0.36	0.12	94.90

Average of cross-slope accuracy at 65 mph = 94.24%
Standard deviation of cross-slope accuracy at 65 mph = 3.42%

The accuracy of cross-slopes can be summarized in Table 4.6. Based on the results in Table 4.6 it can be concluded at 95% confidence that, the cross-slope results from a properly conducted run on a newly laid pavement would be within 14% of the ground-truth. The above margin of error decreases slightly to 12% for relatively aged pavements.

Table 4.6 Summary of Cross-slope Accuracy

Speed (mph)	45	55	65	45	55	65
Accuracy parameter (%)	US 41 (Newly laid)			SR-26 (Relatively aged)		
Average	92.7	92.6	92.7	96.7	93.49	94.24
Std. Deviation	5.5	3.3	1.57	1.86	6.7	3.42
Lower bound of the 95% confidence interval	86.0	88.0	90.0	93.0	93.0	88.0
Margin of error	14.0	12.0	10.0	7.0	7.0	12.0

4.9.3 Precision and Accuracy of radius of curvature measurements

As described in Chapter 3, the preliminary radius of curvature data can be analyzed effectively using two methods; (1) the modified kinematic method (Eqn. 3.14(b)) which would be identified in this chapter as the USF method, and (2) the Compass method (Eqn. 3.23). The results of curvature measurements on SR-26 (relatively aged pavement) using the USF and the Compass method are summarized in Tables 4.7 (a)-(f). One can observe some disparity between the curvature values depending on the method of analysis.

On the other hand, the corresponding results for US-41, the newly laid pavement, are shown in Tables 4.8(a)-(f). From the latter set of tables, it is seen that, at speeds of 35 and 45 mph, the radius of curvature computed using the USF method and the Compass method are almost identical. However, at 55 mph, the curvature values obtained from the two methods deviate from each other.

Table 4.7(a) Radius of Curvature Results on SR 26 based on USF Method @ 35 mph

STATION\RUN	All radius values are in feet							PRECISION(%)	ACCURACY(%)
	1	2	3	4	5	AVERAGE	MANUAL SURVEY		
11c	3939.90	1561.30	1187.90	2125.20	1299.80	2022.80	1791.20	5.22	87.06
12c	1574.50	1131.90	2537.70	1681.70	2384.00	1862.00	1791.20	60.79	96.04
13c	1417.50	1447.30	1314.30	955.50	1282.10	1283.30	1791.20	74.45	71.64
14c	3409.60	1860.00	3472.10	4368.20	5816.90	3785.40	1791.20	46.33	Outlier

Table 4.7(b) Radius of Curvature Results on SR 26 based on the Compass Method @ 35 mph

STATION\RUN	All radius values are in feet							PRECISION(%)	ACCURACY(%)
	1	2	3	4	5	AVERAGE	MANUAL SURVEY		
11c	2984.20	1248.50	913.70	1668.30	993.70	1561.70	1791.20	8.90	87.18
12c	1193.90	839.60	1979.50	1262.70	1832.20	1421.50	1791.20	59.06	79.36
13c	1058.60	1142.30	1017.40	737.30	951.10	981.30	1791.20	75.13	54.78
14c	2583.70	1372.60	2491.00	3235.50	4313.40	2799.20	1791.20	45.90	43.72

Table 4.7(c) Radius of Curvature Results on SR 26 based on USF Method @ 45 mph

STATION\RUN	All radius values are in feet							PRECISION(%)	ACCURACY(%)
	1	2	3	4	5	AVERAGE	MANUAL SURVEY		
11c	1509.40	1662.30	1269.70	1734.10	1239.50	1483.00	1791.20	.83.06	82.79
12c	1600.40	1326.40	3137.90	1212.40	1548.90	1765.20	1791.20	22.23	98.55
13c	982.00	1391.50	1221.40	1156.60	7004.10	2351.20	1791.20	-97.90	68.73
14c	1753.20	1552.00	2600.80	1960.70	2603.20	2094.00	1791.20	74.11	83.09

Table 4.7(d) Radius of Curvature Results on SR 26 based on the Compass Method @ 45 mph

	All radius values are in feet								
STATION\RUN	1	2	3	4	5	AVERAGE	MANUAL SURVEY	PRECISION(%)	ACCURACY(%)
11c	1145.40	1251.20	955.40	1290.10	913.00	1111.00	1791.20	82.17	62.02
12c	1274.50	1034.90	2521.00	906.70	1190.00	1385.40	1791.20	18.03	77.34
13c	754.80	1063.90	944.40	890.50	5951.10	1921.00	1791.20	-109.80	92.75
14c	1432.00	1217.00	2162.00	1577.70	2078.70	1693.50	1791.20	71.86	94.54

Table 4.7(e) Radius of Curvature Results on SR 26 based on USF Method @ 55 mph

	All radius values are in feet								
STATION\RUN	1	2	3	4	5	AVERAGE	MANUAL SURVEY	PRECISION(%)	ACCURACY(%)
11c	1186.70	1412.60	1026.50	1832.30	1760.60	1443.80	1791.20	71.09	80.60
12c	1727.30	2140.70	2914.20	1901.80	2021.90	2141.20	1791.20	63.89	80.46
13c	1204.90	1239.50	1435.30	1654.10	1263.00	1359.30	1791.20	78.31	75.89
14c	2384.80	3597.10	4393.80	2516.90	2189.40	3016.40	1791.20	54.33	31.59

Table 4.7(f) Radius of Curvature Results on SR 26 based on the Compass Method @ 55 mph

	All radius values are in feet								
STATION\RUN	1	2	3	4	5	AVERAGE	MANUAL SURVEY	PRECISION(%)	ACCURACY(%)
11c	902.60	1070.70	783.50	1329.00	1298.90	1076.90	1791.20	72.74	60.12
12c	1339.60	1618.30	2252.90	1449.40	1568.20	1645.70	1791.20	63.10	91.87
13c	930.90	931.60	1087.40	1278.60	974.10	1040.50	1791.20	77.11	58.09
14c	1889.10	2726.40	3357.00	1927.30	1709.60	2321.90	1791.20	55.42	70.36

Table 4.8(a) Radius of Curvature Results on US 41 based on USF Method @ 35 mph

STATION\ RUN	All radius values are in feet							PRECISION(%)	ACCURACY
	1	2	3	4	5	AVERAGE	MANUAL SURVEY		
3C	998.80	813.40	738.50	1375.20	718.90	928.90	929.80	51.96	99.90
4C	1053.10	833.40	728.80	1093.70	1012.30	944.30	929.80	77.17	98.45
7C	1468.90	1216.90	1049.90	991.50	875.00	1120.40	929.80	68.90	79.50
8C	913.10	973.60	1226.30	995.50	832.10	988.20	929.80	75.89	93.73
9C	752.20	971.20	1003.30	765.60	1002.20	898.90	929.80	83.68	96.67

Table 4.8(b) Radius of Curvature Results on US 41 based on Compass Method @ 35 mph

STATION\RUN	All radius values are in feet							PRECISION(%)	ACCURACY
	1	2	3	4	5	AVERAGE	MANUAL SURVEY		
3C	1013.50	825.80	737.60	1341.90	708.50	925.50	929.80	54.99	99.52
4C	1074.00	831.20	731.80	1118.50	997.30	950.60	929.80	76.98	97.77
7C	1488.30	1232.00	1057.00	980.40	890.00	1129.50	929.80	68.23	78.52
8C	921.40	974.80	1217.00	1003.80	830.50	989.50	929.80	77.00	93.58
9C	762.30	993.50	1050.20	766.90	1005.50	915.70	929.80	83.24	98.47

Table 4.8(c) Radius of Curvature Results on US 41 based on USF Method @ 45 mph

STATION\RUN	All radius values are in feet							PRECISION(%)	ACCURACY(%)
	1	2	3	4	5	AVERAGE	MANUAL SURVEY		
3C	828.70	1113.30	811.10	960.00	961.90	935.00	929.80	80.92	99.44
4C	820.80	799.20	889.50	746.50	828.40	816.90	929.80	91.11	87.85
7C	1053.60	1155.00	741.60	763.90	1005.90	944.00	929.80	77.64	98.47
8C	774.60	739.90	934.30	816.30	831.10	819.20	929.80	85.95	88.10
9C	1003.00	1124.90	862.80	1053.80	912.50	991.40	929.80	86.53	93.38

Table 4.8(d) Radius of Curvature Results on US 41 based on Compass Method @ 45 mph

	All radius values are in feet								
STATION\RUN	1	2	3	4	5	AVERAGE	MANUAL SURVEY	PRECISION(%)	ACCURACY(%)
3C	817.10	1117.10	816.00	963.10	968.40	936.30	929.80	80.69	99.30
4C	798.50	793.80	878.20	734.70	814.40	803.90	929.80	90.75	86.45
7C	1037.20	1142.90	744.10	767.90	1019.80	942.40	929.80	78.72	98.65
8C	771.80	739.70	939.70	815.20	846.30	822.50	929.80	85.75	88.45
9C	986.60	1123.90	879.80	1076.00	915.80	996.40	929.80	87.20	92.84

Table 4.8(e) Radius of Curvature Results on US 41 based on USF Method @ 55 mph

	All radius values are in feet								
STATION\RUN	1	2	3	4	5	AVERAGE	MANUAL SURVEY	PRECISION(%)	ACCURACY(%)
13C-1	1216.90	1651.60	1411.40	1595.30	1572. 5	1489.50	1306.00	81.69	85.94
13C-2	1231.00	1686.40	1311.10	1680.10	1365.50	1454.80	1306.00	84.09	88.60
13-1C-1	1768.90	2738.60	1816.40	1687.10	2217.30	2045.60	1306.00	66.12	43.36
13-1C-2	1388.10	2871.00	1598.30	1572.90	2534.60	1993.00	1306.00	55.94	47.39
13-2C-1	1424.80	2018.80	1251.20	1280.30	2094.60	1613.90	1306.00	70.21	76.42
13-2C-2	1497.60	1762.90	1155.00	1247.90	1851.90	1503.10	1306.00	76.78	84.91
13-3C-1	1848.30	1848.80	1514.80	1484.20	2224.80	1784.10	1306.00	75.30	63.38
13-3C-2	1255.60	1429.40	1221.50	1280.40	2027.60	1442.90	1306.00	59.47	89.51
13-4C-1	1393.60	1755.60	1221.30	1648.60	1989.00	1601.60	1306.00	75.81	77.36
13-4C-2	1416.30	1369.80	1085.20	1566.50	2005.60	1488.70	1306.00	65.27	86.01

Table 4.8(f) Radius of Curvature Results on US 41 based on Compass Method @ 55 mph

STATION\RUN	All radius values are in feet							PRECISION(%)	ACCURACY(%)
	1	2	3	4	5	AVERAGE	MANUAL SURVEY		
13C-1	800.80	1369.60	823.60	1269.30	1178.70	1088.40	1306.00	73.57	83.33
13C-2	863.00	1297.60	856.50	1259.20	1152.00	1085.70	1306.00	78.89	83.12
13-1C-1	1236.30	1890.70	1047.20	1377.70	1725.90	1455.50	1306.00	70.10	88.55
13-1C-2	991.50	1930.70	895.30	1133.90	1684.70	1327.20	1306.00	54.52	98.37
13-2C-1	910.30	1449.50	730.20	894.90	1574.90	1111.90	1306.00	58.36	85.13
13-2C-2	980.20	1268.40	702.90	913.50	1285.90	1030.20	1306.00	68.22	78.88
13-3C-1	1314.10	1519.30	810.10	1213.30	1580.70	1287.50	1306.00	62.91	98.58
13-3C-2	906.40	1048.20	681.20	913.10	1293.80	968.50	1306.00	66.41	74.15
13-4C-1	975.00	1240.10	720.00	1154.20	1428.00	1103.50	1306.00	65.24	84.49
13-4C-2	996.80	1052.40	699.10	1201.20	1422.90	1074.50	1306.00	65.06	82.27

Based on the above results, the following observations were made:

1. In the case of the relatively aged pavement (SR-26), the precision and accuracy of the radius of curvature values obtained from both methods (modified kinematic or USF and Compass) were unsatisfactory.
2. In the case of the newly laid pavement (US-41), the precision of the radius of curvature values obtained from both methods (modified kinematic and Compass) was satisfactory except at a few locations. However, the accuracy of the radius of curvature values was much more satisfactory since the accuracy computation (Eqn. 4.3) is based only on the average of a number of repetitions and hence the effect of outliers would not be as critical as it is in the case of precision computation. USF and FDOT investigators concluded that the primary reason for the observed inconsistency could be partly attributed to the vehicle wander during any given entire run. Therefore, it was decided to repeat the above experiment under better controlled and guided driving

conditions. Consequently, an enhanced testing program was conducted in January 2006, the results of which are illustrated in Tables 4.8(g) and 4.8(h).

Table 4.8(g) Modified radius of curvature results on SR 41 based on the USF method @45mph

	All radius values are in feet								
STATION\RUN	1	2	3	4	5	AVERAGE	MANUAL SURVEY	PRECISION(%)	ACCURACY(%)
C31-A	926.20	796.30	979.80	949.50	981.80	926.70	1084.00	85.92	85.49
C31-B	897.60	735.30	854.20	820.60	875.00	836.50	1084.00	87.90	77.17
C32-A	995.10	902.90	835.90	882.20	999.60	923.10	1084.00	90.55	85.16
C32-B	839.60	891.30	784.50	919.70	902.50	867.50	1084.00	90.43	80.03
C33-A	766.00	976.50	792.30	805.60	884.40	845.00	1084.00	84.43	77.95
C33-B	759.80	1020.80	737.10	764.50	822.30	820.90	1084.00	75.65	75.73
C34-A	692.00	1007.20	703.30	760.00	784.20	789.30	1084.00	72.40	72.82
C34-B	675.70	1144.50	704.10	809.60	787.80	824.40	1084.00	61.16	76.05

Table 4.8(h) Modified radius of curvature results on SR 41 based on the Compass method @45mph

	All radius values are in feet								
STATION\RUN	1	2	3	4	5	AVERAGE	MANUAL SURVEY	PRECISION(%)	ACCURACY(%)
C31-A	669.90	621.20	888.50	499.30	882.70	712.30	1084.00	70.09	65.71
C31-B	647.30	609.30	779.90	443.00	788.30	653.60	1084.00	67.79	60.29
C32-A	674.50	723.30	721.50	478.90	862.90	692.20	1084.00	69.19	63.86
C32-B	595.70	717.80	741.30	477.60	787.40	664.00	1084.00	71.93	61.25
C33-A	562.00	780.70	731.30	427.30	785.20	657.30	1084.00	65.01	60.64
C33-B	562.20	781.40	656.60	410.40	743.50	630.80	1084.00	65.06	58.19
C34-A	509.10	859.30	608.20	399.40	684.90	612.20	1084.00	59.64	56.47
C34-B	486.70	864.20	645.50	427.30	699.70	624.70	1084.00	61.65	57.63

The results in Tables 4.8(g) and 4.8(h) indicate that driving under better controlled conditions does not improve either the accuracy or the precision of radius of curvature evaluation. Tables 4.7 and 4.8 generally indicate that if at least five repeated trials can be conducted on each curve to be evaluated, using the USF method of evaluation, a reasonable accuracy can be achieved irrespective of the precision. Hence the USF method of evaluation can be recommended for project level evaluation of the radius of curvature of roadways where five repeated trials will not be impractical.

4.9.4 Precision and Accuracy of grade measurements

The precision and accuracy of the vertical grade measurements for US 41 provided by the IMU subsystem are illustrated in Table 4.9. It is seen that the accuracy is entirely unacceptable while even the precision is not satisfactory. The following two reasons can be attributed to this discrepancy:

1. Possible errors in the comparison of the manually surveyed *average grade* between two surveyed locations of the roadway section which are generally 100 feet apart to the *instantaneous grade* at any given station as measured by the IMU.
2. Significant errors caused by the undetected "pitching motion" of the MPSV relative to the roadway. This can be caused by the constant rocking of the MPSV's suspension system about the transverse axis.

In order to address the above concerns, the investigators repeated the grade measurement with the following modifications:

1. Manual grade measurements made at stations spaced at much shorter distance intervals.
2. Mounting a laser sensor on the center of the rear bumper of the MPSV. This new laser coupled with the existing center laser on the front bumper would detect the rocking motion of the MPSV relative to the road.

It must be noted that grade results were not computed for SR 26 (old pavement) without the rear laser since it was seen that the results were unsatisfactory for the new pavement (US 41).

Table 4.9 Vertical grade results for US 41 @ 45 mph (without the rear laser)

STATION\RUN	All grades are percentages							PRECISION(%)	ACCURACY(%)
	1	2	3	4	5	AVERAGE	MANUAL SURVEY		
13C-1	0.08	0.10	0.14	0.09	0.10	0.10	0.03	61.14	Outlier
13C-2	0.12	0.10	0.13	0.10	0.10	0.11	0.09	81.37	83.00
13-1C-1	0.33	0.25	0.23	0.22	0.23	0.25	0.48	68.35	52.74
13-1C-2	0.51	0.42	0.41	0.41	0.41	0.43	0.41	82.81	95.35

In order to address the above concerns, the investigators repeated the grade measurement with the following modifications:

1. Manual grade measurements made at stations spaced at much shorter distance intervals.
2. Mounting a laser sensor on the center of the rear bumper of the MPSV. This new laser coupled with the existing center laser on the front bumper would detect and account for the rocking motion of the MPSV relative to the road.

The results of the renewed experiment are given in Tables 4.10 and 4.11. Comparison of results in Tables 4.9, Tables 4.10(a) and 4.10(b) show that mounting of the rear laser did in fact improve the precision of grades of the new pavement (US 41) considerably, although the test locations are different. Even the results shown in Tables 4.11(a) and 4.11(b) indicate very high precision in the presence of rear bumper laser although a basis for comparison is unavailable in the absence of grades measured on SR 26 without the additional laser. Therefore, one can attribute the lack of precision to the reason (2) stated above. However, the additional laser has not served to improve the accuracy of grades at all. Hence the accuracy issue can be directly attributed to the reason (1) stated above.

Table 4.10(a) Vertical grade results for the graded section on US 41 @ 45 mph (with the rear laser)

	All grades are percentages								
STATION\RUN	1	2	3	4	5	AVERAGE	MANUAL SURVEY	PRECISION(%)	ACCURACY(%)
G2 - G21	0.70	0.76	0.74	0.77	0.77	0.80	0.50	93.59	49.86
G21 - G22	0.69	0.76	0.71	0.74	0.74	0.70	0.50	94.79	50.65
G22 - G23	0.71	0.76	0.70	0.71	0.70	0.70	0.62	93.55	83.94
G23 - G24	0.74	0.77	0.74	0.75	0.74	0.80	0.60	96.92	77.53

Table 4.10(b) Vertical grade results for the curved section on US 41 @ 45 mph (with the rear laser)

	All grades are percentages								
STATION\RUN	1	2	3	4	5	AVERAGE	MANUAL SURVEY	PRECISION(%)	ACCURACY(%)
C31 - C32	1.05	0.96	1.01	1.03	1.02	1.00	1.60	94.94	61.93
C32 - C33	1.06	1.02	1.04	1.09	1.08	1.10	1.70	96.13	62.64
C33 - C34	1.06	1.04	1.03	1.08	1.05	1.10	1.70	97.37	60.68

Table 4.11(a) Vertical grade results for the straight section on SR 26 @ 45 mph (with the rear laser)

	All grades are percentages								
STATION\RUN	1	2	3	4	5	AVERAGE	MANUAL SURVEY	PRECISION(%)	ACCURACY(%)
3S – 3S1	2.55	2.61	2.60	2.58	2.56	2.60	1.40	98.96	13.95
3S1 - 3S2	2.40	2.41	2.40	2.38	2.39	2.40	1.20	99.17	8.56
3S2 - 3S3	2.21	2.19	2.17	2.18	2.20	2.20	1.10	98.99	6.41
3S3 - 3S4	2.13	2.13	2.12	2.11	2.12	2.10	1.00	99.53	11.37

Table 4.11(b) Vertical grade results for the curved section on SR 26 @ 45 mph (with the rear laser)

	All grades are percentages								
STATION\RUN	1	2	3	4	5	AVERAGE	MANUAL SURVEY	PRECISION(%)	ACCURACY(%)
13C - 13C1	0.99	1.00	0.96	1.00	0.98	1.00	0.00	97.47	Outlier
13C1 - 13C2	0.99	0.99	0.96	1.00	0.98	1.00	0.10	97.54	Outlier
13C2 - 13C3	0.84	0.87	0.83	0.87	0.85	0.90	0.50	97.39	Outlier
13C3 - 13C4	0.66	0.67	0.64	0.66	0.63	0.70	0.50	96.70	54.30

Hence the authors conclude that the precision of automatic grade evaluation can be improved by the installation of the rear bumper laser. However, accuracy of automatic grade evaluation cannot be verified unless means are developed for manual evaluating of the *instantaneous grades*.

CHAPTER 5
CONCLUSIONS AND RECOMMENDATIONS

A research investigation was performed to validate two main subsystems of FDOT's multi-functional pavement evaluation vehicle (MPSV); (1) the pavement imaging subsystem and (2) the inertial measurement subsystem.

5.1 The Pavement Imaging Subsystem:

In the first phase of the study the investigators identified various sources of noise that affect the quality of images captured by line-scan cameras in general and pavement distress images of the FDOT MPSV in particular. Furthermore, the signal-to-noise ratio (SNR) was identified as an appropriate indicator of the quality of images. The investigators have shown how SNR can be used as a definitive criterion for the selection of aperture settings and optimum lighting conditions during imaging-based pavement distress evaluations. In addition, several state-of-the-art techniques that show promise in improving the accuracy of crack evaluation based on pavement images were identified. The first phase of the research culminated in the development of a novel and efficient technique for enhancing line-scan images of pavement cracks by using a standard gray-scale target.

Next, an experimental investigation was conducted to study the effect of vehicle speed, pavement type, and different lighting conditions on the quality and precision of digital line-scan pavement images. The quality of images was assessed objectively using the signal-to-noise ratio (SNR). In addition, the effect of geometrical distortion on the crack evaluation, and blurring of images due to vehicular vibration was quantified in terms of the instantaneous displacement of image features. The results of this investigation showed that the vehicle operating speed does not significantly affect the quality of images or the ability of accurate recognition of cracks in a pavement. It was also seen that the artificial lighting system itself introduces a significant level of noise in the images in

both asphalt and concrete pavements, especially under adequate ambient lighting. The research findings also indicate that conditions which produce relatively higher SNR have a tendency to improve the accuracy of crack evaluation. Hence, prior assessment of SNR using standard grayscale targets can be used as an approximate but reliable indicator of the expected accuracy of crack evaluation.

Although the test results generally indicate satisfactory repeatability of the imaging subsystem with respect to the quality of images and details of their content, crack measurements are seen to have a relatively higher variability in surveys without the pavement lighting system due to the higher uncertainty in crack recognition. Hence it was seen that, under poor ambient lighting conditions, a user will gain an overall benefit from an artificial lighting system. On the other hand, during adequate ambient lighting, use of artificial light introduces excessive noise with little improvement in the crack measurement accuracy. Based on the research findings it can be also concluded that, for hairline cracks less than 3 mm wide, the error in recognition ability is relatively high, sometimes exceeding100%. In contrast, for features larger than 10 mm in width, the maximum error rarely exceeds 9.5%. Moreover, the incorporation of corrections for geometrical distortion caused by optical distortion and Distance Measurement Instrument (DMI) error were found to improve the accuracy of crack evaluation significantly.

5.2 Inertial Measurement Subsystem:

The quality of roadway cross-slope, grade and curvature data provided by the IMU subsystem of the FDOT MPSV was the target of the third and final phases of the study reported here. The precision and accuracy of cross-slope and super-elevation data were seen to be acceptable for FDOT evaluation needs, both on newly laid and relatively aged pavements. As for the radius of curvature computation, a number of analytical techniques were used to overcome the undulations and uncertainties involved in the recording of curvature data from the IMU subsystem. The use of moving averages and statistical

filtering were seen to be particularly effective in stabilizing the curvature plots. Based on the comparison with radii values computed from manual surveys, the modified kinematic method and the Compass method were shown to be equally capable of predicting accurate radii of curvature for circular as well as non-circular curves.

During the fourth and the final phase of the study, a comprehensive experimental program was developed for the validation of roadway geometrical data produced by the IMU subsystem of the MPSV, by comparing them with corresponding data obtained from manual surveys. It was seen that the cross-slope and super-elevation data were generally repeatable and accurate based on ASTM specifications on both newly laid and relatively aged asphalt pavements. The precision and accuracy results of the preliminary testing program on SR 222 in Gainesville, FL, presented in Chapter 3 and those of the detailed testing program on two pavement facilities at different stages of their life cycle, newly laid US-41 and relatively aged SR-26, presented in Chapter 4 were satisfactory. The above findings indicate that the FDOT MPSV can be used to evaluate the roadway cross-slopes and super-elevations to minimum accuracies of 86% and 88% on newly laid and relatively aged pavements respectively at 95% confidence. Hence the investigators conclude that the FDOT MPSV is well-equipped for statewide implementation of automated cross-slope and super-elevation measurements.

However, the initial precision and accuracy estimates of radii of curvature data were significantly lower than those of the cross-slope measurements, on both new and old pavements. Once the possible causes of such inaccuracies were identified, the relevant experiments were modified to overcome the limitations of the initial experimentation. With respect to the improvement of radii of curvature measuring techniques, more controlled, better guided and smoother vehicle maneuvering on curves in particular yielded more precise curvature data. However, the accuracy of the MPSV radius of curvature data as compared to manual measurements was acceptable only when five

repeated measurements were averaged. Therefore, the investigators conclude that MPSV is an excellent tool for accurately evaluating the curvature at the project level where making at least five repeated runs would be feasible.

With respect to localized grade data, the newly installed rear bumper laser yielded very high precision. However, a similar level of accuracy could not be achieved with respect to manual grade measurements. The primary reason for the discrepancy between MPSV grade measurements and the manual measurements was that the latter information is not usually obtained on a localized basis to be comparable with the localized grade data produced by the MPSV.

The results of the experimental validation of the imaging and inertial systems of the MPSV will benefit the research efforts towards automated distress evaluation, rapid evaluation of roadway geometry as well as improved geometric design of roadways.

5.3 Recommendations

The frontier of imaging technology lies in the development of software that can be used to accurately classify and quantify pavement distress on real-time basis. In this regard, FDOT would be able perform automated or interactive crack evaluation using the MPSV, when appropriate automated or interactive evaluation systems which can function in conjunction with the MPSV's imaging and inertial sub-systems are identified. Such automation efforts would be boosted by the precision and accuracy limitations of crack evaluation found from this research and the adoption of the developed image enhancing techniques.

In addition, the envisioned automated crack evaluation system can be calibrated to detect excessive distress levels that do not conform to the age of pavements or the cumulative traffic imposed on them. This effort will enable the MPSV to be used effectively in

setting up definitive pavement construction job acceptance standards with respect to cracking. Therefore, the MPSV would be an invaluable tool in the formulation of pavement crack thresholds and acceptance standards with respect to the pavement age and in the speedy verification of the above standards in new construction projects.

Based on research findings, the investigators also recommend the following upgrades to the MPSV that would enhance the reliability and accuracy of crack evaluation:

1. Replace the existing linescan camera and the pavement lighting system with two identical linescan camera systems each equipped with a laser-based pavement illuminator. The benefits of the upgraded system would be the increased resolution (from 2048 pixels per line to 4096 pixels per line), and the potential for eliminating shadows that would reduce the brightness of the pavement images.

2. Replace the current DOS-based imaging controller in the Mobile Data Recorder (MDR) with the windows-based controller, *WINPRO*. The primary motivation behind the investigators' recommendation is that the latter control system has the potential for resolving the issue of intermittent imaging data overflow causing the imaging system to shut-down during surveys.

REFERENCES

Askey, P.: "JPEG,"http://www.dpreview.com/learn/?/Glossary/Digital_Imaging/JPEG_01.htm, Digital Photography Review TM, 1998-2001

American Association of State Highway and Transportation Officials, "Standard Practice for Quantifying Cracks in Asphalt Pavement Surface" (No. PP 44-01), AASHTO, April 2001, Publication No. HM-20-COM

ASTM Standard E 177 90a, "Standard practice for use of the terms Precision and Bias in ASTM test methods", 1990.

ASTM Standard E 950, "Standard test method for measuring the longitudinal profile of traveled surfaces with as accelerometer established inertial profiling reference".

ASTM Standard E 1082 90, "Standard test method for measurement of vehicular response to traveled surface roughness", 1990.

ASTM Standard E 1489 96, "Standard practice for computing ride number of roads from longitudinal profile measurements made by an inertial profile measuring device", 1996.

ASTM Standard E 1364-95, "Standard test method for measuring road roughness by static level method", 1995.

Beer F.P., Johnston E.R. Jr, *Vector Mechanics for Engineers-dynamics*, Mc Graw-Hill, New York, 1977.

Deiries, S.: "How CCD Quantum Efficiency is Computed," http://www.eso.org/projects/odt/CCDtestbench/QEcalc.pdf, European Southern Observatory 2004

Efford, N.: "Digital Image processing – A Practical Introduction Using Java," Pearson Education Limited, 2000

FDOT *Greenbook*, "Manual for Uniform Minimum Standards for Design, Construction and Maintenance for Streets and Highways", FDOT, May 2002.

Fisher, R., Perkins, S., Walker, A., and Wolfart, E.:" Image Synthesis – Noise Generation," http://www.dai.ed.ac.uk/HIPR2/noise.htm, R. Fisher, S. Perkins, A. Walker and E. Wolfart 2000

Ganguly A., Class notes, CEE 6933, Time Series and Spatial Statistic,, Dept. of Civil and Environmental Engineering, University of South Florida, Summer 2004.

Glenon J.C., Loumiet J.R., "Measuring Roadway Curve Radius Using the Compass Method", January 2003.

Gunaratne, M. Mraz, A. and Sokolic, I. "Study of the feasibility of video logging with pavement condition evaluation", Report submitted to FDOT", Report number BC-965, August 2003.
Jasc Software Paint Shop Pro 8. < http://www.jasc.com/products/paintshoppro/>, 2004

Lee, J-S.: "Refined Filtering of Image Noise Using Local Statistics," Computer Graphics and Image Processing 15, pp. 380-389, 1981

Licha, T.: "Math & Myth – Signal To Noise Ratio and Image Combining," http://www.licha.de/AstroWeb/articles_fullsize.php3?iHowTo=14, The Astroscopic Lab 2002

Miller, J., and Bellinger, W. *Distress Identification Manual for Long-Term Performance Program.* U. S. Department of Transportation, Federal Highway Administration, 2003.

Mraz, A. *Evaluation of Digital Imaging Systems Used in Highway Applications*, Doctoral Dissertation, University of South Florida, Tampa, FL, July 2004.

Mraz, A., Gunaratne, M., and Nazef, A.,"Guidelines for Evaluation of Digital Imaging Systems Used in Highway Applications," ASCE Journal of Transportation Engineering, June 2005, Vol. 131, No. 6.

Norton, P.: "How Does the Peltier Cooler Works," http://www.techtv.com/screensavers/print/0,23102,1298,00.html, TechTV, 2004

Owens, R.: "Image Enhancement – Spatial domain methods," http://homepages.inf.ed.ac.uk/rbf/CVonline/LOCAL_COPIES/OWENS/LECT5/node3.html#SECTION00033100000000000000, School of Computer Science and Software Engineering M002, The University of Western Australia, 1997

POS/LV V3 Installation and Operation Guide, Applanix Corporation, Ontario, Canada, 2000.

POSPac User Manual, Applanix Corporation, Ontario, Canada, 2002.

Rasband, W. *ImageJ – Documentation*. National Institute of Mental Health, Research Service Branch, Maryland. http://rsb.info.nih.gov/ij/docs/index.html. Accessed July 1, 2005.

Roper Scientific: "Signal-to-Noise Ratio," http://www.roperscientific.com/library_enc_signal.shtml, Roper Scientific 2004.

Scherzinger B.M., "Precise robust positioning with inertial/GPS RTK", Proceedings of ION-GPS 2000, Salt lake city, Utah, September, 2000.

Schowengerdt, R..: "Image Noise," http://www.ece.arizona.edu/~dial/ece533/notes12.pdf, The Digital Image Analysis Laboratory, Department of Electrical and Computer Engineering, University of Arizona, 2003

Smith, R., Freeman, T., Pendleton, O. Evaluation of Automated Pavement Distress Data Collection Procedures for Local Agency Pavement Management. Prepared for Washington State Department of Transportation, Texas Transportation Institute, Texas A&M University, College Station, TX, 1996.

Sonka, M., Hlavac, V., Boyle, R.: "Image Processing, Analysis, and Machine Vision," PWS Publishing, 1999.

Stein, J. (2004) *CCD Paramenter*. <http://home.arcor.de/j_stein/tips3_e.html>.

Van Dine C.P., Overturf J., "Route mapping and linear referencing with photolog geometric data", Proceedings GEOTEC event, Vancouver, BC, March 2003.
Minnesota DOT, *Roadway Design Manual (Metric)*,

Wang, K.C.P., "Design and Implementations of Automated Systems for Pavement Surface Distress Survey", Journal of Infrastructure Systems, ASCE, Vol. 6, No.1, March 2000**.**

Wang, K.C.P., "Data Analysis of a Real-Time System for Automated Distress Survey", Proceedings of the Transportation Research Board meeting, January 2002.

Yair, W.:" Statistical Signal Processing – Note on the proper definition of white-noise processes," http://www.cs.huji.ac.il/course/2003/ssp/white_noise_def.ps, The Hebrew University of Jerusalem, The Selim and Rachel Benin School of Computer Science and Engineering, 2004

Young, I. T., Gerbrands, J. J., van Vliet, L. J.: "Image Processing Fundamentals," http://www.ph.tn.tudelft.nl/Courses/FIP/frames/fip.html, Pattern Recognition Group, Department of Applied Physics, Faculty of Applied Sciences, Deft University of Technology, The Netherlands.

http://www.dot.state.mn.us/tecsup/rdm/metric/3m.pdf , October 1999, accessed on 07/13/2004.

APPENDIX A
Procedure for *Applanix* POS LV System Calibration and Verification

A.1 Required Equipment:

1. Laser calibration bar
2. Electronic level
3. DMI simulator
4. Two identical ramps
5. Measuring tape with a precision of 1 mm.

A.2 Calibration Procedure

Step 1

(a) Station the survey vehicle on a reasonably flat ground surface

(b) set the calibration bar (that encompasses all the lasers) under the lasers (Fig. A.1)

(c) level the calibration bar using appropriate adjustment plates and an electronic level.

Note: Selection of a flat ground surface merely facilitates leveling of the calibration bar in a stable manner. Even after perfect leveling is achieved, it could be noticed from the MDR computer that the laser readings may not be generally identical. This indicates the need for laser correction (Step 2(c)) as well as calibration of the integrated POS-LV - laser system (Step 2(a)-(c)). *Therefore, the laser correction factors (CF) must not be set during this step.*

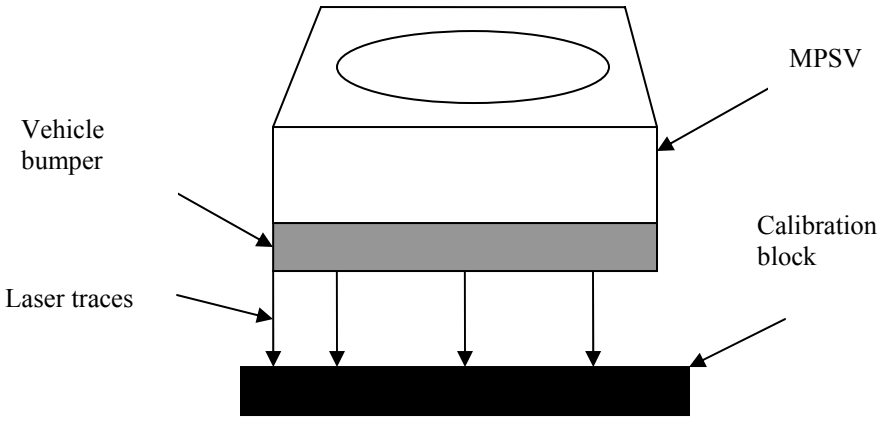

Fig. A1. Laser calibration

Step 2

(a) Attach the DMI simulator onto the MDR to simulate vehicle movement. This operation will activate the POS-LV system to display the heading, tilt and grade readings.

Note: *It is assumed that a zero tilt reading indicates perfect horizontal positioning of POS-LV as presumably verified by its manufacturer*.

(b) If the tilt reading is not zero, the vehicle floor-board must be manually tilted (preferably at the middle of the vehicle) with respect to the ground to achieve a zero tilt reading.

Note: On completion of Steps 1 and 2(a) and 2(b), it is assured that both the calibration bar and the POS-LV system are perfectly horizontal. Then, if the lasers are installed at the same vertical position (height) of the vehicle bumper, the laser sensors must produce identical readings. However, due to unavoidable minor differences in the mounting of laser sensors on the vehicle bumper, these sensor readings will rarely be identical after Steps 1 and 2(a) and 2(b). Therefore, at this stage the laser correction factors (CF) can be applied.

(c) Apply laser corrections in the laser calibration mode of the MDR.

Note: the CF factors are computed based on the assumption that the laser sensor at the least height from the calibration bar is at the "standard" vertical height and hence provides the accurate distance to the calibration bar. Once the corrections are made and the MDR is taken out of the laser calibration mode, all the laser sensors would indicate identical readings (equal to the original reading of the laser sensor at the least height from the calibration block). Care must be exerted not to change the laser calibration in any subsequent operation or evaluation.
This completes the calibration process of the laser and the POS-LV system.

A.3 Determination of the POS-LV bias and Verification of the POS-LV Calibration.

Step 1

(a) Drive the front and the rear wheels of the right side of the vehicle onto the two identical ramps (Fig. A.2)

(b) Station the vehicle so that the laser spots are still visible on the leveled calibration bar used in Step 1.

(c) Compute the angle of tilt as

$$\phi = \sin^{-1}(h/L) \tag{A.1}$$

where h = height of the ramp and L = distance between the innermost points on the two wheels

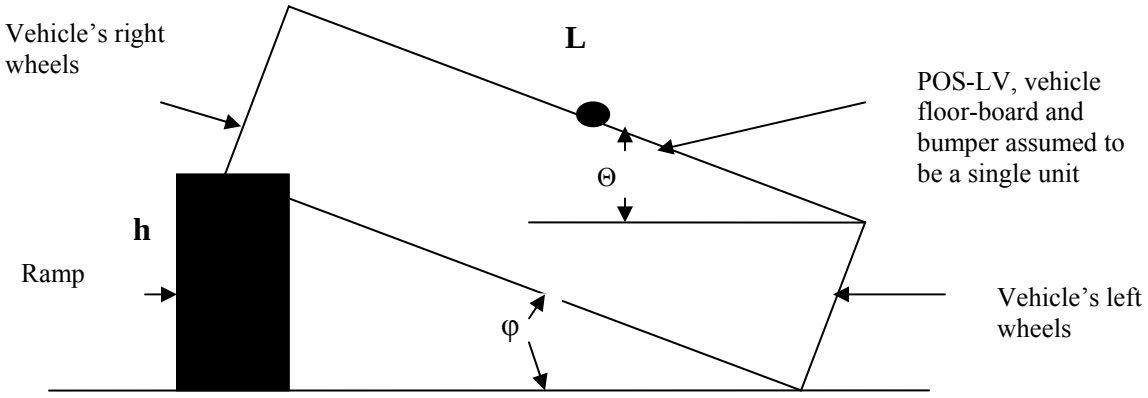

Fig. A.2 Calibration mode on clockwise rotation

Step 2

(a) Observe the laser sensor readings (d_i) on the MDR computer

(b) Compute the vehicle tilt based on the differences in sensor readings and the sensor positions.

(c) Compute the laser slope as (Fig. A3)

$$\alpha = \tan^{-1}[(d_2 - d_1)/L_2] = \tan^{-1}[(d_3 - d_1)/L_3] = \tan^{-1}[(d_4 - d_1)/L_4] \tag{A.2}$$

where L_2, L_3 and L_4 are the distances of the sensors 2,3 and 4 from sensor 1.

(d) Verify that $\phi = \alpha$

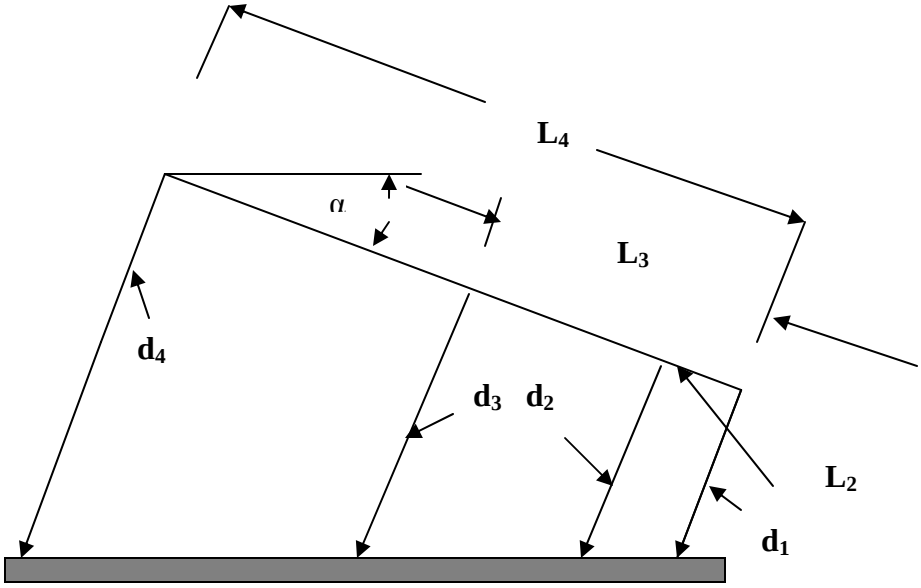

Fig. A.3 Configuration of laser measurements

Step 3

(a) Observe the tilt reading of the POS-LV (*-2*)

Note: the "-" sign indicates counter-clockwise rotation.

If $\phi = \theta$ calibration is verified for counter-clockwise rotation.

If $\phi \neq \theta$, then three sources of error are possible,

Error 1. The POS-LV system is deviated from the vehicle floor-board and bumper plane (Fig. A.2)

Error 2. A zero tilt reading does not imply perfect horizontal positioning of POS-LV (Step 2)

Error 3. Malfunctioning of the POS-LV system

(*Note that errors 1 and 2 are systematic errors*)

(b) Express the error β as follows:

$$\phi = \theta + \beta \qquad \text{(A.3)}$$

Step 4

(a) Drive the vehicle's front and rear wheels of the left side of the vehicle onto the same two identical ramps (Fig. A.4)

(b) Station the vehicle so that the laser patches are still observed on the leveled calibration block used in Step 1 of Section A.2.

(c) Compute the angle of tilt and the new laser slope as

$$\phi' = \alpha' = \tan^{-1}[(d_1 - d_2)/L_2] = \tan^{-1}[(d_1 - d_3)/L_3] = \tan^{-1}[(d_1 - d_4)/L_4] \quad \text{(A.4)}$$

(d) Repeat step 3 (Section A.3) to verify that $\phi' = \theta'$, where θ' is the new POS-LV reading measured in a clockwise sense. This completes the verification of calibration.

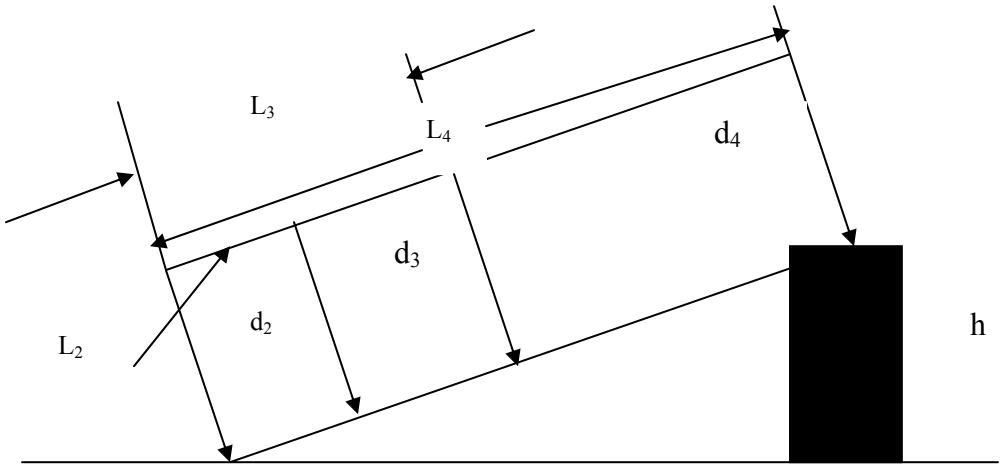

Fig. A.4 Calibration mode on counter-clockwise rotation

If $\phi' \neq \theta'$, express the new error $*$ as follows:

$$\phi' = \theta' - \delta \quad \text{(A.5)}$$

A.4 Visualization of POS-LV Errors

The errors expressed in Eqns. (A.3) and (A.5) (∃ and ∗ respectively) can be illustrated in Figs. A.5(a) and A.5(b) respectively. If they are due to the first two sources of errors identified in Step 3 of Section A.3, it can be visualized from Fig. A.5(a) and A.5(b) that ∃ = ∗.

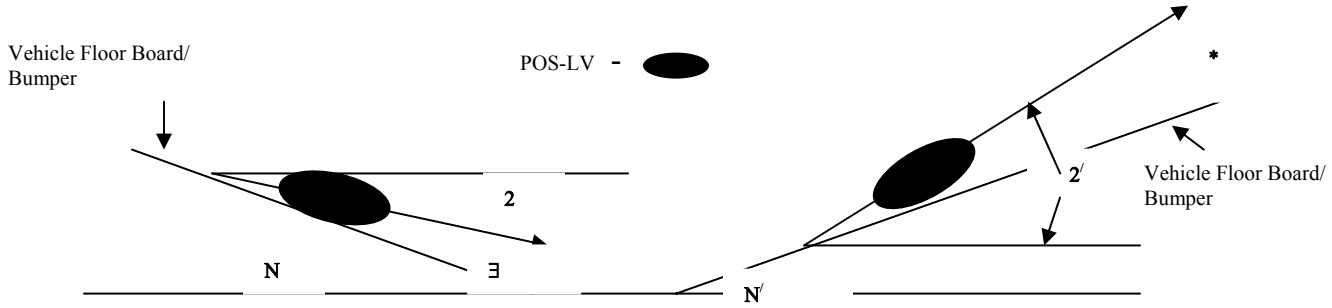

(a) (b)

Figure A5 Configuration of errors

Conclusion: If ∃ and ∗ (from. Eqns. (A.3) and (A.5)) are found to be equal in magnitude then we can estimate the systematic error due to the sources of error 1 and 2. Otherwise we conclude that the POS-LV system must be malfunctioning.

APPENDIX B
Procedure for Distance Measuring Instrument (DMI) and Camera Systems Calibration

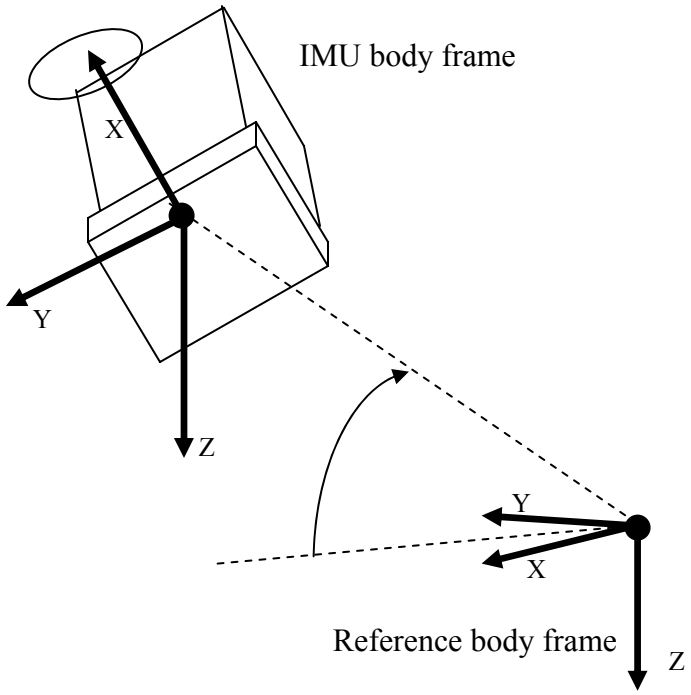

Figure B1: IMU with respect to Reference Frame Mounting Angles

B.1 DMI Scale Factor Calculation

The DMI measures wheel rotation by generating a fixed number of pulses per wheel rotation. POS LV converts wheel rotation into distance traveled by multiplying the DMI pulse count by a scale factor that converts pulses to metres. The following formula is used to compute the DMI scale factor s:

$s = \frac{n}{d\pi}$, where n is the number of DMI pulses per revolution, and d is the instrumented wheel diameter in meters

Note: The number of DMI pulses per revolution is typically stamped on the DMI nameplate.

- DMI generates 1024 pulses per revolution

- $s = \frac{1024}{d\pi} = \frac{1024}{0.5 \times 3.14} = 652$ pulses/m

The DMI direction sense is programmed by setting the sign on the DMI Scale Factor. If the DMI is mounted on the driver's left side, a positive DMI Scale Factor is used. Conversely, if the DMI is mounted on the driver's right side, a negative DMI Scale Factor is used.

B.2 GPS Antenna Separation

GPS antenna separation (between two antennas) is the distance between the phase centers of the two GPS antennas used by POS LV. This distance is used by the GPS Azimuth Measurement Subsystem (GAMS) for heading aiding.

Measure the length of the straight line joining the two GPS antenna phase centers; measurement is critical to within five millimeters.

B.3 DOWNWARD LINE SCAN CAMERA FOCUS AND CALIBRATION STATIONARY TEST

1. Connect 5khz signal oscillator to 7w2 connector input located in the rear of the downward video imaging system.

2. Turn on ups power and light system.

3. Turn on downward imaging system computer.

4. Select **CTRL ALT DEL**.

5. Enter password **ICC**

6. Select **ICCLINESCAN** icon on desk top. Close and reopen.

7. Click on the save images box. Image should appear on the monitor.

8. Place a 25 line focus graph paper on the ground in the center of where the line-scan width. Check on monitor for image of the graph. Continue to move paper until all 25 lines appear. If focus is off adjust focus directly at the camera lens. After adjusting focus, use silicon to secure the position of the lens.

9. After best focus is obtained place a 7 line test graph at each edge of the line scan. look at the image on the monitor. using the horizontal scroll check both edges for graphs, making sure all 7 lines on each end are in the image. This will assure full image of scan is being seen.

10. Using a chalk line, mark a line through the center of all the black lines of the graphs. This will show the line in which the camera is scanning.

11. Take a Lux light meter and lay it down flat on chalk line and measure the light reading on the chalk line.

12. Adjust the spot lights mounted in the rear of vehicle to get a consistent light reading across the chalk line. 50000 to 70000 lux is desired.

B.4 DVC 1310 FOCUSING AND EXPOSURE SETTING PROCEDURE

Focusing the DVC1310 cameras is done manually. The focal point can be adjusted to the customer's preference. For initial focus and exposure settings, the customer should go into the c-view for windows program, and follow the white balance procedure. (see Mississippi imaging van procedure, forward system set up).

Once the program is running and images are continuously being grabbed, the operator can manually turn the focus on the lens of the camera, and view the picture on the monitor screen. Turn until the best focused picture is seen. if the lens is fully turned to infinity, and additional focusing is needed, loosen the lens lock down nut located on the front face of the camera. Use the included camera wrench to perform this task. Screw in the lens until the image seen on the monitor screen is in focus. Retighten the lens lock down nut with the camera wrench to secure the lens.

The *fstop* controls the exposure of the image and can be manually adjusted by turning it on the lens. The *fstop* is factory set to wide open on the downward lens, and set to an f/4 on the forward and sign lenses. When the *fstop* is turned to a larger number, the exposure is decreased, allowing less light in the lens, which causes a darker picture. When the f/stop is turned to a lower number, the exposure increases allowing more light into the lens, causing a brighter picture.